

Fundamental study aiming for sustainable urban environment from viewpoints of wind engineering and comparative sociology

佐藤, 幹

<https://doi.org/10.15017/1807092>

出版情報：九州大学, 2016, 博士（工学）, 課程博士
バージョン：
権利関係：全文ファイル公表済

**Fundamental study aiming for sustainable urban environment from
viewpoints of wind engineering and comparative sociology**

Tsuyoshi Sato

A thesis submitted for the degree of Doctor of Engineering

March 2017

ABSTRACT

Urban environmental problems such as heat island phenomenon and air pollution have attracted social attentions reflecting the increase of the importance of cities due to the concentration of political-economic functions and continuous increase of population, and the realization of pleasant environment in urban areas has been desired in recent years. However, it is extremely difficult even with the latest scientific knowledge. One of the most critical reasons is that urban-type environmental problems are caused in consequence of a complicated interaction of physical and nonphysical phenomena with different temporal-spatial scales. For example, one of the major reasons of air pollution in urban areas is a decrease of air ventilation because of a dense arrangement of buildings, and this is considered to be a problem of wind engineering or urban atmospheric boundary layer science with a time scale of 10^3 - 10^4 s and spatial scale of 10^1 - 10^2 m. Another major cause is the increase of pollutant emissions from vehicles, residential housings, and factories. It is thought that this problem should be solved by environmental policies, which is formulated through a few tens of years of discussion among stakeholders and applied for entire of the urban area (e.g. park and ride system in European countries and antipollution ordinances in Japan in the middle of the 20th century).

For this complicated nature of urban type environmental problems, it is considered that the comprehensive view underpinned by knowledge from both physical and nonphysical scientific research is required to accomplish pleasant urban environment. Therefore, this thesis conducted a series of fundamental studies from the viewpoints of wind engineering and comparative sociology as a starting point to realize sustainable urban environment.

Chapter I demonstrates the background and purpose of this study. The significance of the approaching from comparative sociology and wind engineering is demonstrated with a comprehensive reviews of past studies in each study field.

Chapter II is the Study on the formulation process of sustainable society by comparative sociology. Kitakyushu city in Japan and Emscher area in Germany are employed as pioneering models of environmentally friendly societies, and their regional histories over past 100 years are compared mainly focusing on the economic and environmental situations. The intercomparison of regional histories disclosed that the social movements for improving environment started in the late of the 20th century, and it was accelerated from the end of the 20th century to the present days. Subsequently, it is demonstrated that the three factors: 1) symbols of an environmentally friendly society, 2) managing organizations with a comprehensive view, 3) use of regional legacies played a significant role for realizing sustainable societies in the two regions.

Chapter III systematically investigates the measurement accuracy of particle image velocimetry (PIV) experiment on unsteady turbulent flow fields around scaled urban building models in a large size wind tunnel. At first, the past PIV experiments in wind engineering and urban atmospheric boundary layer science are overviewed in order to determine the typical experimental setting of PIV in a large-size wind tunnel, and discuss whether the typical experimental condition has any problem or not in the light of the theory of PIV. Through the discussion, it is proved that peak locking problem is generally unavoidable under the typical experimental condition, degrading the measurement accuracy. Thus, a countermeasure for peak locking problem using mask correlation method (MCM) was proposed, and the effectiveness of the countermeasure is tested using experimental data obtained by the authors. The test results indicate image quality

including particle size on images, image contrast, and signal noise ratio are improved, and peak locking is drastically mitigated if the countermeasure was applied.

Chapter IV presents the results of a PIV experiment on the turbulent flow fields around high rise building models which imitates downtown areas. The spatial distributions of turbulent statistics in UCL and RSL are investigated, and the similarity with turbulent flow fields around cubic and vegetation canopies are demonstrated, such as two inflection points of temporally averaged streamwise velocity profile, rapid decreasing of Reynolds stress within a canyon. Subsequently, the characteristic instantaneous flow motions are examined and the following three results are obtained: 1) low-speed up flow (ejection) and high-speed downward flow (sweep) occur intermittently around the roughness models, and their features including frequency and duration time are similar to the ejection and sweep events around low-rise building models, 2) hairpin packet structures consisting of a series of hairpin vortexes which line the streamwise direction occurs above the roughness models, 3) hairpin packet structures might be related to the occurrence of ejection and sweep events around the roughness models.

Chapter V presents the results of PIV experiments on turbulent flow fields around 2D street canyons with and without flat eaves in order to investigate how the complexness of roughness geometry affects the turbulent flow fields. The temporally averaged flow field structures are drastically changed by the effect of eaves, and they are not classified in fundamental flow regimes presented in the past studies. In addition, turbulent coherent structure are investigated by the spatial distributions of two point correlation coefficients of streamwise and vertical velocity components. The penetration of turbulent coherent structures into a canyon is prevented by eaves under the condition that the distance between buildings is small, and the interaction of the turbulent flow between the region

inside and above a canyon becomes extremely poor. Furthermore, the canyon ventilation rate is largely reduced by the effect of eaves in a dense canyon, while the influence of eaves on canyons ventilation is small in a sparse canyon. Finally, the increase and decrease trend of bulk drag force is discussed associated with the transition of temporally averaged flow field structures in street canyons.

Chapter VI summarizes the main contribution of previous four chapters.

Contents

CHAPTER I

Introduction

1.1 Background and motivation.....	1
1.2 Approach and objective.....	3
1.2.1 <i>Social consensus for the construction of an environmentally friendly society</i>	4
1.2.2 <i>Turbulent flow fields around scaled models of urban buildings</i>	5
1.3 Structure of thesis	16
References.....	19

CHAPTER II

Study on the formulation process of sustainable society by comparative analysis on pioneering regions in Japan and Germany

2.1 Introduction	25
2.2 Historical backgrounds of the two regions.....	27
2.2.1 <i>Period 1: Dawn of heavy industry</i>	28
2.2.2 <i>Period 2: Golden age and environmental problems</i>	30
2.2.3 <i>Period 3: Decline of heavy industry and economic recession</i>	33
2.2.4 <i>Period 4: Area revitalization</i>	35
2.3 Three success factors for the achievement of an environmentally friendly society	39
2.3.1 <i>Management organization</i>	39

2.3.2 <i>Symbol of revitalization</i>	41
2.3.3 <i>Legacy of heavy industry</i>	44
2.4 Application to developing countries	47
2.5 Conclusion	50
Reference	52

CHAPTER III

Study on measurement accuracy of PIV in a large size wind tunnel

3.1 Introduction	58
3.2 Experimental procedure and typical experimental condition	64
3.3 Peak locking problem	72
3.4 Countermeasure for peak locking problem	75
3.5 Performance test of MCM	77
3.5.1 <i>Quality of the sample images</i>	77
3.5.2 <i>Test Results</i>	80
3.6 Conclusion	86
Reference	88

CHAPTER IV

Study of coherent structure around high rise buildings

4.1 Introduction	95
4.2 Experimental set up	98
4.2.1 <i>Wind tunnel and configuration of the array</i>	98
4.2.2 <i>Particle image velocimetry</i>	99

4.3 Experimental results	101
4.3.1 Streamwise velocity	101
4.3.2 Turbulent statistics.....	104
4.3.3 Typical instantaneous upward flow fields.....	107
4.3.4 Typical instantaneous downward flow fields.....	112
4.4 Conclusion.....	115
Reference.....	117

CHAPTER V

Research on the effect of ancillary structures on turbulent flow fields

5.1 Introduction	121
5.2 Experimental setting	126
5.2.1 Wind tunnel and roughness configuration.....	126
5.2.2 PIV setting	129
5.2.3 Drag measurement.....	131
5.3 Temporally averaged flow field structure	132
5.4 Spatial distribution of turbulent statistics	137
5.4.1 Standard deviation.....	130
5.4.2 Reynolds stress.....	142
5.5 Turbulent coherent structure	144
5.6 Canyon ventilation rate	153
5.7 Drag coefficient.....	155
5.8 Conclusion.....	157
References	159

CHAPTER VI

Conclusion

6.1 Conclusive summary.....	163
Reference.....	167

List of figures

Figure1-1: Schematic of climatic scales and vertical layers found in urban area. PBL(planetary boundary layer), UBL(urban boundary layer), UCL (urban canopy layer) and related studies in each scales. Representative studies in urban climatology and their targets are also presented (quoted from Oke 2006, and modified by author)	7
Figure 1-2 Schematic of time and spatial scales of target flow fields of past research in urban climatology	9
Figure1-3: Conceptual diagram of turbulent organized structure (hairpin packets structure) growing up from the wall (quoted from Adrian et al. 2000).....	12
Figure1-4: Conceptual diagram of flow fields around different shapes roughness models	14
Figure1-5: Structure of thesis	18
Figure2-1: Locations of (a) Kitakyushu and (b) Emscher (red marks)	27
Figure2-2: Landscape of Yahata region in the early of the 20th century (quoted from http://meijimeisho.at.webry.info/201305/article_3.html)	29
Figure2-3: Transition of Emscher River from 1899 to 2007 (quoted from http://www.eglv.de/emschergenossenschaft/emscher-umbau/emscher/zeitreise/)	32
Figure2-4: Smoke emission from factories in Kitakyushu in the 1960s (quoted from http://www.city.kitakyushu.lg.jp/kankyoku/file_0269.html)	34
Figure2-5: Landscape of the Emscher area in the industrial period (quoted from http://www.art-society.com/report)	34

Figure2-6: Water pollution in Doukaiwan Bay (a)in 1960 (b)in 1980 (quoted from http://www.city.kitakyushu.lg.jp/kankyoku/file_0269.html)	34
Figure2-7: Research of public disruptions by women’s association (quoted from http://www.city.kitakyushu.lg.jp/kankyoku/file_0269.html)	42
Figure2-8: (a)Heritage of the Zollverein Coal Mine Industrial Complex (b)Coal factory in Dortmund (quoted from Motooka and Tanaka, 2006)	46
Figure3-1: Typical experimental setting of PIV in a large size wind tunnel. Parameters are estimated from the past experiments listed in table 3-2.....	65
Figure3-2: General experimental procedure of PIV.....	65
Figure3-3: Spatial distribution of temporally averaged streamwise velocity around a 2D street canyon converted in pixel unit	70
Figure3-4: Relation between particle size and measurement error (quoted from the text book published from the visualization society of Japan (2012) and modified by author).....	70
Figure3-5: Analysis procedure of particle size on image.....	74
Figure3-6: Particle image data with different focus conditions	74
Figure3-7: Procedure of Mask correlation method (MCM).....	76
Figure3-8: Roughness arrangement of the TR-PIV experiment (Sato et al. (2016)). Black dashed line: center line of the canyon, black plots: positions of sample data used in section 3.5.2.....	78
Figure3-9: Results of preprocessing by MCM. (a) and (b): raw and modified image. (c), (d), (e) and (f): enlarged views at the red and yellow squares. Blue dashed lines: squares of 30×30pixel. The red circles indicate same particles.....	79
Figure3-10: Histograms of the instantaneous displacement in pixel units, dashed line:	

without MCM, solid line: with MCM, (left): horizontal displacement, (right): vertical displacement, (a),(d): $(x/H, z/H)=(1.5, 1.5)$, (b),(e): $(x/H, z/H)=(1.5, 1.0)$, (c),(f): $(x/H, z/H)=(1.5, 0.5)$ 81

Figure3-11: Histograms of the sub pixel part of instantaneous displacement, white bar: without MCM, gray bar: with MCM, (left): horizontal displacement, (right): vertical displacement, (a),(d): $(x/H, z/H)=(1.5, 1.5)$, (b),(e): $(x/H, z/H)=(1.5, 1.0)$, (c),(f): $(x/H, z/H)=(1.5, 0.5)$ 82

Figure 3-12: Vertical profiles of streamwise wind velocity and turbulent statistics measured at the three lines in figure 3-8. Blue plots: without MCM, red plot: with MCM. (a) U/U_{20H} , (b) σ_u/U_{20H} , (c) σ_w/U_{20H} , (d) $-\overline{u'w'}/u_*^2$, (e) Sk_u , (f) Sk_w 84

Figure3-13: Vertical profiles of correlation coefficients on the center line of canyon ($x/H=1.5$), white plots: without MCM, black plot: with MCM..... 86

Figure4-1: Side view of experimental set up..... 98

Figure4-2: Schematic plan view of block array and the position of laser seat 99

Figure4-3: Size and position definition of integration area 99

Figure4-4: Dotted square: experimental data has high accuracy, solid line: center of measurement area.....102

Figure4-5: Comparison of vertical profiles of streamwise wind velocity and turbulent statistics in various types of vegetation canopies and present study. All profiles of present experiment are measured at the center of the measurement area (figure4-4). U_H is time averaged streamwise velocity measured at canopy roof height and u_* is friction velocity. (a) U/U_H , (b) σ_u/u_* , (c) σ_w/u_* , (d) Sk_u , (e) Sk_w , (f) $-\overline{u'w'}/u_*^2$, (g) $-\overline{u'w'}/\sigma_u\sigma_w$ 103

Figure4-6: Special averaged profile of contribution for the momentum transfer by four quadrants. Square, triangle, diamond and circle plots are from this study; thin, solid, dotted and broken line are from Kanda et al. (2004)..... 4-6

Figure4-7: Vector maps of two characteristic flow patterns. Strong upward wind occur within the canopy in both instantaneous flow fields and the condition A is satisfied ($u' < 0$, $w' > 0$ are fulfilled more than 60% of measurement points in shaded square in figure 4-4)109

Figure4-8: (a) and (b) Instantaneous flow fields captured at 26.780s and 26.760s after experiment began, both two satisfied condition A. (c) and (d) vector views produced by subtracting convective wind speed ($U_c=0.25$) from figure 4-8 (a) and (b) according to the method Adrian et al . (2000) developed. 110

Figure 4-9 (a)Vertical cross section of hairpin packet structure, (b)Flow structure around a hairpin vortex (Adrian et al. 2000) 111

Figure4-10: (a) and (b) Vector maps of two characteristic flow patterns. Strong downward wind occurs above the canopy and it penetrates into canopy. The threshold B is satisfied in both flow field ($u' > 0$, $w' < 0$ are fulfilled more than 60% of measurement points in shaded square in figure 4-4) 112

Figure4-11: (a), (b) and (c) Instantaneous flow patterns at the moment when strong bent flow observed at the canopy roof height. Figure 4-10(d) Vector views produced by subtracting convective wind speed ($U_c = 0.35$) from figure 4-10(a) 113

Figure5-1: Canyon flow, air ventilation, and drag force124

Figure5-2: Side views of experimental setting (a)PIV, (b)Drag coefficient127

Figure5-3: Diagrams of 2D street canyon models. Gray lines: separated measurement areas, black lines: regions where experimental data has high accuracy above the canyons.128

Figure5-4: Histograms of particle displacement under different conditions of final interrogation window size in case A. (a) Streamwise displacement ($\Delta x[\text{pixel} / \Delta t]$), (b) Vertical displacement ($\Delta z[\text{pixel} / \Delta t]$). Dashed line: 21×21 pixel, solid line: 15×15 pixel, dotted line: 9×9 pixel.....131

Figure5-5: Temporally averaged velocity vector maps, (a) Case A (L/H=3, no eaves), (b) Case B (L/H=3, having eaves), (c) Case C (L/H=5, no eaves), (d) Case D (L/H=5, having eaves), (e) Case E (L/H=7, no eaves), (f) Case F (L/H=7, having eaves).....134

Figure5-6: Spatial distributions of standard deviations of streamwise velocity component normalized by reference wind velocity (σ_u/U_{20H}), (a) Case A (L/H=3, no eaves), (b) Case B (L/H=3, having eaves), (c) Case C (L/H=5, no eaves), (d) Case D (L/H=5, having eaves), (e) Case E (L/H=7, no eaves), (f) Case F (L/H=7, having eaves)138

Figure5-7: Spatial distributions of standard deviations of vertical velocity component normalized by reference wind velocity (σ_w/U_{20H}), (a) Case A (L/H=3, no eaves), (b) Case B (L/H=3, having eaves), (c) Case C (L/H=5, no eaves), (d) Case D (L/H=5, having eaves), (e) Case E (L/H=7, no eaves), (f) Case F (L/H=7, having eaves)140

Figure5-8: Snapshots of typical flow motions near eaves, (a) high-speed downward flow near $x/H=2.1$ in case B (within the squares with gray dashed lines in Figure 5-6(b) and Figure 5-7(b)), (b) and (c) low speed reverse flow and high speed forward flow above the eaves (within the squares with gray dashed lines in Figure 5-6(f)).....141

Figure5-9: Spatial distributions of Reynolds stress normalized by reference wind velocity ($-\overline{u'w'}/U_{20H}^2$), (a) Case A (L/H=3, no eaves), (b) Case B (L/H=3, having eaves), (c) Case C (L/H=5, no eaves), (d) Case D (L/H=5, having eaves), (e) Case E (L/H=7, no eaves), (f) Case F (L/H=7, having eaves).143

Figure5-10: Spatial distributions of two point correlation coefficients of streamwise velocity component (R_{uu}) with reference points located below the canyon roof height (white dashed lines), (a) Case A (L/H=3, no eaves), (b) Case B (L/H=3, having eaves), (c) Case C (L/H=5, no eaves), (d) Case D (L/H=5, having eaves), (e) Case E (L/H=7, no eaves), (f) Case F (L/H=7, having eaves)·146

Figure5-11: Spatial distributions of two point correlation coefficient of streamwise velocity component (R_{uu}) with reference points located above the canyon roof

height (white dashed lines), (a) Case A (L/H=3, no eaves), (b) Case B (L/H=3, having eaves), (c) Case C (L/H=5, no eaves), (d) Case D (L/H=5, having eaves), (e) Case E (L/H=7, no eaves), (f) Case F (L/H=7, having eaves)..148

Figure5-12: Spatial distributions of two point correlation coefficient of vertical velocity component (R_{ww}) with reference points located below the canyon roof height (white dashed lines), (a) Case A (L/H=3, no eaves), (b) Case B (L/H=3, having eaves), (c) Case C (L/H=5, no eaves), (d) Case D (L/H=5, having eaves), (e) Case E (L/H=7, no eaves), (f) Case F (L/H=7, having eaves)150

Figure5-13: Spatial distributions of two point correlation coefficient of vertical velocity component (R_{ww}) with reference points located above the canyon roof height (white dashed lines), (a) Case A (L/H=3, no eaves), (b) Case B (L/H=3, having eaves), (c) Case C (L/H=5, no eaves), (d) Case D (L/H=5, having eaves), (e) Case E (L/H=7, no eaves), (f) Case F (L/H=7, having eaves)152

Figure5-14: Canyon ventilation rate; $Q \cdot T/V$ and $Q_m \cdot T/V$154

Figure5-15: Drag coefficient (C_d) in each case. C_d of a smooth surface induced by equation 5-5 (hino, 1992) is also presented156

List of Tables

Table1-1: Method and purpose of the studies	4
Table2-1: Growth of the environmental department of Kitakyushu city (data from Taketoshi 2002).....	36
Table2-2: Proportion of jobs in 1970 and 2006 (data from Seltmann 2006)	39
Table2-3: Water pollution and process of social activities in Kitakyushu and Emscher area	44
Table2-4: Key factors to construct sustainable society in the two regions.....	48
Table3-1: List of past PIV experiments conducted in wind engineering and urban atmospheric boundary layer science	60
Table3-2: Experimental conditions of past PIV experiments in a large size boundary layer wind tunnel	66
Table3-3: Quality of the raw image of modified image	80
Table5-1: Spatial resolution and measurement duration	130
Table5-2: Location of the reference points in each case.....	145

CHAPTER I

Introduction

1.1 Background and motivation

From the middle of the 18th century, the progress of modernization and industrialization have drastically increased the amount of production (Bairoch, 1982), and established the life style which is characterized by mass production, mass consumption and mass disposal (White paper of Japanese environmental authority, 1999). However, this social development have increased environmental burden, and caused serious environmental problems. Especially, in urban areas, materials and energy have been intensively consumed, and it caused the environmental problems peculiar to urban areas such as atmospheric pollutions and heat island. The adverse effect on health of the urban residents has become serious, and recently the number of health incidents has been reported. According to Mu and Zhang (2013), the number of patients with respiratory diseases associated with air pollution in Beijing has drastically increased, and their survey estimates the health loss at 446 billion yen. Thus, it is considered that the sustainable development of urban areas will not be accomplished without checking the deterioration of environment and realizing an urban environment which assure the health of urban residents.

Analyzing the causing process of environmental disruption in urban areas, it is largely classified into two. The first one is industrial pollution especially associated with the emission from heavy industries, and the other is life pollutions caused by excessive concentration of population in urban areas. In regard to the former, the causing

mechanism is relatively simple, namely, there is a specific source and it pollutes environment. In other words, the relation between perpetrators and victims is obvious. Although many cases have been reported in the developing countries even in the present days, a number of incidents occurred in developed countries in the early and middle of the last century were solved owing to the environmental technologies. On the other hand, the latter has been caused nowadays in large cities of both developing and developed countries such as Tokyo and Beijing. Moreover, a survey conducted by United Nations Population in 2015 indicates the concentration of population to urban areas will accelerate in the future, and more than 70% of the world population will live in urban areas until 2050. Thus, it is expected that the environmental burden associated life will continuously increase in the future. The generation mechanism of the latter is different from the former. Specifically, it is caused by the integration of small amount of heat and pollutant emission from living activity. In other words, the relation between perpetrators and victims is unclear centrally to the former.

Against the industrial pollution, several past studies indicate the scientific knowledge play an important role for solving them. For example, emission control systems played an important role to solve past industrial pollution caused by the emission from heavy industries in Japan (e.g. Kishimoto 2011, Matsunaga 2004). Additionally, past studies revealed the importance of social phenomenon to solve the industrial pollution. The anti-air and water pollution law of Japan before 1970 described that the environment should be protected under the harmonization of economic development. In other words, the social trend at that time comprehended ecology as an antinomy of economy, and it is frequently pointed out it delayed to take countermeasures for environmental pollutions. However, under such circumstance, several pioneering areas (e.g. Kitakyushu and

Kawasaki) established their own development strategies, and now they are well known as typical models which are achieving sustainable development under the balance of economy and ecology. Although the causal relationship of life pollution is complicated compared to industrial pollution described above, it is obvious that the combination of science and social technology is needful. For example, for the air pollution, scientific research of urban meteorology investigate the diffusion process of polluted materials emitted from cars and buildings associated with the wind conditions in urban areas, and nowadays these data occupy the important positions of urban planning.

1.2 Approaches and objectives

As the reason described above, this study takes approaches from the viewpoints of wind engineering and comparative sociology (table 1-1).

Natural wind is expected as a driving force to remove pollutant materials emitted from buildings and cars, and it can moderate severe thermal stress in summer season in low and middle latitude countries. The wind environment in urban areas is strongly influenced by surface topology, which is formed by arrangements of buildings and vegetation as well as shape and height of buildings. Thus, understanding the relationship between urban wind environment and geometrical characteristics is significantly important for achieving a desirable urban environment. In this study, turbulent flow fields in the vicinity of scaled urban building models (1000 to 1 scale compared to the real buildings) were investigated by wind tunnel experiments, employing a particle image velocimetry (PIV) method.

On the other hand, based on sociological approach, the process of social consensus formation for the construction of a sustainable society was investigated through the comparative study on environmentally pioneering regions in Japan and Germany. It is no

Table 1-1 Method and purpose of the studies

	Method	Purpose
Comparative sociology	Comparative analysis on pioneering models	Extract key mechanisms of social change
Wind engineering	Wind tunnel experiment with scale building model	Reveal the relation between urban geometry and physical nature of turbulent flow

exaggeration to say that the formation of robust social consensus among numerous stakeholders including public organizations, private companies and individuals is the most important point to build pleasant urban environments as the past examples shows (Shikata 1991; Seltmann 2007). In this study, the histories of the two regions for over the past 100 years were compared each other, and then the essential factors why these two regions have succeeded in becoming environmentally friendly societies were extracted.

1.2.1 Social consensus for the construction of an environmentally friendly society

According to the annual report of Environmental Agency of Japan in 1999, the public awareness of environmental pollution was raised in 1960s. In this period, a large amount of emissions of waste materials from heavy industries caused serious pollution (e.g. four major environmental cases in Japan), and strong protests against the industrial pollution were conducted in industrialized countries of those days. The social movements played an important role to force private companies and national governments to take measures, and such environmental disruption was solved almost completely by developments of technologies and legal systems. Furthermore, the social attitude making much of environmental quality has continued until the present days, and has contributed to establish environmentally conscious society.

This social change has attracted much attention from researchers of social science: politics (e.g. Taketoshi 2002; Nomura 2011), economics (Matsunaga 2004; Sun 2004; Seki 2009), and sociology. These studies overview the histories of the regions where serious environmental pollution happened in the past, and extract the primal factors which brought the social changes toward sustainable societies. Learning from these contributions, this study focuses two areas which are well-known as models of sustainable regions in the present days though serious contamination occurred in the past, and investigates their histories over the past 100 years. Common factors between these two regions are also revealed through the intercomparison analysis.

1.2.2 Turbulent flow fields around scaled models of urban buildings

Figure 1-1 is the schematic of the climatic scale and the vertical structure of the urban boundary layer (UBL) (Oke 2006). The influence of mechanical shear of the urban roughness on the boundary layer appears in the surface layer and it is divided into three layers in the vertical direction: urban canyon layer (UCL); roughness sublayer (RSL); inertial sublayer (ISL) (figure 1-1 (b) and (c)).

UCL is located at the bottom of the ULB, and the top height of UCL is usually determined as the maximum building height. The influence of roughness on flow fields is significantly large, and time-averaged flow field structures is heterogeneous in space. Furthermore, wake flow, eddies, flow separation, and flow reattachment are caused around the roughness, forming complex flow fields. RSL is the layer from the ground surface to the height of several times of the average building height (according to Cheng and Castro 2002, 2-5 times of building height). The flow fields is still heterogeneous in a horizontal plane in RSL reflecting the geometrical characteristics of urban roughness. In

contrast, in ISL, the flow fields become almost horizontally uniform and temporally averaged velocity (U [m/s]) obeys logarithmic law (Eq.1-1) .

$$\frac{U}{u^*} = \frac{1}{\kappa} \ln\left(\frac{z-d}{z_0}\right) \quad (1-1)$$

Here, z_0 [m] is the roughness length and indicates a length scale of the magnitude of the surface shear, d [m] is the displacement height and means the central height of momentum absorption by roughness (Jackson 1981), κ is Karman constant, and u^* [m/s] is the friction velocity.

In order to reveal the relationship between the nature of turbulent flow fields and urban geometrical conditions, researchers have conducted a various types of studies in accordance to the research targets. On the basis of the temporal and spatial scale of the research targets, the past studies can be roughly categorized as the following three types: temporally-specially average; temporal-average and spatial-distribution; and temporal-spatial variation (figure 1-2).

1) Temporally-spatially averaged

In a traditional approach, the impact of urban roughness elements on the boundary layer has been described by bulk-scale aerodynamic parameters, including z_0 and d and drag coefficient (C_d , indicates the total shear stress on surface or momentum deficit by roughness elements). z_0 and d are included in logarithmic law (eq.1-1) which is valid in ISL where the effect of individual urban obstacle does not appear any more, thus, these two parameters indicate the spatially averaged aerodynamic influence of roughness (figure 1-1 (b)). While C_d is converted to u^* by equation 1-2, and used in the logarithmic law as a representative velocity scale.

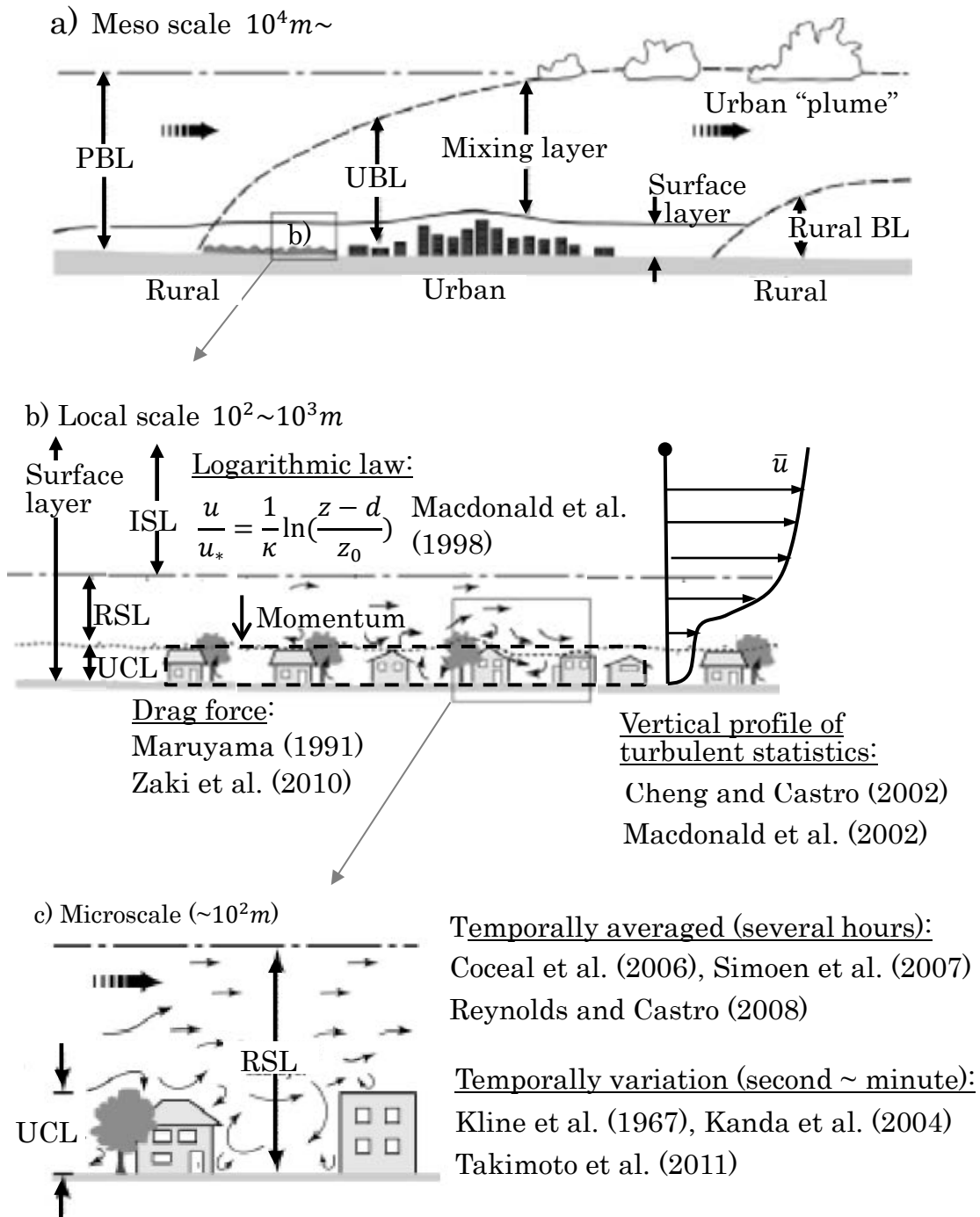


Figure 1-1 Schematic of climatic scales and vertical layers found in urban area. PBL(planetary boundary layer), UBL(urban boundary layer), UCL (urban canopy layer) and related studies in each scales. Representative studies in urban climatology and their targets are also presented (quoted from Oke 2006, and modified by author)

$$\frac{u^*}{U_{ref}} = \sqrt{0.5C_d} \quad (1-2)$$

Here, U_{ref} [m/s] is the reference mean speed.

The relation between an urban geometry and these aerodynamic parameters is expressed by the urban geometrical parameters such as frontal area index (λ_f , ratio of the vertical area of the building seen from the approaching wind direction to lot area); building covering ratio (λ_p , ratio of building roof to lot area). Macdonald et al. (1998) is one of the most monumental achievements using this approach. They theoretically derived mathematical models of z_0 and d as a function of λ_f and λ_p . Compared to the classical models such as Lettau (1969), Macdonald's model is applicable for wide range of building packing density, and can reproduce a convex distribution of z_0 against λ_p .

Furthermore, recent studies have investigated the variation of the aerodynamic parameters against urban geometry taking account of more wide variety of geometrical parameters such as the roughness layout and building height variability. For example, Cheng and Castro (2002) and Hagishima et al. (2009) conducted wind tunnel experiments for rectangular block arrays with uniform and non-uniform heights, and reported the non-uniformity of the roughness height increases drag force and z_0 compared to the case with uniform roughness height. Similar tendency is presented by the large eddy simulation (LES) conducted by Kanda (2006) using both square and staggered arrays with wide variety of λ_p . Zaki et al. (2010) investigated the effect of the randomness of building array by a wind tunnel experiment. Namely, each blocks are randomly rotated horizontally keeping the average angle is 0° . Their experimental results indicate the drag force and z_0 of random arrays is larger compared to those of uniform staggered arrays.

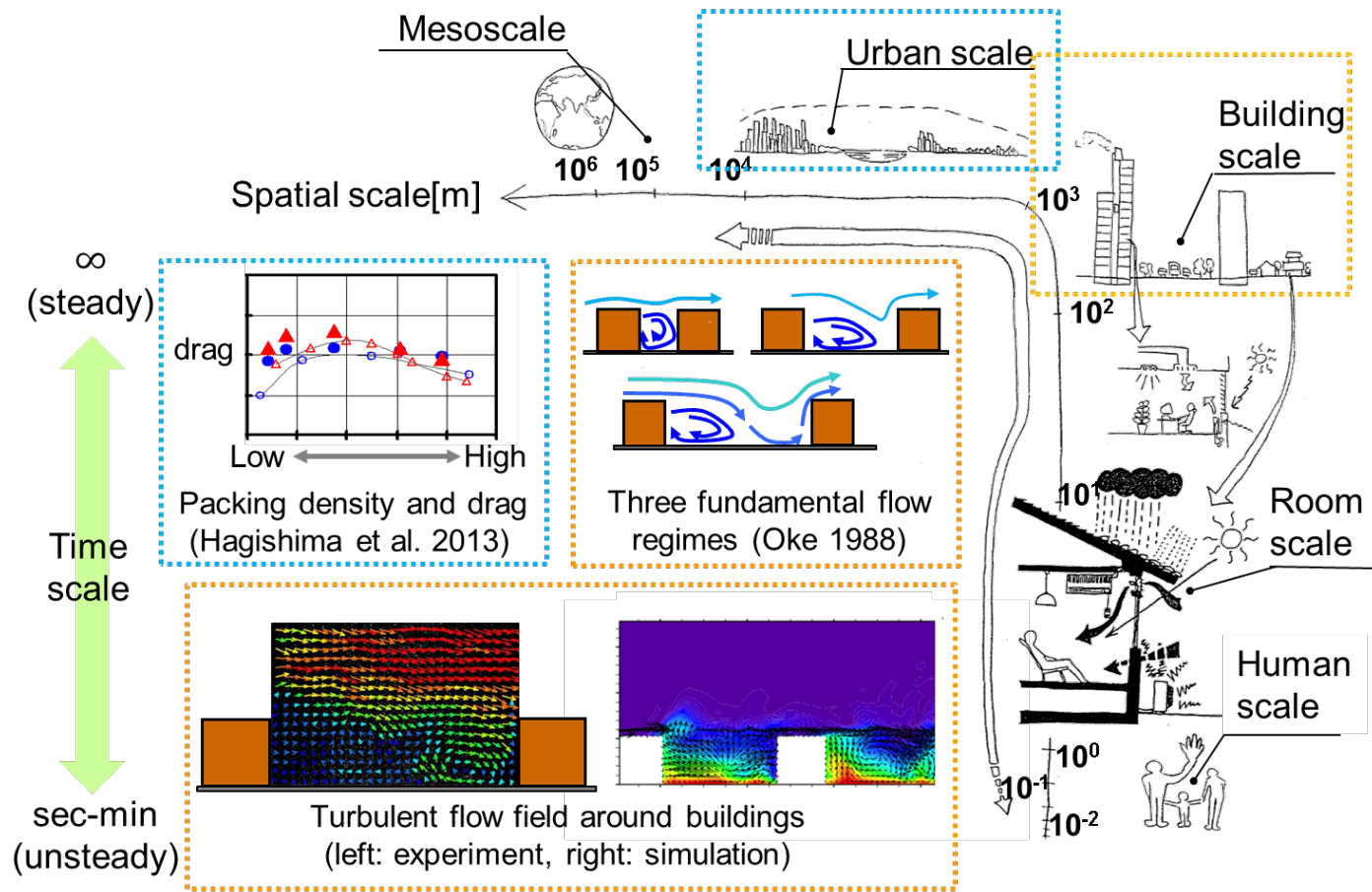


Figure 1-2 Schematic of time and spatial scales of target flow fields of past research in urban climatology

A reasonable explanation of this difference is that strong counter rotating eddies don't arise behind blocks in the random array, making it difficult to form skimming flow within the canopy. The large scale LES conducted by Kanda et al. (2013) using a real geometrical data of Tokyo and Nagoya provided a highly useful database of z_0 and d . From their calculation results, five parameters: λ_p , λ_f , averaged building height, maximum building height, and standard deviation of building height were identified as dominate parameters to determine aerodynamic features of roughness, and new mathematical models of z_0 and d were proposed incorporating these parameters into the models provided Macdonald et al. (1998).

2) Temporal-average, spatial-distribution

Another traditional approach is the analysis on spatial distributions of temporally averaged turbulent statistics, such as mean wind velocity, standard deviation, and Reynolds stress.

A vast number of experiments and numerical simulations have investigated vertical profiles of turbulent statistics in urban boundary layers with various types of roughness conditions (Krogstad and Antonia 1992; Cheng and Castro 2002; Takie and Adame. 2007). The vertical profiles of turbulent statistics are highly important to investigate the turbulent similarity. Macdonald et al. (2002) conducted a wind tunnel experiment for seven types of roughness conditions: 2D street canyon with $\lambda_f = 16\%$, square and staggered arrays with $\lambda_f = 6.25\%$, 16% , and 44% , and presented the standard deviations of streamwise, vertical, and spanwise velocity component ($\sigma_u, \sigma_w, \sigma_v$) in ISL can be scaled by the friction velocity calculated from the Reynolds stress at the same height. Namely, σ_u/u_* , σ_w/u_* , σ_v/u_* keep constant values (2.1, 1.65, and 1.2, respectively) in ISL

regardless of the roughness of the roughness condition. According to the comprehensive review of field experiments by Roth (2000), this scaling method is valid in the full scale urban atmospheric boundary layer. Jimenez (2004) mentions that the turbulent similarity over the several times of roughness heights can be established if the boundary layer depth is over 40-folds of roughness height.

Meanwhile, spatial distributions of turbulent statistics in UCL and RSL with highly complicated structures have been revealed in detail in recent studies owing to the developments of computational fluid dynamics (CFD). Coceal et al. (2006) conducted a direct numerical simulation (DNS) for flow over three types of cubic arrays: square, aligned and square arrays with $\lambda_p = 25\%$, and presented the temporally averaged flow field structures and spatial distributions of turbulent statistics in the vicinity of cubic roughness. Leonardi et al. (2003) conducted DNS for 2D street canyons with 10 different canyon aspect ratio (the ratio of canyon width and roughness height) from 0.33 to 19, and described the transition of the temporally averaged flow field structures with canyon aspect ratio. Their calculation results reproduce the features of three fundamental flow regimes presented by Oke (1988), and size of recirculation flow, location of flow reattachment to the bottom of the canyon, and shape of the secondary vortex behind a wind ward building are determined clearly. In addition to CFD, the developments of particle image velocimetry (PIV) technique has made it possible to obtain flow field data around roughness with high spatial resolution in wind tunnel experiments. For example, PIV experiment for cubic staggered arrays with $\lambda_p = 25\%$ by Reynolds and Castro (2008) presents a vector map of temporally averaged flow field in UCL, and it corresponds well with the result of the numerical simulation by Coceal et al. (2006). Salizzoni et al. (2011) and Annalisa et al. (2015) demonstrated the spatial distributions of Reynolds stress within

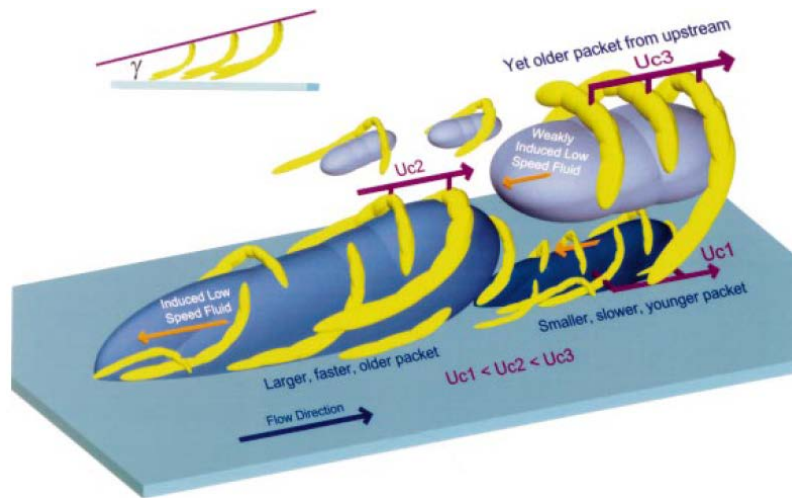


Figure 1-3 Conceptual diagram of turbulent organized structure (hairpin packets structure) growing up from the wall (quoted from Adrian et al. 2000).

2D street canyons, and investigated the momentum transport process between the regions above and inside the street canyons.

3) Temporal and spatial variation

At a first glances, turbulent flow fields seems to be random, however, in actual fact, it is not completely mess and contains coherent structures. Kline et al. (1967) visualized low speed streak-like structures extending in the streamwise direction over a smooth surface using smoke wire, while Grass et al. (1971) visualized streak-like structures of water flows over both a smooth and rough surface comprised of small stones by using air bubbles scattered in a water channel. The understanding of turbulent coherent structures has greatly progressed in the late of 20th century by the developments of both PIV and CFD. PIV experiment by Adrian et al. (2000) demonstrated snapshots of vertical cross section of hairpin packet structures, which consists of horseshoe vortices connected in the streamwise direction (figure1-2) over a smooth surface. Similarly, Zhou (1999) presented

3D structures of hairpin packet structures over a smooth surface by DNS simulation.

Low speed streak-like structures and hairpin packet structures arise over 2D street canyons (e.g. Leonardi et al. 2004) and 3D urban type building models (e.g. Kanda et al. 2004, Kanda, 2006). Coceal et al. (2007) conducted DNS of flow over the cubic staggered array with $\lambda_p = 25\%$, and revealed the streamwise length of low speed streak is reduced while the spanwise length increases compared to the streak-like structure over a smooth surface. Takimoto et al. (2012) compared the scale of turbulent structures over four different roughness conditions: smooth surface, square arrays with uniform and nonuniform building height, and 2D street canyons by the two point correlation method. They indicated the ratio of streamwise and spanwise length of turbulent structures are highly correlated with the streamwise velocity gradient in the vertical direction, and furthermore, they found the similar relation between the velocity gradient and horizontal/spanwise scale ratio of turbulent structures for all roughness conditions.

Meanwhile, intermittent turbulent coherent motions in UCL characterized by low speed upward flow (ejection) and high speed downward flow (sweep) have been one of curious research topics of the recent studies. Takimoto et al. (2009, 2011) presented snapshots of ejection and sweep flow patterns in UCL based on an outdoor experiment within a cubical array with 1.5m. These flow motions arise once in several minutes and occupy almost entire region of a canyon, and stimulate the momentum transport between above and inside a canyon. LES simulations by Inagaki et al. (2011), Michioka et al. (2011), and Michioka et al. (2014) demonstrated that strong ejection flows are caused in UCL in association with the passing of low speed streaks above the roughness, instantaneously increasing the scalar and heat transport from UCL .

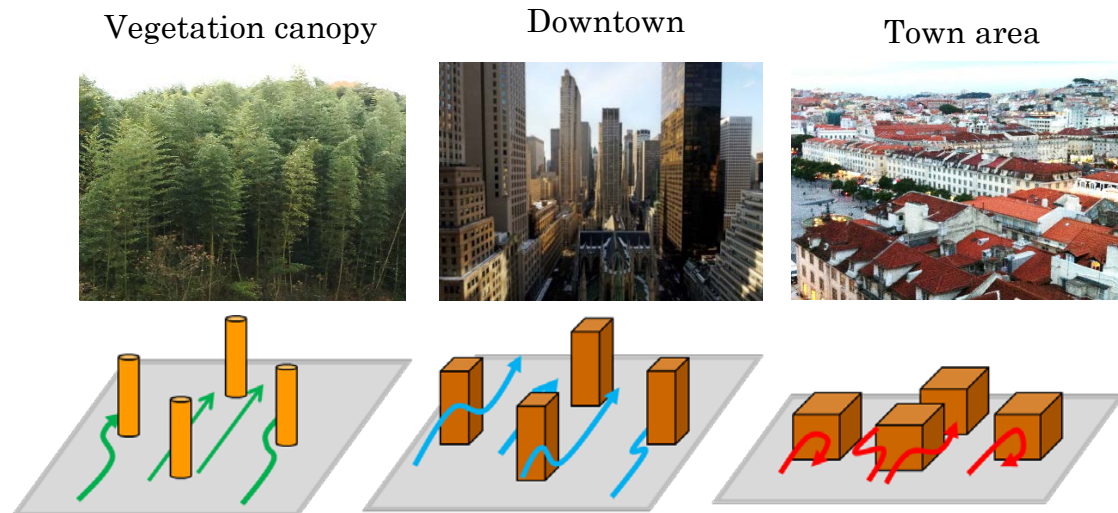


Figure 1-4 Conceptual diagram of flow fields around different shapes roughness models

Among these, in this study, turbulent flow fields in UCL and RSL was investigated from the view of the second and third approach based on the results of wind tunnel experiments with PIV technique. In these wind tunnel experiments, the following two roughness models were employed: a 3D urban roughness model which consists of regularly arranged slender rectangular blocks, and 2D street canyons of simple and complex building shapes.

The former model imitates a downtown area with many high-rise buildings. In most of the past studies of urban boundary layer science, roughness arrays consist of cubes or short blocks with low aspect ratio (ratio of frontal area to roof area) have been used. Although these results of these studies contribute for modeling the flow fields in residential districts of detached houses, airflow characteristics in dense urban districts are difficult to be modeled. As it was mentioned earlier, it is expected that the population concentration to city areas will proceed in the future, thus, it is considered meaningful to investigate the flow field property around high-rise buildings. Furthermore, the flow

around slender block models is an interesting from an aerodynamic point of view. Slender rectangular blocks are considered to be more streamlined than cubic roughness, while less streamlined than cylinder roughness imitating vegetation canopy (figure 1-3). Actually, several past studies indicate the turbulent flow properties around cubes and slender rectangular blocks are different from each other (e.g. Huq et al. 2007, Hagishima et al. 2012). Fortunately, the nature of turbulent flow fields around vegetation canopies has been investigated more than several decades ago (e.g. Kanda and Hino 1994, Raupach et al. 1996, Finnigan 2000), thus, the difference and similarity among turbulent flow fields with the three types of roughness conditions can be discussed.

On the other hand, the later roughness model is used in order to investigate how complexity of urban surface topology affects the nature of turbulent flow fields. Most of the past studies highly simplified real urban geometry and used idealized block arrays such as 2D street canyons and cubic arrays, however, in general, real urban surfaces include diverse and complicated topography derived from secondary roughness such as balconies, porch and penthouses. These sub-constructions attach to main buildings might have a significant influence on the flow fields especially in UCL and RSL, and the urban air ventilation and scalar emission efficiency also might be changed. Thus, it is considered important to take complexity of building shapes into account for realizing the pleasant urban environment.

Several recent studies conducted experiments and simulations using complex shape building models. For example, Reynolds Averaged Navie Stokes (RANS) simulations (Huang et al. 2009, Takano and Moonen 2013, Mohamad et al. 2014) revealed the effect of complex roughness shapes on temporally averaged flow fields, while PIV experiment conducted by Kellnerova et al. (2012) and LES by Takano et al. (2015) examined how

the typical turbulent flow structures are affected by different roof shapes. However, the existing data of the influence of complex urban topology on unsteady turbulent flow fields is still limited, and more data is required to establish the holistic features. Thus, this study conducts PIV experiments using both simple and complex shape roughness in order to provide a high standard experimental data which present the influence of the complexity of shape of roughness on turbulent flow fields.

1.3 Structure of thesis

This thesis is organized into six chapters as follows:

- Chapter II is the study on the formulation process of sustainable society by comparative analysis on pioneering regions. Through the intercomparison of regional histories of two environmentally pioneering societies in Japan and Germany, essential factors which derived the social movement for constructing the sustainable society are revealed.
- Chapter III investigates the measurement accuracy of PIV experiments for unsteady turbulent flow fields around scaled urban building models. PIV has useful features to investigate complicated structures of unsteady three dimensional turbulent flow such as multi point measurement with high spatial resolution and contactless measurement. However, it is known that measurement accuracy is strongly affected by various experimental setting, thus, it is still a difficult measurement methods. Especially if a measurement is conducted in a large size atmospheric boundary layer wind tunnel, a bias error called as peak locking frequently occurs. Thus, in chapter III, the cause of this problem is discussed in light of the physical theory of PIV measurement, then a countermeasure for the problem is demonstrated.

- Chapter IV presents the results of a PIV experiment on the turbulent flow fields around high rise building models. First, the spatial distributions of turbulent statistics in UCL and RSL are presented, and the similarity with turbulent flow field around cubic and vegetation canopies are discussed. The characteristic instantaneous flow patterns are subsequently identified from instantaneous flow field data, and the relationship between these flow patterns and turbulent organized structure above the roughness models are shown.
- Chapter V reports the results of wind tunnel experiments on turbulent flow fields around 2D street canyons with and without flat eaves to investigate how the complexness of roughness geometry affects the turbulent flow fields by using PIV. The temporally averaged flow fields, spatial distributions of turbulent statistics, and turbulent coherent structure are discussed in detail. In addition, it is discussed how the difference of turbulent flow natures affect urban ventilation and the bulk drag force.
- Chapter VI summarizes the main contribution of previous four chapters.

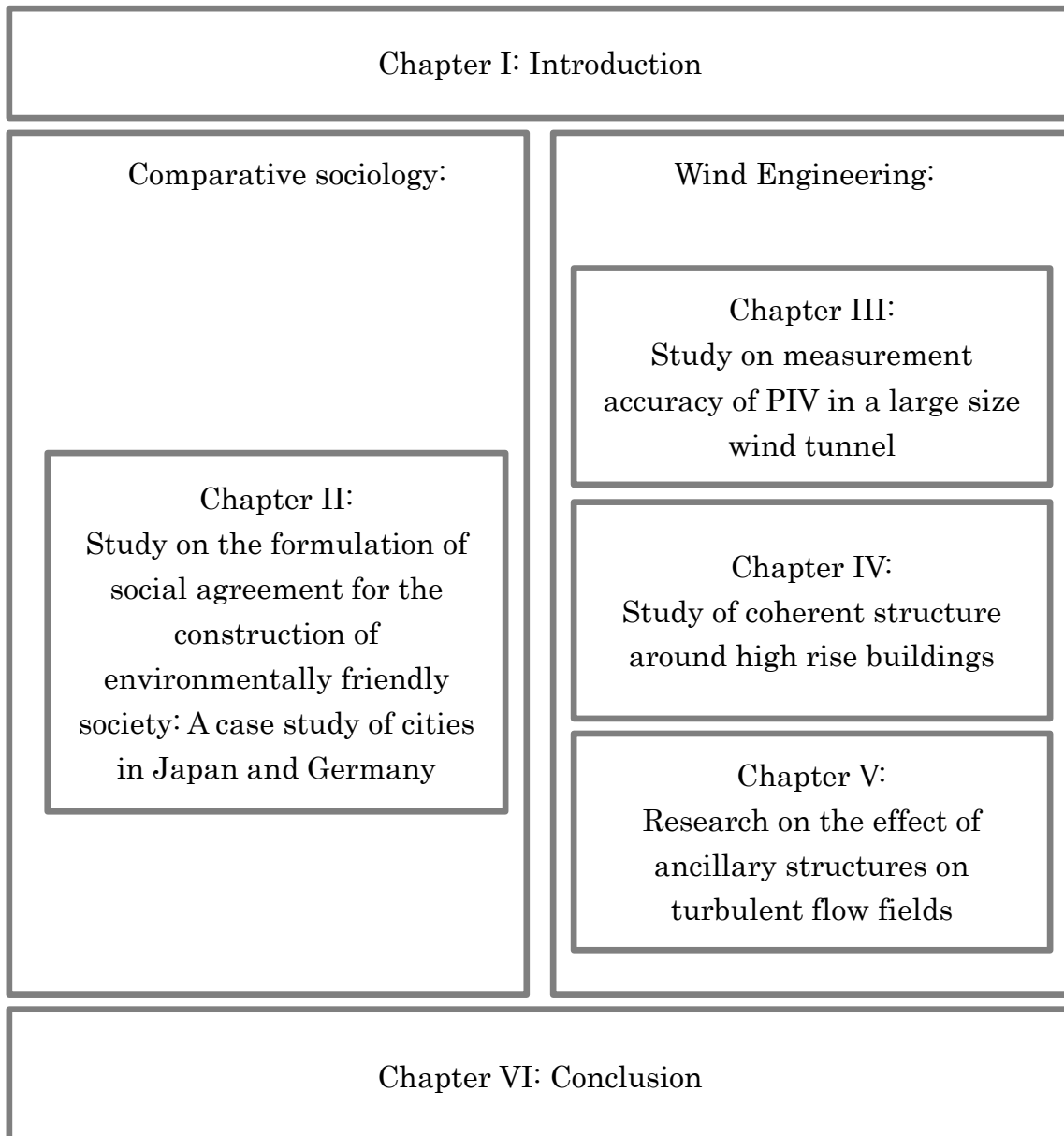


Figure 1-5 Structure of thesis

Reference

- Adrian, R. J., Meinhart, C. D., Tomkins, C. D. (2000) Vortex organization in the outer region of the turbulent boundary layer, *Journal of Fluid Mechanics*, vol. 422, pp.1-54
- Bairoch, P. (1982). International industrialization levels from 1750 to 1980. *The journal of European economic history*, vol.11, pp. 269-333
- Cheng, H., Castro, I. P. (2002) Near wall flow over urban-like roughness, *boundary-layer meteorology*, vol.104, pp. 229-259
- Claus, J., Coceal, O., Thomas, T. G., Branford, S., Belcher, S. E., Castro, Ian P. (2012) Wind-Direction Effects on Urban-Type Flows, *boundary-layer meteorology*, vol. 142, pp. 265-287
- Coceal, O., Thomas, T. G., Castro, I. P., Belcher, S. E. (2006) Mean Flow and Turbulence Statistics Over Groups of Urban-like Cubical Obstacles, *boundary-layer meteorology*, vo. 121, pp.491-519
- Coceal, O., Dobre, A., Thomas, T. G. (2007) Unsteady dynamics and organized structures from DNS over an idealized building canopy, *international journal of climatology*, vol.27, pp. 1943-1953
- Flack, K. A., Schultz, M. P., Shapiro, T. A. (2005) Experimental support for Townsend's Reynolds number similarity hypothesis on rough walls, *Physics of Fluids*, vol. 17, 035102-1, 035102-9
- Grass, A. J. (1971) Structural features of turbulent flow over smooth and rough boundaries, *Journal of Fluid Mechanics*, vol.50, pp.233-255
- Hagishima, A., Tanimoto, J., Nagayama, K., Koga, M. (2007) Wind tunnel experiment on drag force coefficient of regular arrayed rectangular blocks with different heights, *Journal of Environmental Engineering (Transactions of AIJ)*, no.619, pp.39-45
- Hagishima, A., Tanimoto, J., Nagayama, K., Meno, S. (2009) Aerodynamic Parameters of Regular Arrays of Rectangular Blocks with Various Geometries, *boundary-layer meteorology*, vol. 132, pp.315-337
- Inagaki, A., Castillo, M. C. L., Yamashita, Y., Kanda, M., Takimoto, H. (2011) Large-eddy simulation of coherent flow structures within a cubical canopy, *boundary-layer meteorology*, vol.142, pp.207-222

- International Union for Conservation of Nature and Natural Resources (1980). World Conservation Strategy.
- Jackson, P. S. (1981) On the displacement height in the logarithmic velocity profile, *J. F. mech.*, vol. 111, pp.15-25
- Jimenez, J. (2004) Turbulent flows over rough walls, *annual review of fluid mechanics*, vol. 36, pp.173-196
- Kanda, M., Moriwaki, R., Kasamatsu, F. (2004) Large eddy simulation of turbulent organized structures within and above explicitly resolved cube, *boundary-layer meteorology*, vol. 112, pp. 343-368
- Kanda, M. (2006) Large-eddy simulations on the effects of surface geometry of building arrays on turbulent organized structures, *boundary-layer meteorology*, vol.118, pp. 151-168
- Kanda, M., Inagaki, A., Miyamoto, T., Gryschka, M., Raasch, S. (2013) A New Aerodynamic Parametrization for Real Urban Surfaces, *boundary-layer meteorology*, vol. 148, pp.357-377
- Kellnerova, R., Kukacka, L., Jurcakova, K., Uruba, V., Janour, Z. (2012) PIV measurement of turbulent flow within a street canyon: Detection of coherent motion, *journal of wind engineering and industrial aerodynamics*, vol. 104-106, pp. 302-313
- Kline, S. J., Reynolds, W. C., Schraub, F. A., Runstadler, P. W. (1967) The structure of turbulent boundary layers, *journal of fluid mechanics*, vol.30, pp.741-773
- Krogstad, P. A. Antonia, R. A. (1992) Comparison between rough- and smooth-wall turbulent boundary layers, *journal of fluid mech.* vol. 245, pp. 599-617
- Lettau, H. (1969) Note on aerodynamic roughness parameter estimation on the basis of roughness element description, *journal of applied meteorology*, vol.8, pp.828-832
- Leonardi, S., Orlandi, P., Smalley, R. J., Djenidi, L., Antonia, R. A. (2003) Direct numerical simulations of turbulent channel flow with transverse square bars on one wall, *journal of fluid mechanics*, vol.491, pp.229-238
- Macdonald, R.W., Griffiths, R.F., Hall, D.J., (1998) An improved method for the estimation of surface roughness of obstacle arrays, *Atmospheric Environment*, vol.32, pp.1857-1864

- Macdonald, R. W., Schofield, S. C., Slawson, P. R. (2002) Physical modelling of urban roughness using arrays of regular roughness elements. *Water, Air and Soil Pollution: Focus*, 2(5-6), 541-554.
- Maruyama T. (1991) On drag variation due to array patterns of cubic blocks (in Japanese), *journal of wind engineering*, vol. 49, pp.15-24
- Matsunaga, H. (2004) Agglomeration of the heavy and chemical industries and the generation of the environmental industries, *Association of economic geographers*, vol. 50, pp. 325-340
- Michioka, T., Sato, A., Takimoto, H., Kanda, M. (2011) Large-eddy simulation for the mechanism of pollutant removal from a two-dimensional street canyon, *boundary-layer meteorology*
- Nomura, M. (2011) Historical Survey of Environmental Policy in Kitakyushu City up to this day, *KIU journal of economics & business studies*, vol.17, pp.13-22
- Oke, T. R. (1988) Street design and urban canopy layer climate, *energy and buildings*, vol.11, pp.103-113
- Reynolds, R. T., Castro, I. P. (2008) Measurements in an urban-type boundary layer, *experiments in fluids*, vol. 45, pp.141-156
- Roth, B. (2000) Review of atmospheric turbulence over cities, *Q.J.R. Meteorol. soc.*, vol.126, pp.941-990
- Santiago, J. L., Coceal, O., Martilli, A. (2013) How to parametrize urban-canopy drag to reproduce wind-direction effects within the canopy, *boundary-layer meteorology*, vol. 149, pp.43-63
- Sato, T., Hagishima, A., Ikegaya, N., Tanimoto, J. (2013) particle image velocimetry measurement of unsteady turbulent flow around regularly arranged high-rise building models, *international journal of high-rise buildings*, vol. 2, pp. 105-113
- Seki, M. (2009) *Eco town as a local brand*. Shinhyouron press, Tokyo
- Seltmann, G. (2007) Renaissance of an industrial region: “Internationale Bauausstellung Emscher Park achievements and future model for others”. Flechtingen: Gseprojecte office for regional development, pp.1-11 <http://www.riss.osaka-u.ac.jp/jp/events/point/P.Seltmann.pdf> (accessed December 6, 2016)

- Shikata, H. (1991) A town changes smog to star, challenge of Kitakyushu city, Kodansha, Tokyo, Japan
- Simoens, S., Ayrault, M., Wallace, J. M. (2002) The flow across a street canyon of variable width—Part 1: Kinematic description, *Atmospheric Environment*, vol. 41, pp. 9002-9017
- Sun, Y. (2005) The transformation of the Industrial Structure and the Environmental Burden (in Japanese), *The review of welfare society*, vol.4-5, pp. 69-96
- Taketoshi, K. (2002) Antipollution measures and their characteristics in Kitakyushu city, *St. Andrew's University economic and business review*, vol43, pp299-321
- Takimoto, H., Sato, A., Onomura, S., Kanda, M. (2009) PIV measurement of urban canopy turbulence intercomparison study between outdoor and indoor urban scale model (in Japanese), *annual journal of hydraulic engineering*, vol.53, pp.241-246
- Takimoto, H., Sato, A., Barlow, J. F., Moriwaki, R., Inagaki, A., Onomura, S., Kanda, M. (2011) Particle image velocimetry measurements of turbulent flow within outdoor and indoor urban scale models and flushing motions in urban canopy layers, *boundary-layer meteorology*, vol.140, pp.295-314
- Takimoto, H., Inagaki, A., Kanda, M., Sato, A., Michioka, T. (2012) Length-scale similarity of turbulent organized structures over surfaces with different roughness types, *boundary-layer meteorology*,
- Tachie, M. F. and Adane, K. K. (2007) PIV study of shallow open channel flow over d- and k-type transverse ribs, *journal of fluids engineering*, vol. 129, pp.1058-1072
- The ministry of environment in Japan, White paper of the environment in 1999, 1999, <https://www.env.go.jp/policy/hakusyo/hakusyo.php3?kid=211>, (accessed June 30, 2016)
- United Nations. Agenda 21, (1992)
- United Nations Population Division. (2015) World Population Prospects, http://esa.un.org/wpp/documentation/pdf/WPP2010_Volume-I_Comprehensive-Tables.pdf (accessed June 11, 2016)
- White Paper on the Environment; Quality of the Environment in Japan, 1980
- Yoda, S. (1993) Trilemma (in Japanese), Mainichi-Shinbunsha press, Tokyo, Japan

Zaki, S. A., Hagishima, A., Tanimoto, J., Ikegaya, N. (2010) Aerodynamic Parameters of Urban Building Arrays with Random Geometries, *boundary-layer meteorology*, vol. 138, pp. 99-120

Zhou, J., Adrian, R. J., Balachandar, S., Kendall, T. M. (1999) Mechanisms for generating coherent packets of hairpin vortices in channel flow, *Journal of Fluid Mechanics*, vol.387, pp.353-396

CHAPTER II

Study on the formulation process of sustainable society by comparative analysis on pioneering regions in Japan and Germany

2.1 Introduction

Economic development is one of the most important purposes of human society, and urbanization have occurred all over the world. According to Takano (1959), the centralization of capital with the development of modern capitalism has accelerated urbanization. Namely, massive capital investment for heavy industries transforms a rural area into an industrial area, and concentration of economic activity and population to an urban area establish unprecedented scale mega cities such as Tokyo. However, such urbanization has often progressed without taking enough care of the environment. As a result, serious environmental problems such as air pollution in Beijing have been caused, and health risk in urban areas have drastically increased in recent years (e.g. Mu and Zhang 2013). Moreover, it is predicted the urban population continues to increase in the future primarily in developing countries, hence, a more number of people will be exposed to contaminated environments unless any countermeasure will be taken.

Under this circumstance, the concept of sustainable society was proposed as a fundamentally new direction for the future development of human society in the World Conservation Strategy of the International Union for Conservation of Nature and Natural Resources (IUCN) in 1980. There are various definitions of sustainable society, and the most important theme is that all resources such as air, water, mineral resources and bioresource should be shared with future generations, and we have a duty to preserve the

environment to assure healthy lives of future generations. This fundamental concept took concrete form after the issues to work on in each field (e.g. economy, industry, wild life preservation) were presented in Agenda 21 which was adopted at the United Nations conference on environment and development at the Earth Summit in 1992.

One of remarkable points of Agenda 21 is that it indicates the importance of subnational regions. Namely, Agenda 21 mentions that an individual action plan for a sustainable development should be established reflecting the circumstances of each region, and the plan must be progressed under the cooperation of stakeholders including subnational government, private companies and citizen group. With the diffusion of the ideas of Agenda 21, nowadays unique action plans have been launched in a number of regions, and continuous efforts to establish an environmentally friendly society have been conducted.

In the present days, there are several well-known regions which accomplished excellent achievements for realizing a sustainable society such as Kitakyushu city in Japan, Freiburg city in Germany, and Vaxjo city in Sweden. These environmentally pioneering regions are attractive research targets of social sciences, and research from a various points of views has been conducted. For example, Taketoshi (2002), Nomura (2011), and Kishimoto (2011) picked up Kitakyushu city as a sample model, and investigated the contribution of the city government to build an environmentally conscious society from the viewpoint of political science. On the other hand, Matsunaga (2004), Sun (2004) and Seki (2009) also focused on Kitakyushu city, and they revealed the reason why environmentally industries such as waste treatment and recycle business succeeded in Kitakyushu city from the view point of economics.

Although these studies introduced many interesting cases about individual challenges

of a region, it is considered that they pay scant attention to universality because large parts of these reports focus only on a single case and comparison among multiple cases is not conducted. This is partly because each pioneering society uses methods that reflect the specific features and actual situations of the locality; thus, there is little commonality by which to compare the respective local policies in detail.

However, as explained earlier, it is expected that more regions and societies will urbanize in the future, causing more environmental pollution and health crises for people. Therefore, it is highly meaningful to discuss general mechanisms for constituting environmentally friendly societies. Thereby, this study picks up two well-known sustainable regions: Kitakyushu city in Japan (figure 2-1(a)), Emscher area in Germany (figure 2-1(b)), and investigates their regional histories over the past 100 years. Then, the success factors common in the two cases are revealed through the intercomparison of the two cases. The cultural, political and historical background of the two regions are much different from each other, however, three common factors are extracted. Finally, it is discussed whether the success factors can be applicable to other regions which face to environmental pollution in the present days.

2.2 Historical backgrounds of the two regions



Figure 2-1 Locations of (a) Kitakyushu and (b) Emscher (red marks)

In this section, the historical backgrounds of the Kitakyushu region and the Emscher area in the past 100 years are reviewed, focusing on the economic and political situations. Comparative investigation reveals that the two regions have similar historical backgrounds from the end of the 19th century to the present day, and the 100-year period is divided into four phases based on the economic and environmental situations.

2.2.1 Period 1: Dawn of heavy industry

Until the end of the 19th century, Kitakyushu was a poor village, and people made a living by inshore fishery. There was no major local industry, and population was small at that time. However, an important turning point came in 1901 after the state-owned Yahata steel factory commenced operation in that year. The steel factory was built under the national policy of wealth and military strength and was one of the most important production bases of Japan. Figure 2-2 is a picture of the landscape of Yahata in 1910, showing Japanese traditional houses and the modern factory next to each other. After 1901, the population of the Yahata area rapidly increased by 40-fold going from less than 2,000 before 1901 to 84,682 in 1917.

One of the most important reasons why a state-owned steel factory was built in Kitakyushu is the rich coal resourcesⁱ. There was a large coal supply center (Chikuhou coalfield) in the vicinity, and the amount of coal production in the Chikuhou coalfield was more than 50% of all coal produced in Japan at that time. Moreover, a large river, the Ongagawa, connects the Chikuhou coalfield with Kitakyushu, and people took advantage of it as a useful water transport route for the coal. The technological standard of the steel industry at that time required large amounts of coal; thus, it was a great benefit for a steel factory to be adjacent to a huge coalfield.

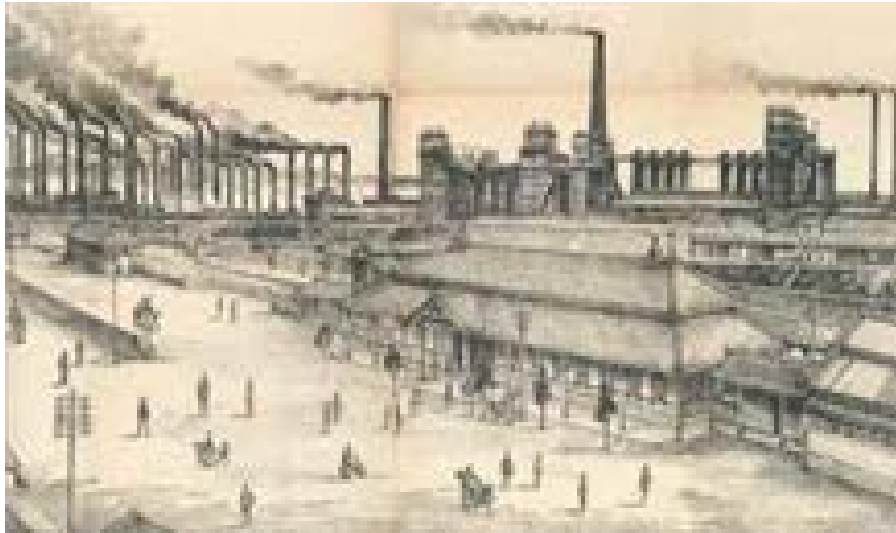


Figure 2-2 Landscape of Yahata region in the early of the 20th century
(quoted from http://meijimeisho.at.webry.info/201305/article_3.html)

One of the remarkable facts of this age is that steel production, which was a leading-edge industry at that time, was started suddenly through the power of the national government. In other words, there was little industrial base in Kitakyushu before 1901, and capital goods and technology were introduced from outside. Yoshio Kanzaki (honorary professor, University of Kitakyushu) has stated that “the process of developing of industry in Kitakyushu is different from the ordinary one, that is, transition from light industry like textile manufacturing to heavy industry. The Yahata steel factory suddenly appeared as state capital in a place where there was no major industry” (e.g. Shikata, 1991), which described this sudden change of local industrial structure as a typical urbanization type that is observed only in the modern era after the Industrial Revolution.

Similar to Kitakyushu, the Emscher area was relatively poor before heavy industry came. Although the south part of the Ruhr industrial area (around the Ruhr River) was one of the most important industrial areas in Germany from the middle of the 19th century, the north part of the area (around the Emscher River) was still undeveloped, and the

population was small.

Development of the Emscher area started with the increase in demand for coal resources in the beginning of the 20th century; a large investment was made by major companies. Similar to the case of Kitakyushu, the industrialization of the Emscher area proceeded rapidly without taking care of the natural environment, and the infrastructure was designed to meet the demands of heavy industry (Nagamatsu, 2006; Seltmann, 2007). In other words, there was plenty of room for development in the Emscher area at that time, and the city structure was tailored for efficient production of coal and steel.

Another feature in common with Kitakyushu was the use of water transport on the Emscher River. Figure 2-3 is the transition of the river from 1899 to 2007. In 1899, it was an aboriginal river with a meandering flow and rich wild life; however, major expansion work were conducted in the early 20th century to change the water flow (figure 2-3(b)). As a result, the Emscher became a regulated artificial river, and was used as a practical water transport route and water drainage system.

2.2.2 Period 2: Golden age and environmental problems

The heavy industry in these two areas grew continuously in the middle of the 20th century. Under the policy of national enrichment, Kitakyushu and the Emscher area played similar roles in Japan and Germany. These two industrial regions were expected to be major production bases for steel, and their products were used for modernization, such as construction of infrastructure and buildings.

Japan had two wars around 1900, the Sino-Japanese War (1894-1895) and the Russo-Japanese War (1904-1905). These two wars increased steel demand under the national policy of wealth and military strength. Social infrastructures developed in consonance

with the operation of the Yahata steel factory, making the Kitakyushu area more inviting private steel production companies and associated industries. As a result, the Kitakyushu region became one of the most important industrial areas of Japan in the 1920s (Kasuga, 1956). After World War II, the Japanese government implemented a priority production systemⁱⁱ and spent enormous amounts of the national budget for revitalization and strengthening of coal mining and steel production. This increased the shipment value of the Kitakyushu industrial area in the middle of the 20th century. Under this circumstance, the five citiesⁱⁱⁱ in the Kitakyushu region were merged to maximize the efficiency of the political system and economic connections among heavy industries; this established the current Kitakyushu city.

Similarly, the Emscher area made a large contribution to the development of the heavy industry of Germany in the 20th century by producing large amounts of coal and steel. The economy of the area rapidly developed owing to coal mining and the steel industry, thus increasing the population. After World War II, the importance of the Ruhr industrial area for West Germany increased because of the loss of industrial area in East Germany. The reconstruction of industry in the Ruhr progressed rapidly after World War II with the support of the Marshall Plan, and more than 50% of residents of the Emscher area were engaged in industrial production in 1970. Figure 2-3(c) presents the landscape around the Emscher River in 1960. With the economic reconstruction, the amount of wastewater increased and a large wastewater treatment facility was built in 1977 (Figure 2- 3(d)).

In consequence, both Kitakyushu and the Ruhr were among the most important motive powers of Japanese and German industrialization in the 20th century. Although these two regions suffered serious damage during World War II, reconstruction proceeded with a high priority under the conditions of the postwar period. Evidence of the social

(a)1899



(b)1906



(c)1960



(d)1977



(e)1996



(f)2007



Figure 2-3 Transition of Emscher River from 1899 to 2007
(quoted from <http://www.eglv.de/emschergenossenschaft/emscher-umbau/emscher/zeitreise/>)

atmosphere of these two industrial areas at that time is the following song^{iv}, the Yahata city anthem:

The flame burns high billows, and the smoke covers the sky. The grand sight of the world, our iron factory. Yahata, Yahata, our home town. The progress of the city is our duty.

Figure 2-4 presents the landscape of Kitakyushu in the middle of the 20th century. A great amount of emission of smoke is shown in figure 2-4, and the city anthem reflects the city's pride in it as a symbol of the great development of heavy industry in their town. Similarly, Nagamatsu (2006) noted that residents of the Emscher area accepted air pollution and water contamination in exchange for high wages; moreover, environmental destruction (figure 2-5) was admired as a sacrifice for national development.

2.2.3 Period 3: Decline of heavy industry and economic recession

However, the heavy industries in these regions gradually declined in the late 20th century. The main reasons of the decline are as follows: a shift of the energy resource from coal to petroleum; decrease of the steel industry's coal consumption through energy-saving technologies; and change of industrial structure from secondary to tertiary industry. With the decline in heavy industry, an economic recession started, increasing the unemployment rate and decreasing the population (Taketoshi, 2002; Nagamatsu, 2006). Furthermore, the environmental destruction from the previous time period caused serious public disruption. Figure 2-6(a) shows the water contamination of Doukaiwan Bay in the 1960s due to the wastewater from factories. Doukaiwan Bay was known as the Sea of Death reflecting the situation that no life could survive in the bay at that time.



Figure 2-4 Smoke emission from factories in Kitakyushu in the 1960s
(quoted from http://www.city.kitakyushu.lg.jp/kankyou/file_0269.html)



Figure 2-5 Landscape of the Emscher area in the industrial period
(quoted from <http://www.art-society.com/report>)



Figure 2-6 Water pollution in Doukaiwan Bay (a)in 1960 (b)in 1980
(quoted from http://www.city.kitakyushu.lg.jp/kankyou/file_0269.html)

Similarly, the Emscher area suffered from environmental problems in the late 20th century; the most serious problem was pollution of the Emscher River. Although wastewater treatment facilities were operated (figure 2-3(d)), the water pollution became worse. U. Raasch, a technical officer of the water management organization of Emscher at that time, described the situation as it existed then: “The Emscher is straightened and lined with impervious concrete beds to convey wastewater from cities as well as industrial areas along the river’s course, resulting in the river becoming environmentally dead” (Salian and Anton, 2011).

The quality of life of the Kitakyushu and Emscher areas was degraded by economic recession and environmental problems. In other words, the Kitakyushu and Emscher regions were taken advantage of as if they were colonies exporting resources for the development of nations but, ironically, becoming forlorn places as the development proceeded.

2.2.4 Period 4: Area revitalization

In these severe situations, the Kitakyushu and Emscher areas both started a wide variety of area revitalization projects to improve living and economic conditions. One of the notable points is that both regions placed importance on environment for revitalization, especially in the projects carried out in the late 20th century. Projects in that period in these two areas have been highly original and effective. As a result, Kitakyushu and the Emscher area are now known as the most successful models of environmentally friendly areas. The specific contents of the revitalization projects are described in the following paragraphs.

Nomura (2011) pointed out that the merger of five cities in 1963 paved the way for

solving environmental problems. Before the merger, it was difficult to carry out practical environmental policy owing to the economic situation of Kitakyushu, which was strongly reliant on heavy industry (and the social atmosphere described above).

Under this situation, a public health unit was established in the Kitakyushu city office along with the merger in 1963. The unit had only four members at that time, and their competence was limited. However, the members and functions of the unit increased in later years, and the unit was raised to its present status (table 2-1). Much effort went into improving the environmental situation in Kitakyushu with the expansion of the department; for example, the staff started onsite inspections for monitoring the contaminant discharge status of heavy-industry factories. Furthermore, they developed local pollutant regulations that were stricter than the national rules^v. In addition, they concluded antipollution agreements with private companies and arranged financial support system for them to improve pollution prevention techniques in factories. Owing to these challenges, the public environmental disruptions in Kitakyushu region were resolved almost completely before 1980 (figure 2-6(b)).

After the fight against pollution, the social movement of Kitakyushu entered a new stage for further improvement of the living environment and creation of a sustainable development policy. The city office launched a 15-year urban design plan named Kitakyushu Renaissance Conception in 1988. A unique project of this plan was the

Table 2-1 Growth of the environmental department of Kitakyushu city
(data from Taketoshi 2002)

Year	1963	1965	1970	1971	1975
Member	4	8	22	47	79
Status	Unit	Division	Division	Bureau	Bureau

establishment of Eco-Town, which was a special district for fundamental research, demonstration experiments, and environmental businesses. To this day, fundamental research and demonstrations have been conducted through the cooperation of universities and private companies. Environmental businesses are operated by pioneering companies, and regular recycling of metal, plastic, and precision equipment is now an ongoing activity. Fifty-one demonstration experiments were finished, and about 1,300 new jobs were created in these new businesses by 2009. With the increasing importance of environmental technology, there is now a focus on overseas expansion of environmental businesses, and cooperative enterprises with foreign companies have been started. Because of achievements like these, Kitakyushu is considered one of the most advanced cases of an environmentally friendly society in Japan.

As for the Emscher area, it is frequently pointed out that the Internationale Bauausstellung (IBA) Emscher Park Project^{vi} was an important turning point in revitalization of that area (e.g. Kasugai 2002). The target area of the IBA Emscher Park Project extended through multiple political districts, and 17 counties and independent cities were included. There was no appropriate organization to move forward with the project, so a temporary company was set up for ten years (1989 to 1999) to manage the project. The company was funded by the Nordrhein-Westfalen state government, and 33 members, including two city officials, belonged to it. At the beginning of the IBA project, the company presented five major themes for area revitalization: the Emscher Park, the reconstruction of the Emscher water system, working in the park^{viii}, new uses for old industrial buildings, and new housing projects. Under these main concepts, the company offered area revitalization projects, not only for private companies but also for public organizations and individuals. The company evaluated the suitability of each

project in light of the five fundamental concepts, and gave financial and informational support to carry out a project if it was accepted. During the ten years, 123 projects were conducted and more than 15 billion euros was invested, improving the landscape, economic conditions, and infrastructure. One of the most representative projects of IBA Emscher Park was the reconstruction of the Emscher River. With the development of heavy industry during the 20th century, the river was drastically modified artificially and used as a huge, efficient wastewater system (figure 2-3(c) and figure 2-3(d)). However, after the recession of heavy industry, such a huge wastewater treatment system was not needed any more.

Under this circumstance, residents and environmental organizations in the Emscher region started a grass-roots social movement demanding improvement of the environmental condition of the Emscher River. Following this action, the water management organization for the Emscher area (the Emschergenossenschaft) started a massive project using the system of the IBA program. Although a part of work is still pending in 2016, achievement is observable in the Emscher River and its tributaries (figure 2-3(e) and figure 2-3(f)).

The revival of the original nature of the Emscher River provided a good image for people, and furthermore, the improvement of the landscape and the living and working environment attracted people from other regions. Taking advantage of this positive image, subnational governments in the Emscher area have been giving emphasis to development of environmental businesses like green tourism, health services, and low energy housing. As a result of these challenges, the Emscher area has broken from the past problem-ridden situation, changed its industrial structure, and improved the employment rate (table 2-2).

2.3 Three success factors for the achievement of an environmentally friendly society

In the last century, the Kitakyushu and Emscher areas passed through four time periods as described above. Although these two regions were in environmental predicaments due to industrial recession, they are now considered the most successful cases of environmentally friendly societies. In this section, the author discusses the reasons why these two areas accomplished their remarkable achievements.

2.3.1 Management organization

The first point of success was the existence of unified management organizations, i.e., the city office of Kitakyushu and the IBA Emscher Park Company. Past studies pointed out that the persistent negotiations with, and support for, private companies by the city offices made a large contribution to establishment of sustainable societies in Kitakyushu. As mentioned above, the antipollution policies in the Kitakyushu were put into effect after Kitakyushu city was created in 1963.

One of the remarkable points of the challenge of the Kitakyushu city office was its specific approach, called the "Kitakyushu method." The Kitakyushu city officials designed their unique regulations to reduce environmental burdens; however, they did not force the regulations on private companies, but instead took counsel with workers,

Table2-2 Proportion of jobs in 1970 and 2006
(data from Seltmann 2006)

	Industrial production (secondary industry)	Services (tertiary industry)
1970	58%	28%
2006	40%	70%

residents, and intellectuals to make their regulations effective. Through conferencing, the city office secured antipollution agreements with private companies and established a funding system for improving environmental performance of factories. Although a concept of cooperative social responsibility for contamination was not common at that time, private companies took prompt actions to follow the environmental agreement because of the cooperative attitude of Kitakyushu city and its good management. This desirable relation between the city office and private companies continued after 1980 and contributed to the success of projects in later days.

Similarly, the IBA Emscher Park Company played a highly important role in the area revitalization in the Emscher area. It is notable that, unlike the Kitakyushu case, the IBA Emscher Park Company did not have political power. Despite this difficulty, and the fact that the target area contained 17 different local governments and a population about twice that of Kitakyushu (about 2 million versus 1.1 million), the company achieved great success during the first ten years and established the regional identity of the Emscher area in later days.

As mentioned above, the main business of the company was evaluating the projects that were collected from the public, providing the information and financial support, and coordinating the entire program. The company held international competitions for urban design and building programs, and consulted with specialists in open conferences and workshops if an unexpected problem occurred. This project management procedure was one of the most important roles of the IBA Emscher Park Company, and it contributed to the steady implementation of sustainable development. Unlike the Kitakyushu case, this system collected ideas from the public; thus, private companies and other actors had no obligation to participate in the program. However, many projects were suggested, not only

from private companies, but also from public organizations and individuals. Regarding reasons why people were eager to suggest projects, Kasugai (2002) pointed out the importance of public relation. The IBA Emscher Park Company publicized adopted projects using their network in the Emscher area. This support contributed strongly to improving the image of a presenter of a project; moreover, it raised social credibility. Thus, improvement of image was an important benefit for a presenter, especially for a private company. This gave them great motivation to join the IBA program although it was not their duty.

Compared to the approach of the Kitakyushu city office, the IBA Emscher Park Company used different methods to achieve area revitalization. However, the facts presented above indicate that the advanced management ability of the unified organization was an important factor to establish an environmentally friendly society.

2.3.2 Symbol of revitalization

The second key factor in achievement of an environmentally friendly society was public consciousness for a symbol of good environment. Both the Kitakyushu region and the Emscher area suffered from severe water contamination in the middle of the last century (figure 2-3 and figure 2-6). However, the water problem was solved in these two areas in the latter part of the last century, and this recovery of the water system raised the expectation of an environmentally friendly society in the future.

The pollution of Doukaiwan Bay was caused by the wastewater from the factories, and contamination peaked in the 1960s. No life could survive in the bay^{viii}, so Doukaiwan Bay was called the Sea of Death or the Champion of Pollution. Action by a local women's association was started against this environmental pollution, and this was a trigger to



Figure 2-7 Research of public disruptions by women's association
 (quoted from http://www.city.kitakyushu.lg.jp/kankyuu/file_0269.html)

solve the environmental problem in Kitakyushu. The women's association widely publicized the seriousness of environmental disruption through unique methods like homemade movies, fieldwork at factories, and scientific research (figure 2-7). Residents had endured the pollution before the movement, but the association's effort changed the public sense about the environment and helped smooth promotion of the antipollution measures by Kitakyushu city. The most important achievement of the environmental department was the cleaning operation of Doukaiwan Bay. The dredging operation was planned in 1966, based on the national laws for preserving water quality and regulation of wastewater. The operation was carried out in the 1970s in cooperation with private companies, drastically reducing the contamination of Doukaiwan Bay (figure 2-6(b)).

The environment was improved after the Doukaiwan Bay project (e.g., Shikata 1991). The Kitakyushu city authority maintained an uncompromising attitude to pollution by private companies and monitored the environmental burden from industrial activities. This strict position of the city office was reported by the mass media, strongly increasing

the public awareness. Additionally, the cooperative framework established during cleaning operations between city office and private companies led to the ongoing policies for growing environmental industries in later years.

In the Emscher area, the destruction of the Emscher River was caused by construction work from the early 20th century, and the river's ecological system was completely dead by the middle of that century. With the recession of heavy industry, the Emscher River was considered the negative legacy of declined region. A turning point for the river was IBA Emscher Park Project, and the quality of the water and the surrounding environment was recovered. Salian and Anton (2011) gave a detailed explanation of the revitalization process of the Emscher River. They mentioned that local demand and political pressure from residents were important motivations for promoting the recovery project. As a result, the IBA Emscher Park Company put major emphasis on the reconstruction of the water system. From the perspective of area regeneration, the reconstruction of the river made a large contribution toward changing the public awareness of residents for their home town. Salian and Anton (2011) and LaBelle (2001) described that the living environment in Emscher area was extremely bad before the IBA project; however, with the recovery of the river, the citizens acquired confidence in their town. In addition, they indicated that this transition of public sense is the most important outcome of the project. The social consensus for evolving an environmentally friendly society is raised, and this helps the smooth promotion of later eco projects in the Emscher area. In the IBA Emscher Park Project, a number of work were carried out for improving the landscape. At first, many people questioned whether a large amount of money should be spent for this rather than housing and other social needs; however, the achievement of the Emscher River rehabilitation persuaded them, and following projects were conducted successfully. As a

Table 2-3 Water pollution and environmental policies in Kitakyushu and Emscher area

	Kitakyushu	Emscher
Motivation	Pressure from women's association	Pressure by nongovernmental organizations and citizens
Project	Cleanup operation of Doukaiwan Bay	Renaturation of Emscher River
Ripple effect	Rise of public awareness Development of environmental technology	Change in the sense of citizens Assurance of budget for following projects

result, the landscape of the Emscher area is now drastically improved, and not only residents but also visitors enjoy ecological tours and other outdoor leisure activities.

In summary, the historical contexts of Doukaiwan Bay and the Emscher River were similar (table 2-3), and both are considered symbols of area revitalization, inducing a social consensus that has led to later challenges to improve the environment. In consequence, the regional identity of the Kitakyushu and Emscher areas in the present day is attributable to the symbolism developed in the late 20th century.

2.3.3 Legacy of heavy industry

The third factor of success in the Kitakyushu region and Emscher area was effective use of the legacy of the past. The environmental businesses of Kitakyushu, like the recycling business, developed in relation to heavy industry; on the other hand, the main environmental businesses in the Emscher area, like green tourism, were not directly linked to heavy industry. Although these two areas encouraged different environmental industries, both used local resources that were made in their "golden age" of heavy industry.

One of the most important achievements of Kitakyushu is Eco-Town. There are 26 Eco-Towns in Japan, and the one in Kitakyushu is known as the most advanced case. It has been deemed that the connection between environmental industries and local resources contributed to the growth of Kitakyushu's Eco-Town. Akimoto (1994) presented six requirements for formation of a recycling business: a large amount of waste material, usefulness of the waste material, homogeneity of waste, a system for collecting waste, an established technology, and demand for recycled materials. In accordance with Akimoto (1994), it was beneficial for a recycling business to locate near an industrial area because of a large amount of homogeneous waste materials from factories. Furthermore, there was a relatively large demand for recycled goods in the Kitakyushu area, and thus Eco-Town in Kitakyushu had a large advantage in the recycling business.

In addition to these factors, it was considered that both hard and soft regional resources were used well in Kitakyushu. In tangible aspect, the traffic infrastructure designed for heavy industry promoted smooth transportation of materials and products for a recycling business. In intangible aspect, the Kitakyushu city office provided a hospitable support system for new environmental businesses. The notable point is that the city office promoted environmental industries and simplified the admission procedure to start a new business. Furthermore, the city office dispatched support staff to a company that intended to start a new business, and this staff had all the responsibility for negotiations between the city office and the company. These systems reduced entry barriers and contributed to the development of Eco-Town. This committed attitude and useful system were associated with the experience of overcoming public environmental disruption through the cooperation with private companies. Thus, it is considered that the network and relation of mutual trust relations between the city and the companies, as established

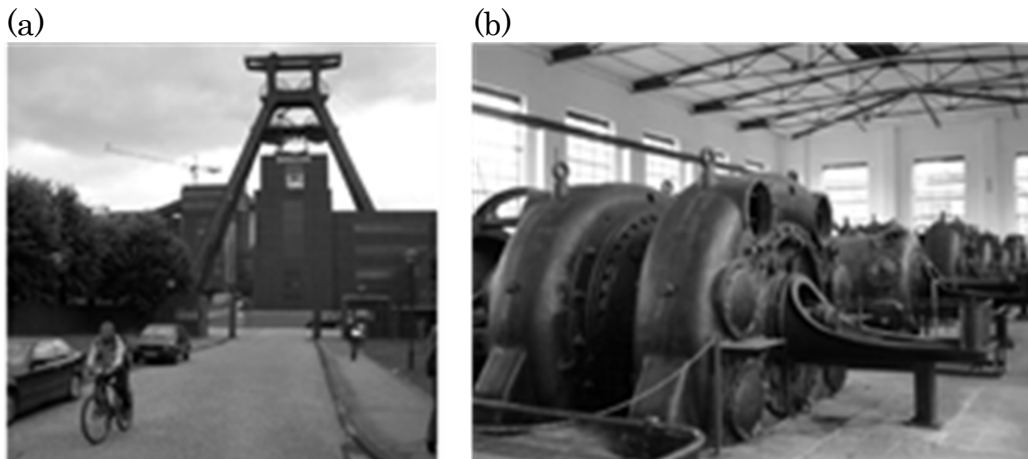


Figure 2-8 (a) Heritage of the Zollverein Coal Mine Industrial Complex
(b) Coal factory in Dortmund (quoted from Motooka and Tanaka, 2006)

several decades ago, had a large influence on the current situation of Kitakyushu.

On the other hand, the Emscher area used the legacy of the past in a different way from Kitakyushu. One of the major concepts of the IBA Emscher Park Project was the use of old industrial buildings, and a number of factories and industrial bases were reused as regional resources for sightseeing. A successful case was the Zollverein Coal Mine Industrial Complex in Essen, which was considered the most beautiful coal mine in the world and was registered as a world heritage site in 2002. The complex was built in the middle of the 19th century and halted operations in 1986, three years before the IBA Emscher Park Project began. The coal mine remained as the original feature, representing the region's history and identity as an industrial region (figure 2-8(a)) Similar to this coal mine, a number of renovation projects were conducted on closed-down factories and industrial bases. They were repurposed to such uses as an art museum, cafeteria, green leisure, and education facility for local history (e.g., the coal factory in Dortmund, figure 2-8(b)). These reused buildings of heavy industry helped to rediscover regional culture and became the pride of residents. In addition, these repurposing projects improved the

landscape of the Emscher area, increasing the number of visitors seeking green tourism.

Compared to the case of Kitakyushu, the main feature of the use of the past legacies in the Emscher area was to introduce new businesses like sightseeing and green tourism. A number of remaining buildings were renovated and had new functions, different from what they had in the past. In other words, the Escher case indicates that old tangible legacies can be used by adding new intangible values.

2.4 Application to developing countries

So far, the historical background of the establishment of an environmentally friendly society in Kitakyushu and the Emscher area was reviewed (chapter 2), and the reasons for their success were revealed (chapter 3, table2-4).

For the last several decades, industrial areas in developing countries have been growing rapidly owing to large investment from developed countries. As Akamatsu (1962) mentioned, developing countries try to catch up with developed countries, but the competition among developing countries is severe in the global market; thus, it is difficult to hold onto a competitive advantage. Therefore, a new industrial area in developing countries may possibly be confronted with an economic recession similar to those suffered by Kitakyushu and the Emscher area in the middle of the last century. For this expected problem, the experience of Kitakyushu and the Emscher area seems to provide many useful suggestions for regional-level adaptation. For this reason, in this chapter the author discusses whether the knowledge presented above is applicable to developing countries.

The environment authority of the Kitakyushu city office gradually expanded over 50 years, accumulating experience in pollution management, and that experience made a

large contribution in establishing an environmentally friendly society. Similarly, the IBA Emscher Park Company took advantage of the experience and methods developed in past IBA projects. The environmental legal system and political organizations of developing countries have recently reached high standards. However, as Hiraoka (2005) pointed out, industrialization proceeds extremely quickly in developing countries through large, rapid investment from developed countries. Thus, human resources in developing countries do not have time to acquire practical skills and methodologies of environmental governance. For this reason, environmental contamination continues in the present day even if a high-standard social system are introduced. Moreover, according to the Kitakyushu and Emscher cases, a lack of human resources with enough experience in environmental management may delay area revitalization after the decline of heavy industry. Hence, the author can conclude that the know-how and practical skills of Kitakyushu and the Emscher area should be shared as soon as possible to train local human resources. Furthermore, it is desirable for local people to acquire an ability to design future plans for their towns by themselves.

Regarding symbols of area revitalization, it is expected that the importance of a symbol is greater in the present day than in the past. The reason is associated with the current remarkable development of information technology. The revivals of Doukaiwan Bay and the Emscher River were widely publicized by mass media in Kitakyushu and by the IBA Emscher Park Company. As a result, these two water systems played a very important role in building social consensus for clean environment and inducing follow-on projects of an environmentally friendly society. According to the review by Taguchi and Shida (2010), recent research have pointed out the importance of sharing information to achieve development with health environment (e.g., Dasgupta et al. 2002). Well-

Table2-4 Key factors to construct sustainable society in the two regions

	Key essence and measurements		
	Leading organization	Symbol of revitalization	Use of past legacies
Kitakyushu	<ul style="list-style-type: none"> Environmental agreements and projects with private companies ·Long-term design to establish sustainable society 	<ul style="list-style-type: none"> ·Cleaning project of Doukaiwan Bay ·Public awareness of the importance of environment 	<ul style="list-style-type: none"> ·Regional characteristic as a heavy industrial area ·Mutual understanding between city office and private companies
Emscher	<ul style="list-style-type: none"> ·A five-measure framework for sustainable society ·Management of a variety of projects sought for the public 	<ul style="list-style-type: none"> ·A series of projects for Emscher river renaturation ·Encouragement of residents' consciousness of their town 	<ul style="list-style-type: none"> • Renovation of relics of heavy industry facilities • Creation of new types of environmental businesses

developed information technologies enable not only large organizations, but also individuals, to spread their opinions, and thus it is expected that a symbol of clean environment will greatly assist to promote the environmental movement.

Regarding the use of past legacy, it is difficult to predict how industrial areas in developing countries can use legacy in the future because they are growing in the present day; thus, the legacy for the future is being created now. However, what is important is that a variety of ways exist to use legacy in regard to both tangible and intangible values. Therefore, it is required that people suggest unique and free ideas for using their regional resources for area revitalization.

2.5 Conclusion

In this study, the author examined cases of two pioneers of environmentally friendly societies, Kitakyushu and the Emscher area. Through this comparison, the author discussed why and how these two regions became the most advanced models of a sustainable society.

First, the historical background of these two regions over the last 100 years was analyzed, and it was revealed that they had very similar historical contexts. Moreover, their histories were divided into four time periods: dawn of heavy industry; golden age and environmental problems; decline of heavy industry and economic recession; and area revitalization. The regional identities of these two regions were established with development of heavy industry in the early 20th century, and they achieved remarkable economic development in the middle of the last century. Although they suffered from economic recession and poor living standards from the 1960s to the 1970s, they achieved area revitalization and now are well known as pioneers of environmental society.

In the third chapter, the procedures of area revitalization in the late 20th century were analyzed in detail. Three key factors in the success of area revitalization—management organization, symbol of clean environment, and legacy of the past—were presented. In both cases, a unified organization promoted area revitalization with strong leadership. The leadership conducted many projects, building consensus among residents through a symbol of clean environment, and this attitude induced follow-on environmental projects. Effective use of the heavy industry legacy of the past reinforced regional identity and raised the pride of the residents.

Finally, the author discussed whether the teachings extracted from the experiences of Kitakyushu and the Emscher area are applicable to developing countries. In the present day, developing countries have high-level legal systems and organization, but lack people with enough practical knowledge and skill in environmental governance. Thus, personnel exchange is greatly needed to raise the abilities of local people. In regard to symbols of area revitalization, it is expected that symbols and models will play an extremely important role for promoting revitalization projects owing to the current high standard of information technologies. It is difficult to presume how the legacy of the past will be used in the future, but there are a variety of ways to use it, so unique and free ideas are desirable.

References

- Akamatsu, K. (1962) A Historical Pattern of Economic Growth in Developing Countries, *The Developing Economies*, vol. 1, pp. 1-23
- Akimoto, K. (1994) Construction of regional system of resource circulation (in Japanese), *Sangyou Ricchi*, vol. 11, pp. 11-22.
- Dasgupta, S., Laplante, B., Hua, W., and Wheeler, D. (2002) Confronting the Environmental Kuznets Curve, *The Journal of Economic Perspectives*, vol. 16, no. 1, pp. 147-68
- Hiraoka, Y. (2005) The "Disadvantage of Backwardness" in Environmental Problems in Asia and Japanese Experience (in Japanese), *Studies in Humanities*, vol. 56, pp. 23-43
- Kasuga, S. (1956) The Regional Construction of Industries—With Special Reference to the Industrial Region of North Kyushu (in Japanese), *Japanese Journal of Human Geography*, vol. 8, pp. 20-33.
- Kasugai, M. (2002) *Town planning of Germany*, 4th edition (in Japanese), Gakugei-Shuppan Press, Kyoto
- Kishimoto, C. (2011) Establishment of a sustainable society in Kitakyushu in post war era, *East Asian Economic Perspectives*, vol.22, pp. 23-36
- LaBelle, J. M. (2011) Emscher Park, Germany—Expanding the Definition of a “Park,” *The George Wright Society Forum*, vol. 18, no. 3, Michigan, USA
- Matsunaga, H. (2004) Agglomeration of the heavy and chemical industries and the generation of the environmental industries (in Japanese), *Association of Economic Geographers*, vol. 50, pp. 325-340
- Ministry of Economy Trade and Industry of Japan (2006) Report of Eco Town project/Environmental industries in progress.
- Motooka, T., and Tanaka, Y. (2006) Area revitalization of metropolitan area of Ruhr and Rhine, *Space, Society and Geographical Thought*, vol. 10, pp. 57-83

- Mu, Q., and Zhang, S. (2013) An evaluation of the economic loss due to the heavy haze during January 2013 in China. *China Environmental Science*, vol. 33, pp. 2087-2095
- Nagamatsu, S. (2006) *Area rebirth in IBA Emscher park*, 1st edition, Suiyou-Sha press, Tokyo.
- Nomura, M. (2002) Historical Survey of Environmental Policy in Kitakyushu City Up to This Day, *KIU Journal of Economics and Business Studies*, vol. 17, pp. 13-22
- United Nations Population Division. *World Population Prospects, the 2015 Revision*, http://esa.un.org/wpp/documentation/pdf/WPP2010_Volume-I_Comprehensive-Tables.pdf (accessed June 11, 2016).
- Salian, P., and Anton, B. (2011) *The Emscher Region: The Opportunities of Economic Transition for Leapfrogging Urban Water Management*. Freiburg: ICLEI European Secretariat GmbH
- Seki, M. (2009) *Eco town as a local brand*. Shinhyouron Press, Tokyo
- Seltmann, G. (2007) Renaissance of an industrial region: "Internationale Bauausstellung Emscher Park"—achievements and future model for others, URL: <http://www.riss.osaka-u.ac.jp/jp/events/point/P.Seltmann.pdf>
- Shikata, H. (1991) *A town changes smog to star, challenge of Kitakyushu city* (in Japanese), Kodansha Press, Tokyo.
- Shimizu, N. (2010) The Establishment of the State-Owned Yahata Steel Works: The Integrated Steel Works That Promoted Japan's Industrialization When the Country Entered the Modern Industrial World as a Latecomer, *KIU Journal of Economics and Business Studies*, vol. 17, pp. 1-68
- Sun, Y. (2005) The transformation of the industrial structure and the environmental burden, *The Review of Welfare Society*, vol.4-5, pp. 69-96
- Taguchi, H., and Shida, T. (2010) Environment Pollution Control: Advantage or Disadvantage for Latecomer's Economies in East Asia, *PRI Discussion Paper Series*,

10A-02

Takano, H. (1959) The types and definition of “urbanization.” (in Japanese),
Geographical Review of Japan, vol. 32, pp. 629-642

Taketoshi, K. (2002) Anti-pollution measures and their characteristics in Kitakyushu city
(in Japanese), St. Andrew's University Economic and Business Review, vol. 43, pp. 299-
321

Chapter II picked up Kitakyushu and Emscher areas as pioneering model cases of sustainable societies, and investigated the process of conversion of social form from that emphasizes economic development without caring environmental protection to that accomplishes development under the balance of economy and ecology under the view point of comparative sociology. In the following three chapters (chapter III, IV, and V), a series of studies from a view point of wind engineering were conducted to comprehend urban environmental problems as a physicochemical phenomenon.

As it explained in Chapter I, chapter III conducts technical discussion about the measurement accuracy of PIV experiments for unsteady turbulent flow fields around scaled urban building models. Nowadays, although PIV is employed in wind tunnel experiments on complicated and unsteady turbulent flow fields owing to the useful features such as multi point measurement with high spatial resolution and contactless measurement, obtaining highly accurate data is still difficult even if high standard experimental devices are employed. In chapter III, first I explain the physical theory of PIV measurement referring the past and current usage situations of PIV technique, and then identify the problem about measurement accuracy which is called peak locking and propose a simple countermeasure for the problem.

Chapter III

Study on measurement accuracy of PIV in a large size wind tunnel

3.1 Introduction

PIV is the technique comprised of flow visualization and image processing. Tiny particles scattered in a flow field are illuminated by a thin laser sheet, which is created by an optical unit and a laser generator, and photographs of these particles are recorded using a high speed camera. A wind velocity is estimated based on the moving distance of a particle group between two images with a short time interval (generally, $10^{-3} \sim 10^{-6}$ s in laboratory experiments). This fundamental framework of PIV was established by Adrian (1984).

The features of PIV are multi-point measurement with high spatial resolution, non-contact measurement. In addition, it is possible to obtain the data with a high frequency. Such features are useful to investigate complicated structures of unsteady three dimensional turbulent flow. In particular, contactless measurement is beneficial to capture small structures nearby a bluff body such as flow separation and re-attachment.

Based upon these advantages, PIV has attracted much attention from researchers of various fields; practicability and measurement accuracy of PIV have been significantly improved for several decades owing to the development of experimental equipment and analysis algorithms. For example, digital cameras become widely used since 1990's instead of film cameras (e.g. Willert and Gharib 1991; Keane and Adrian 1992), obtaining more than several hundred images in a single test, which are enough to obtain turbulent statistics. Advanced algorithms for image processing have improved spatial and temporal

resolutions (e.g. Hart 1999; Westerweel 2000; Chen and Katz 2005; Hain and Kahler 2007). For example, Chen and Katz (2005) developed a hybrid algorithm of a cross correlation method and a particle tracking method, increasing spatial resolution of image processing to several times of the former methods. Adrian (2005) provides comprehensive review of such development of PIV techniques, and describes a standard PIV system which consists of a double-pulsed Nd:YAG laser, a high speed digital camera, and a planar light sheet. Owing to these efforts, PIV is widely applied in the present days in a variety of research areas, including wind engineering and urban atmospheric boundary layer science as listed in Table 3-1.

Since the relation between urban geometry and flow field structures has been one of important research subjects in urban atmospheric boundary layer science, PIV experiments shown in Table 3-1 mainly focus on the turbulent flow field near the urban-like roughness. Simoens et al.(2007), Uehara et al. (2007), Reynolds and Castro (2008), Takimoto et al. (2008), Annalisa et al. (2014) and Sato et al. (2016) presented temporally averaged flow fields around a various types of block arrays. For example, Simoens et al. (2007) measured flow fields around 2D street canyons with different canyon aspect ratio (the ratio of the street width to the canyon roof height), and showed the transition of the temporally averaged flow fields within the street canyons. Uehara et al. (2007) measured flow fields in an arterial road parallel to the streamwise direction with four types of roughness configurations: a uniform array of low-rise buildings, an array of high-rise buildings in windward side and low-rise buildings in leeward side, an array of low-rise buildings in windward side and high-rise buildings in leeward side, and a zigzag array

Table 3-1 List of past PIV experiments conducted in wind engineering and urban atmospheric boundary layer science

Authors	Facilities	Scaled models	Research targets
Park and Lee (2000)	Water channel	3D finite cylinder	Visualization and statistical analysis of 3D wake structures around a free end of a cylinder
Yoshikawa et al. (2003)	Wind tunnel	3D finite cylinder 3D finite rectangular	Relation of wind load (wall pressure) and unsteady wake structures around a tall building model
Liu et al. (2003)	Water channel	Single 2D canyon	Instantaneous flow field structures under different thermal conditions (neutral and unstable)
Caton et al. (2003)	Water channel	Single 2D cavity	Flow field structures and scalar emission process within and over a 2D cavity
Takimoto et al. (2006)	Field experiment	Square array of cubes	Turbulent statistics and momentum transportation within and over a 3D urban canyon
Huq et al. (2007)	Water channel	Square array of cubes and slender blocks	Temporally averaged flow fields and shear layers in two type urban canopy models
Kikitsu et al.(2007)	Wind tunnel	3D finite rectangular	Interaction mechanism between a vibrating three dimensional square rectangular and turbulent flow fields
Pokrajac et al (2007)	Water channel	2D street canyon	Spatial distributions of turbulent organized structures and form induced momentum transport over a 2D street canyon
Simoens et al. (2007)	Wind tunnel	Single 2D canyon	Spatial distributions of turbulent statistics over 2D street canyons of different canyon aspect ratio
Uehara et al. (2007)	Wind tunnel	Square array of blocks with different height	Temporally averaged flow fields around urban models with height variability
Reynolds and Castro (2008)	Wind tunnel	Staggered array of cubes	Turbulent statistics, momentum transport, and turbulent structures near an urban building model

Takimoto et al. (2009)	Field experiment Wind tunnel	Square array of cubes	An effect of wind direction on turbulent flow fields within an urban canopy
Salizzoni et al. (2011)	Wind tunnel	2D cavity	Momentum transport mechanism between the region above and inside a 2D cavity and a mean velocity scale
Takimoto et al. (2011)	Field experiment Wind tunnel	Square array of cubes	Instantaneous up-flow and down-flow motions observed around an urban canopy
Kellnerova et al. (2012)	Wind tunnel	2D street canyon	Dominant coherent structures around 2D street canyons with flat and triangle roofs
Takimoto et al. (2012)	Wind tunnel	Smooth surface 2D street canyon Square array of cubes	Horizontal scale of turbulent organized structures above different shape urban models
Katsuki et al. (2012)	Wind tunnel	Scaled model of real urban area	Recirculation eddy structures and momentum transport within a complicated urban geometrical model
Sato et al. (2013)	Wind tunnel	Staggered array of slender blocks	Typical instantaneous flow motions around a high rise urban building model
Annalisa et al. (2014)	Water channel	2D street canyon	An effect of canyon aspect ratio on a boundary layer structure and kinetic energy dissipation within a canyon
Sharon et al. (2014)	Water channel	Random array of thin plates	Drag force, Reynolds stress, and dispersive stress within undeveloped and developed boundary layers
Arinami (2015)	Wind tunnel	Single building model with opening	Simultaneous measurement of instantaneous flow fields around and inside a building model
Yamada et al. (2015)	Wind tunnel	Building model with penthouse	A mean scale and spectrum of turbulent flow fields within a flow separation region on a building roof
Sato et al. (2016)	Wind tunnel	2D street canyon	An effect of substructures on turbulent flow fields around a 2D street canyon

of high-rise and low-rise buildings. Flow fields in both vertical and horizontal cross sections were measured in their experiment, and they proposed the three dimensional structures of temporally averaged flow fields.

Moreover, investigations on unsteady turbulent coherent structures have greatly progressed through PIV measurements. Traditional flow visualization experiments using ink and hydrogen bubbles (e.g. Kline et al. 1967, Grass 1971) reveals qualitative features of turbulent coherent structures in a broad perspective, while current PIV can provide quantitative data of instantaneous turbulent flow fields with high spatial and time resolutions. For example, Reynolds and Castro (2008) conducted a PIV experiment on turbulent flow fields around a cubic staggered array with plan area index $\lambda_p = 25\%$ (the ratio of the plan area occupied by obstacles to the total floor area), and they demonstrated characteristic low-speed ascent flow (ejection) and high-speed descent flow (sweep) which intermittently arise around a canyon. In addition, they pointed out that these typical flow motions cause large momentum transfer between the region inside and outside of a canyon. Similar results are observed for a cubic square array with $\lambda_p = 25\%$ in both a wind tunnel experiment and an outdoor experiment (Takimoto et al. 2011). Kellnovera et al. (2012) applied time resolved PIV (TR-PIV, which is a PIV with high temporal resolution), on a turbulent flow fields around 2D street canyons with flat and triangle shape roofs, and extracted dominant flow modes based on turbulent kinetic energy.

These studies have greatly contributed to deepen our understanding on turbulent flow natures around urban-type roughness. In the present days, sophisticated data utilizing the PIV method are still highly needed for advanced research, such as tracking generation and extinction process of vortices in the vicinity of roughness, analysis on temporal and spatial variations of characteristic flow structures around roughness (e.g. flow separation

and reattachment), and examination on the interaction of turbulent flow fields with different natures (e.g. simultaneous measurement of outdoor and indoor flow). However, it is not easy to acquire high quality data enabling these advanced analysis even if high standard experimental devices are employed primarily for the following reasons: (1) accuracy of particle pattern matching might be degraded in a flow fields containing strong shear and rotation (Scarano 2005), (2) limited flexibility of designing experimental setting, such as an optical access of a wind tunnel and a device specification, might affect data quality including spatial and temporal resolutions of particle images, (3) experience and skill of an experimenter have a large influence on device operation and parameter setting though considerable difference might be caused in experimental results depending on them (Kahler et al. 2016).

Under these circumstances, well-designed workshops for benchmark tests of PIV, named as “PIV Challenge” were conducted as reported by Stanislas et al. (2003); Stanislas et al. (2005), Stanislas et al. (2008), and Kahler et al. (2016). In these workshops, several tens of PIV research teams analyzed same particle image data of several ideal and simple flow fields (e.g. a wake flow of airfoil, a jet, and a pipeline flow) by their own methods. Through the intercomparison of the velocity data estimated by all the teams, various important knowledge is provided: relation between flow field properties and data accuracy, performance of different algorithms, limitations of spatial resolution and measurable velocity range, and causes and countermeasures of typical experimental errors. Similarly, a few researchers investigated the effects of device operation and parameter setting on data accuracy of PIV measurements on airflow around urban roughness model (e.g. Scarano et al. 2005, Koutani and Kobayashi 2015). However, the number of such research is extremely limited and no comprehensive bench mark tests

have been conducted in wind engineering and urban atmospheric boundary layer science, and a collective view on measurement accuracy of PIV is not established yet.

Under these backgrounds, this chapter intends to identify difficulties in PIV measurements on turbulent flow fields around urban roughness in a large-size wind tunnel based on the comprehensive review of past research, and proposes a countermeasure to improve the measurement accuracy. Section 3-2 detects a typical experimental setting of PIV in a large-size wind tunnel based on the intercomparison of past experiments, and investigates whether the typical experimental condition has any problem or not in the light of the theory of PIV. Through the discussion in section 3-2, a problem called peak locking which is generally unavoidable in the typical experimental condition is discussed. The occurrence mechanism of peak locking and a countermeasure are subsequently discussed in section 3-3 and section 3-4, respectively. Finally, the effectiveness of the countermeasure is tested in section 3-5 using experimental data obtained by the authors. .

3.2 Experimental procedure and typical experimental condition

As Adrian (2005) described, the standard PIV system consists of a laser generator, optical lens, digital camera, tracer generator and digital computer. Figure 3-1 is the schematic configuration of the typical PIV setting employed in wind tunnel experiments and figure 3-2 is the general experimental procedure of PIV. Each value in figure 3-1 is estimated from past experiments conducted in large-size wind tunnels (table 3-2).

(a) Optical unit

A thin laser sheet is formed by cylindrical lenses or a laser line generator lens (Powell

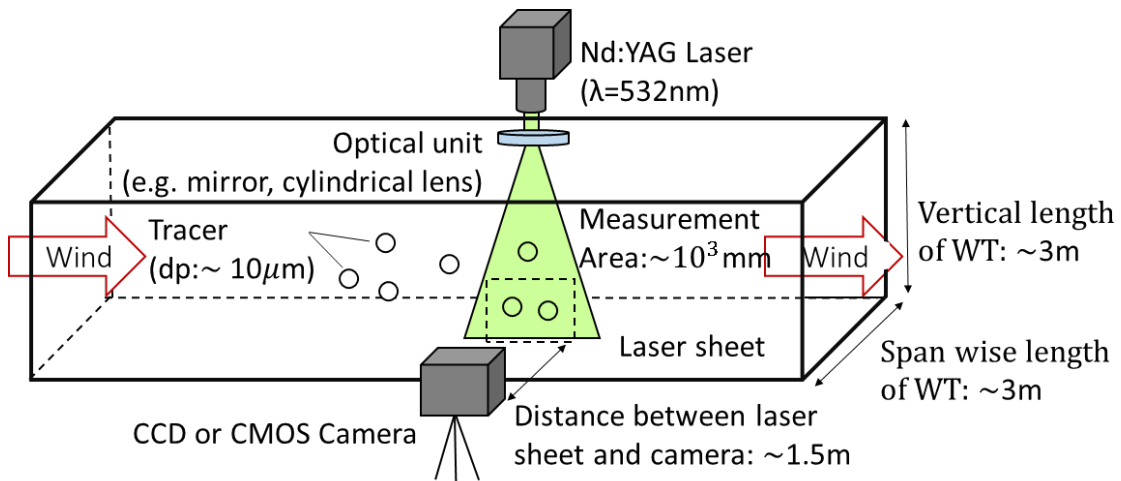


Figure 3-1 Typical experimental setting of PIV in a large size wind tunnel. Parameters are estimated from the past experiments listed in table3-2.

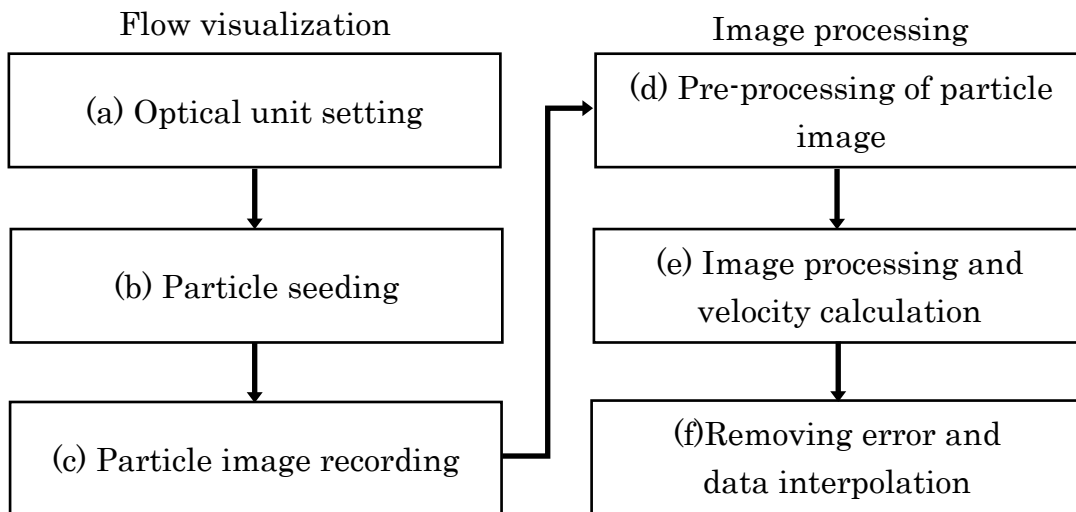


Figure 3-2 General experimental procedure of PIV

lens). The width of a laser sheet should be wide enough so as to cover a whole measurement area. In addition, the proper laser sheet thickness is necessary to keep the disappearance rate of particles between two successive images low for accurate pattern matching in process (e) (figure 3-2). Specifically, the thickness of a laser sheet should be more than four times of moving distances of particle groups in the direction perpendicular to the laser sheet (The visualization society of Japan 2002). This requirement is especially

Table 3-2 Experimental conditions of past PIV experiments in a large size boundary layer wind tunnel

Authors	Laser	Particle size [μm]	Sampling rate [Hz]	Camera type	WT cross section size (spanwise[m]×vertical[m])	Measurement area size (streamwise[m]×vertical[m])
Yoshikawa et al. (2003)	Nd:YAG, pulse	1 ~ 6	2	CCD	3.0 × 2.5	138 × 110
Kikitsu et al.(2007)	Nd:YAG, pulse	1	30, 500	CMOS	3.0 × 2.5	280 × 105
Simoens et al. (2007)	Nd:YAG, pulse	0.9	10	CCD	0.5 × 0.5	44 × 44.7
Reynolds and Castro (2008)	Nd:YAG, pulse	2 ~ 4	1~2	CCD	0.9 × 0.6	50 × 50
Takimoto et al. (2009)	Nd:YAG, pulse	-	4	CCD	1.0 × 1.0	288 × 219
Salizzoni et al. (2011)	Nd:YAG, Pulse	-	4	-	1.0 × 0.7	120 × 120
Kellnerova et al. (2012)	Nd:YAG, CW	-	500	-	0.25 × 0.25	About 150 × 150
Katsuki et al. (2012)	Nd:YAG, pulse	-	15	CCD	3.0 × 1.7	-
Sato et al. (2013)	Nd:YAG, CW	1	1000	CMOS	1.5 × 1.0	40 × 62.5

Arinami et al. (2015)	Nd:YAG, CW	10	500	CMOS	1.8×1.8	604×604 674×674
Yamada et al. (2015)	Nd:YAG, pulse	1	1000	CMOS	1.8×1.6	84×24
Koutani and Kobayashi (2015)	Nd:YAG, pulse	0.3 ~ 1	4	CCD	1.8×1.6	84×24
Sato et al. (2016)	Nd:YAG, CW	1	1000	CMOS	1.5×1.0	75×75

important in a measurement of flow fields with strong three dimensionality..

(b) Particle seeding

The size and materials of particles should be selected taking account of its follow-up capability to working fluid and effects of external forces including gravitational force and centrifugal force. For example, a sedimentation velocity of particles (U_g [m/s]) is calculated from a balance of gravitational force and viscous drag (Stokes law, equation 3-1).

$$U_g = \frac{gd_p^2(\rho_p/\rho_a - 1)}{18\nu} \quad 3-1$$

Here, g [m/s²] is the gravitational acceleration, d_p [μm] is the particle diameter, ρ_p, ρ_a [g/m³] are the particle density and air density, and ν [m²/s] is the air viscosity. As presented in equation 3-1, U_g increases with d_p and ρ_p . Moreover, large d_p and ρ_p enlarge an unfavorable effect of centrifugal force and degrade follow-up capability, thus, oil particles of nanoscale are most widely used in resent studies (table 3-2). Although the density of oil is much larger than that of air ($\rho_p/\rho_a \sim 800$), U_g is on the order of 10^{-4} [m/s] owing to the extremely small particle diameter.

Another important factor is spray density of particles. High spray density contributes to reduce data missing rate, however, excessively high density causes speckle noise on images and degrades accuracy of image processing. Furthermore, it is considered that spatial resolution would be better in the case that individual particles can be distinguished than the case where particles are contiguous each other and detected as a single large particle in images.

(c) Particle image recording

The camera parameters including f-number, sampling rate, and exposure time are significant factors of data accuracy in PIV. The wind velocity is calculated based on a moving distance of particles L [pixel] between two successive images as follows,

$$L = \alpha \times V \times \Delta t \quad 3-2$$

Here, α [pixel/mm] is the transformation coefficient of real scale and pixel scale, V [m/s] is a velocity of a particle group, Δt [s] is the time interval between two images. It is known that measurement accuracy is reduced if L is too large or too small, and the acceptable range of L is from 10 pixel (L_{max}) to 0.1 pixel (L_{min}) though it varies depending on image processing algorithms. Specifically, most favorable L is between 4 to 5pixel (e.g. Raffel 2002). Hence, Δt should be determined so as to satisfy this requirement for L .

The ratio of L_{max} and L_{min} indicates a measurable velocity range, and it is estimated to be 100 to 200. On the other hand, velocity resolution is determined based on equation 3-2 by substituting $L=0.1$, α and Δt ; the latter two depend on an experimental condition. Measurable range and resolution of velocity are crucially important in the measurement of a turbulent flow field around a bluff body, where both high speed and low speed flow exist simultaneously, and wind velocity is extremely small in a wake region and a flow separation region. For example, figure 3-3 shows the spatial distribution of a temporally averaged wind velocity around a 2D street canyon converted in pixel unit ($\alpha = 5.83$ pixel/mm, $\Delta t = 0.001$ s) obtained by the authors (Sato et al. 2016). In figure 3-3, the maximum moving distance is less than 10 pixel and within the acceptable range, while the minimum moving distance is smaller than 1 pixel at the region behind the windward block, suggesting velocity resolution is not enough. This problem is expected to frequently occur in wind tunnel experiments targeting airflow around urban building

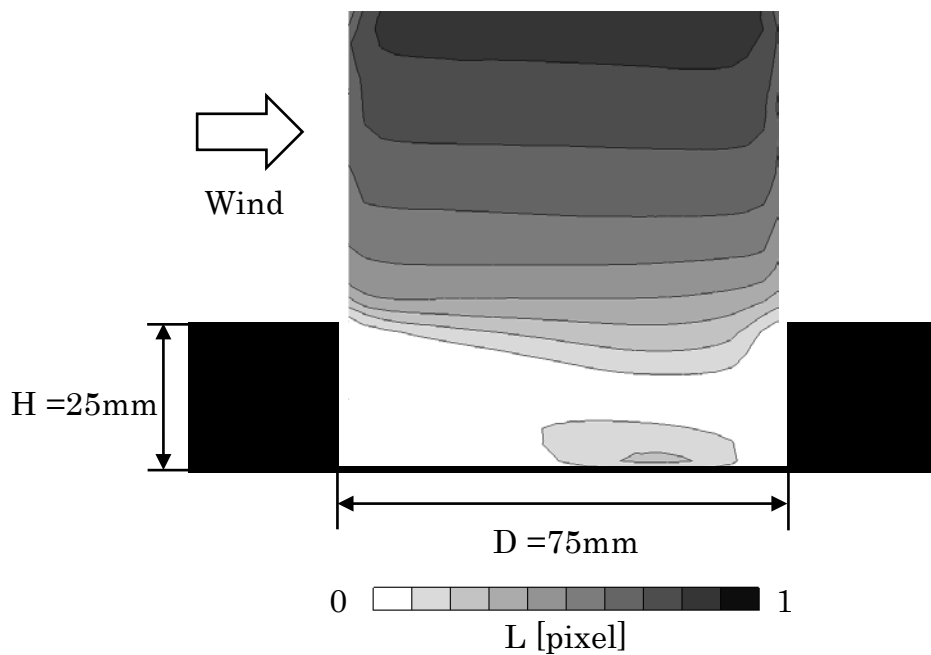


Figure 3-3 Spatial distribution of temporally averaged streamwise velocity around a 2D street canyon converted in pixel unit

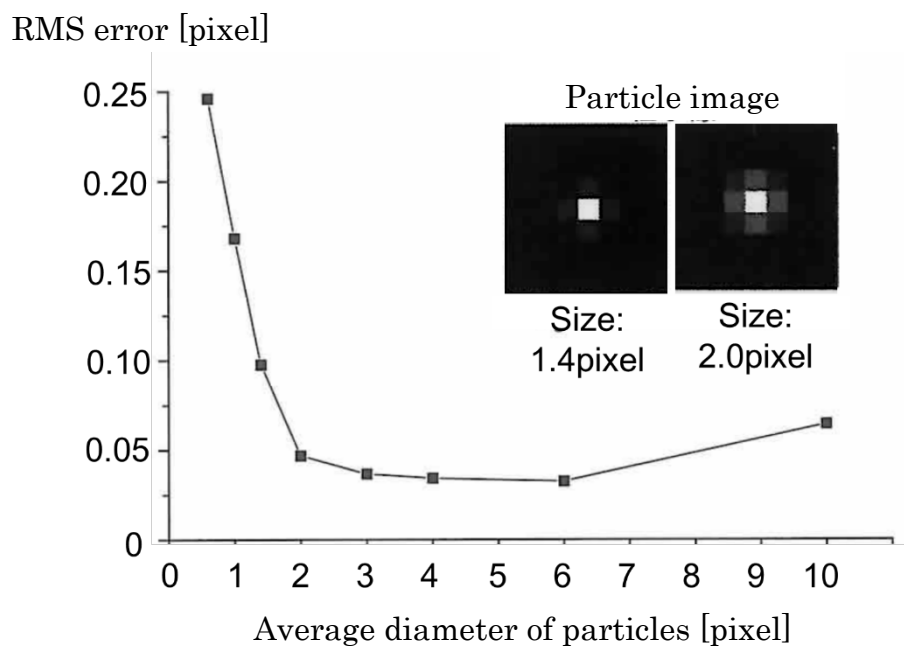


Figure 3-4 Relation between particle size and measurement error (quoted from the text book published from the visualization society of Japan (2012) and modified by author)

arrays, thus, careful attention is necessary in particular for the research on the instantaneous flow fields.

Meanwhile, the minimum velocity resolution of 0.1 pixel is achieved in an ideal case that particle diameter is 2 to 3 pixel on images (Westerweel 2000). If this requirement is not satisfied, measured velocity resolution might become larger than 0.1 pixel because of a bias error (see figure 3-4). This error is called as peak locking, where a frequency distribution of moving distance of particle groups is unreasonably biased toward integer values. As past studies presented (e.g. Westerweel 2000), the peak locking can be avoided by enlarging f-number of a camera or taking defocused image in the image recording process (step (d), figure 3-2). However, it is considerably difficult to apply these methods in the typical experimental condition presented in figure 3-1 and table 3-2. More detailed discussion about this problem is conducted in the following sections.

(d) Preprocessing of particle image

The purpose of image preprocessing is to effectively extract information by enhancing image quality using various types of image correction methods, such as contrast stretching, gamma correction, and median filter. However, it is highly challenging to determine what type of image enhancement method is effective, moreover, distinguishable differences might appear in analysis results depending on each method. In the workshop of fourth PIV challenge (Kahler et al. 2016), a research team applied an advanced preprocessing comprised of three methods: harmonic mean subtraction, reduction of cross-talk and contrast improvement. In contrast, another team applied simple preprocessing such as just mean subtraction though same image data were distributed to them. Appreciable differences are observed in their image processing

results, and it might be due to the difference of image preprocessing method.

(e) Image processing and velocity calculation

Selection of an image processing algorithm and setting of analysis parameters including interrogation window size, iteration number and grid spacing have a significant influence on analysis results. The development of analysis algorithms has been an important subject for PIV researchers and various types of algorithms have been proposed in past studies. Window deformation iterative multigrid (WIDIM), which is an algorithm comprised of a recursive cross-correlation method and image transforming method, is considered to be a highly reliable algorithm (Adrian 2005; Scarano 2005; Stanislas et al. 2005). In PIV experiments, data accuracy tend to decline in the regions where spatial velocity gradient and flow deformation are large, however, advanced algorithms including WIDIM show good performance even in these severe conditions.

(f) Removing error and data interpolation

To remove error data, following methods are frequently used: threshold setting for correlation coefficient of particle pattern matching, referring a histogram of instantaneous velocity, and comparing spatially adjacent velocities. Unreasonable error data caused by random noise are mostly removed by these simple methods (Raffel et al. 2002). On the other hand, an area averaging and a bilinear function are often used for data interpolation. Moreover, advanced methods based on fluid dynamics have been suggested in the recent studies, however, there are few studies which employed these advanced methods.

3.3 Peak locking problem

As mentioned above, the minimum velocity resolution of 0.1pixel is achieved under the condition that the average particle diameter on images is 2~3 pixel (The visualization society of Japan 2002), and peak locking problem might occur if the average particle diameter is less than this size. Although few papers mention the average particle size on images, it is possible to estimate whether this requirement is satisfied in past studies from relevant data presented in figure 3-1 and table 3-2. In this section, first the average particle size on camera screen is calculated in micro meter unit, then it is compared with the image sensor size of a digital camera (figure 3-5).

According to Raffel et al. (2002), the average particle diameter on a camera screen (d_{τ} [μm]) is estimated by equations 3-3 and 3-4.

$$d_{\tau} = \sqrt{(Md_p)^2 + d_{diff}^2} \quad 3-3$$

$$d_{diff} = 2.44F(M + 1)\lambda \quad 3-4$$

Here, d_{diff} [μm] is the diameter of a disk-like image pattern formed by light diffraction (airy disc), λ [nm] is the wavelength of laser light, M is the magnification ratio determined by the mutual position relation of the laser sheet, camera lens and camera screen, F is the f number of the camera lens. As figure 3-1 and table 3-2 show, the typical values of λ and d_p are 532 nm and 1~10 μm , respectively. Although the exact values of M and F are not presented, M is presumed to be from 0.1 to 0.2 from the fact that the distance between the laser sheet and camera is no more than 1.5 m and an outline dimension of a camera is a few decimeters in most cases, while F is considered to be a small value considering that incident light to the camera screen decreases with the increase of F and it frequently becomes a critical problem of PIV experiments. If F is assumed to be 2.8, d_{diff} and d_{τ} are estimated to be 4 μm and 4~5 μm , respectively.

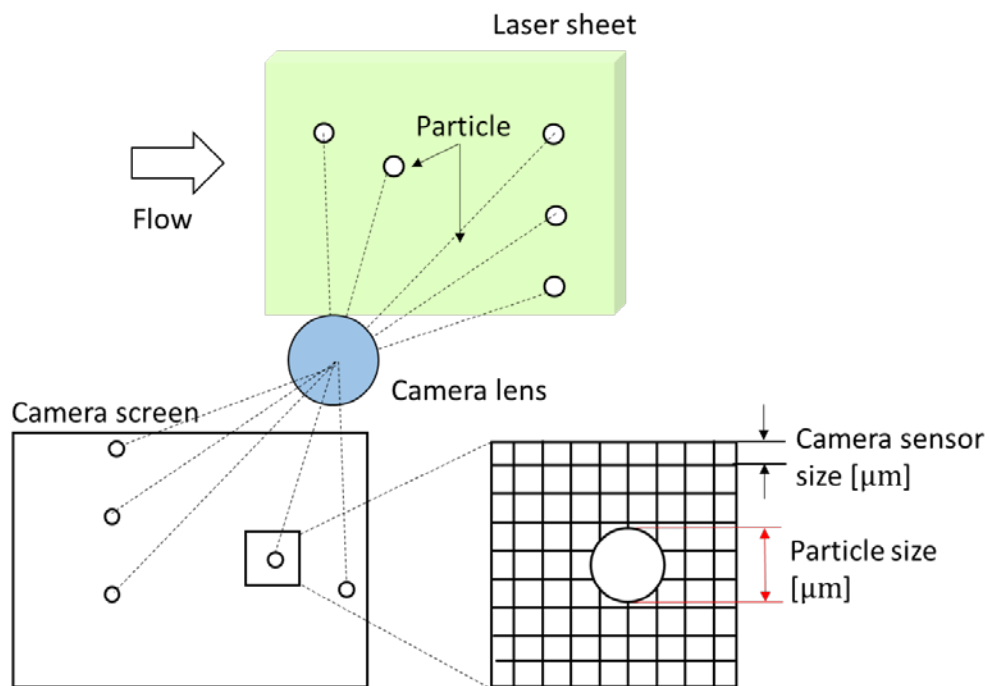


Figure 3-5 Analysis procedure of particle size on image

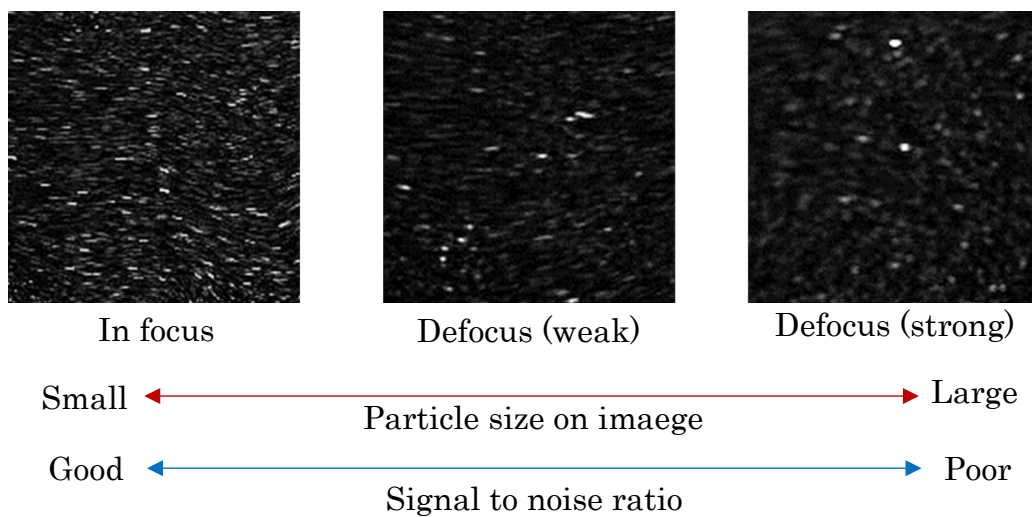


Figure 3-6 Particle image data with different focus conditions

On the other hand, average sizes of image sensors of CCD and CMOS camera employed in recent PIV experiments are 10 $\mu\text{m}/\text{pixel}$ and 15 $\mu\text{m}/\text{pixel}$ (Hain et al. 2007a), therefore, the average particle size on image is presumed under 1 pixel and it does not satisfy the required condition (2 ~ 3 pixel).

Furthermore, it is considerably difficult to satisfy this condition by changing experimental conditions. λ , d_p and camera pixel size are determined by device specifications and they are unchangeable parameters. Similarly, M is decided almost completely depending on the optical access of a wind tunnel. Only F can be determined arbitrarily, however, large F decreases luminance of particles and degrades signal to noise ratio (SNR). For the same reason, it is difficult to enlarge particle size by adding defocus on purpose (figure 3-6). Hence, it is considered that peak locking problem is generally unavoidable in the typical experimental condition presented in figure 3-1 and table 3-2.

3.4 Countermeasure for peak locking problem

Except for changing experimental conditions, the peak locking problem might be mitigated by improving image quality in preprocessing step (figure 3-2, step (d)), or applying an image processing algorithm which incorporates a countermeasure for peak locking. Regarding to the processing algorithm, various algorithms have been developed (e.g. Stanislas et al. 2005), however, these advanced algorithms tend to increase calculation load, and moreover, it is pointed out that several algorithms modify calculation results without a theoretical support (Okamoto 2004; Chen and Katz 2005).

Thereby, this section focuses on the other approach. Various preprocessing methods were tested and the mask correlation method (MCM) developed by Eto et al. (1996) presented excellent performance. Although MCM was developed originally for particle

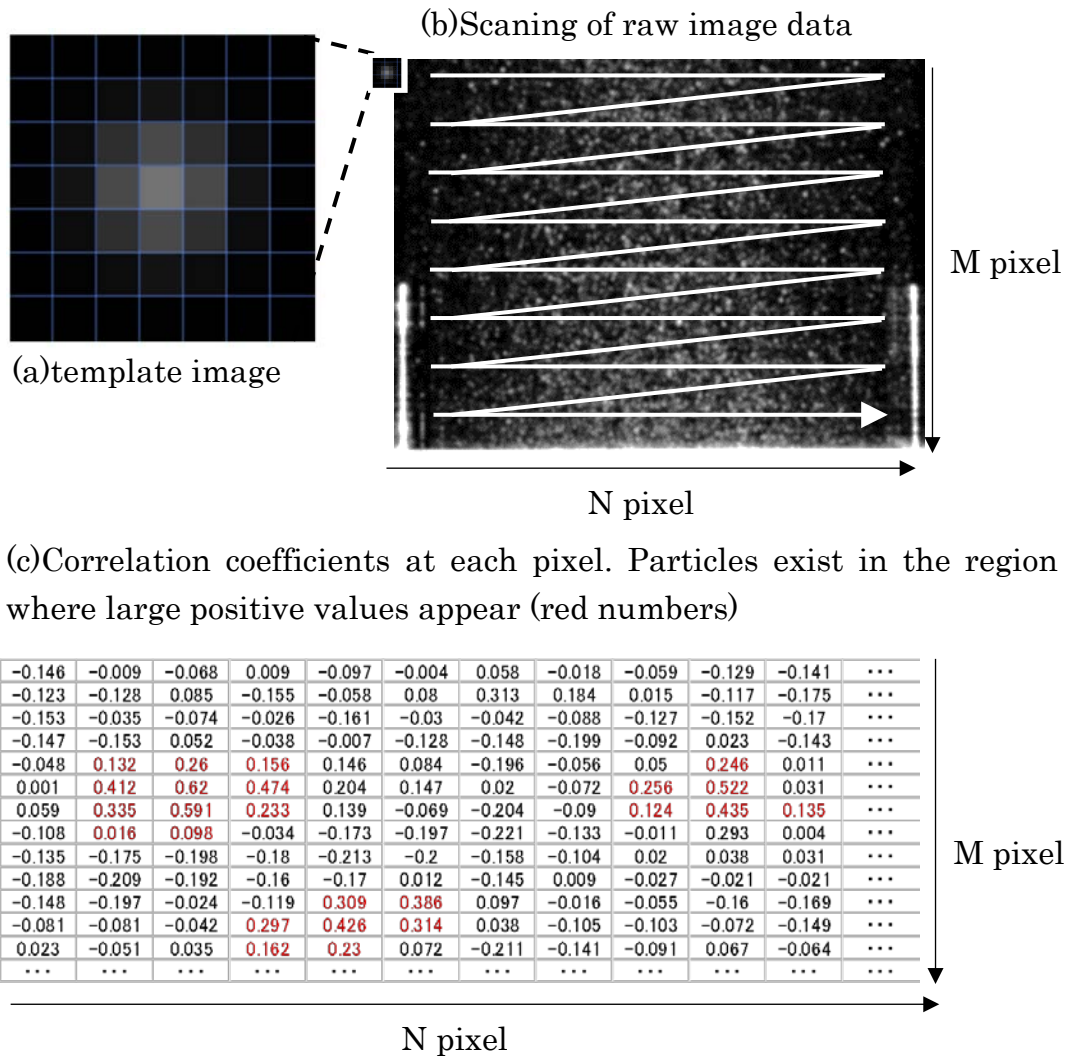


Figure 3-7 Procedure of Mask correlation method (MCM)

tracking velocimetry (PTV), a main contribution of MCM is enhancing particle signal intensity and extending image contrast, hence, MCM is considered to be useful for PIV as well. The procedure of MCM in the present study is presented in figure 3-7. First, an ideal particle image with Gaussian brightness distribution (equation 3-5) is created.

$$f = \exp\left(-\frac{(x - x_0)^2 + (y - y_0)^2}{2\sigma^2}\right) \quad 3-5$$

Here, σ is the ideal particle radius, x_0 and y_0 are central coordinates of the ideal particle in the streamwise and vertical direction. The ideal particle diameter is defined as 3pixel in the present study, and the template image of the ideal particle is presented in figure 3-7(a). The raw images are scanned by this template image, and correlation coefficients between the ideal particle and raw images are calculated in the range of $(x_0 \pm i, y_0 \pm j, i, j = -3, +3)$ (figure 3-7(b)). Then, new luminance values at each point are determined in the range of 0 ~ 255 based on the correlation coefficients (-1 ~ +1) regardless of luminance values in the raw images (figure 3-7(c)). This is an important feature of MCM. Namely, even for particles with low luminance in the raw images can be used as valid data in the following analysis if only the correlation coefficient is large. Other features of MCM are small calculation load (Appendix 3-1), and little dependency on experimenters' skill and experience. Based on these advantages, MCM is considered to be a useful method from a practical point of view.

3.5 Performance test of MCM

This section investigates the performance of MCM to mitigate peak locking problem using experimental data obtained by a wind tunnel experiment conducted by authors (Sato et al. 2016).

3.5.1 Quality of the sample images

The sample data were obtained by a PIV experiment around a 2D street canyon with canyon aspect ratio was 3 ($W/H = 3$, see figure 3-8). The Experimental parameters which relate to d_τ on the sample images were as follows: $\lambda = 532 \text{ nm}$, $d_p = 1 \text{ }\mu\text{m}$, $M =$

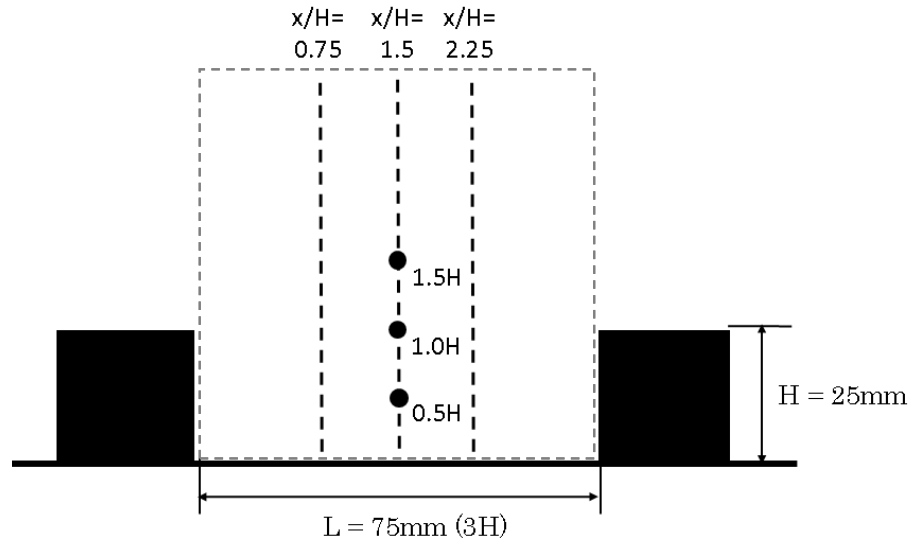


Figure 3-8 Roughness arrangement of the TR-PIV experiment (Sato et al. (2016)). Black dots: Instantaneous velocity was obtained (figure 3-10 and 3-11), three dashed lines: profiles of turbulent statistics was obtained (figure 3-12), gray dash line: measurement area

0.117, $F = 2.8$, and the image sensor size of the CMOS camera was $20\mu\text{m}$. By substituting these parameters into eq.3-3 and 3-4, d_τ was estimated to be about 0.2pixel.

Figure 3-9(a) is a raw image obtained by Sato et al. (2016), and figure 3-9(c) and figure 3-9(e) are enlarged views in the red and yellow squares in figure 3-9(a). The particle diameter in figure 3-9(c) and (e) is small apart from a few particles and seems not to satisfy the required condition ($d_\tau = 2\sim 3$ pixel, figure 3-4). In addition, the luminance is low and image contrast is poor in figure 3-9(c) and (e).

MCM was applied for these images and an enhanced image is presented in figure 3-9(b), figure 3-9(d) and figure 3-9(f). The particle luminance is much larger than that in the raw images, and the particle diameter is also enlarged. Table 3-3 presents the ensemble averaged values of spatial average and standard deviation of the particle luminance within the 30×30 pixel squares with the blue dashed lines in figure 3-9(c)-(f). The large

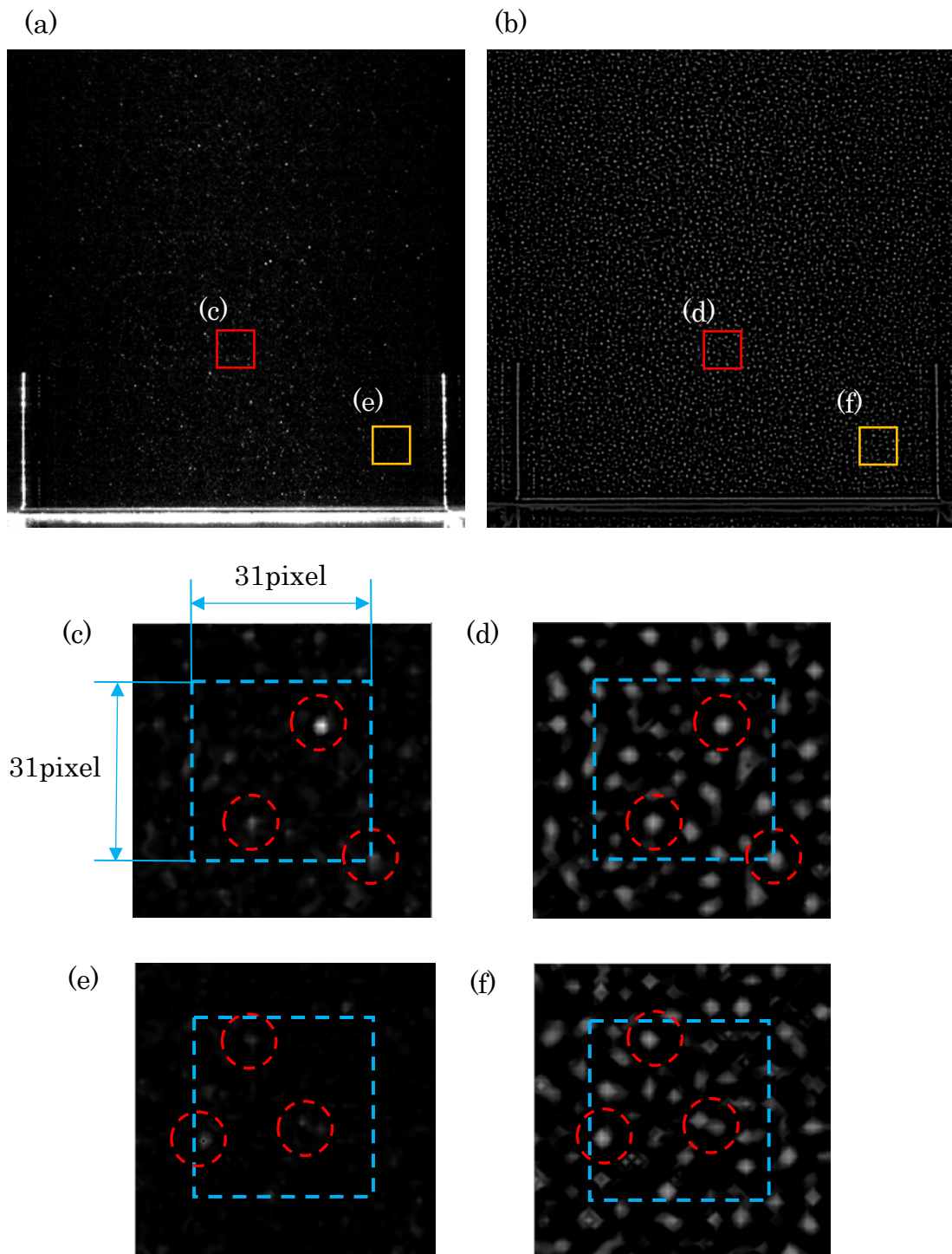


Figure 3-9 Results of preprocessing by MCM. (a) and (b): raw and modified image. (c), (d), (e) and (f): enlarged views at the red and yellow squares. Blue dashed lines: squares of 30×30 pixel. The red circles indicate same particles.

Table 3-3 Quality of the raw image of modified image

	Average luminance	Standard deviation
Raw image	9.50	14.4
Modified image	19.4	30.9

standard deviation indicates high image contrast, and it is considered important for image processing in the next step.

3.5.2 Test Results

The raw and enhanced images were analyzed by a direct cross-correlation algorithm combined with WIDIM. The interrogation window size was 31×31 pixel, and calculation was iterated three times.

Figure 3-10 presents histograms of instantaneous moving distances of particle groups between two successive images (Δx [pixel]: streamwise direction, Δz [pixel]: vertical direction). Every data was obtained on the center line of the canyon ($x/H=1.5$, see figure 3-8) and three different height: $z/H=1.5$ (figure 3-10(a) and (d)), $z/H=1.0H$ (figure 3-10(b) and (e)), and $z/H=0.5H$ (figure 3-10(c) and (f)). Flow characteristics such as turbulent intensity and shear stress are much different at each location, hence, it can be investigated whether the image correction by MCM is applicable for various types flow fields.

The dashed lines in figure 3-10 are the image processing results of the raw images. Strong peak locking is observed in all the figures, namely local maximum peaks appear in integer numbers while local minimum peaks occur in $n+0.5$ (n is integer values). This

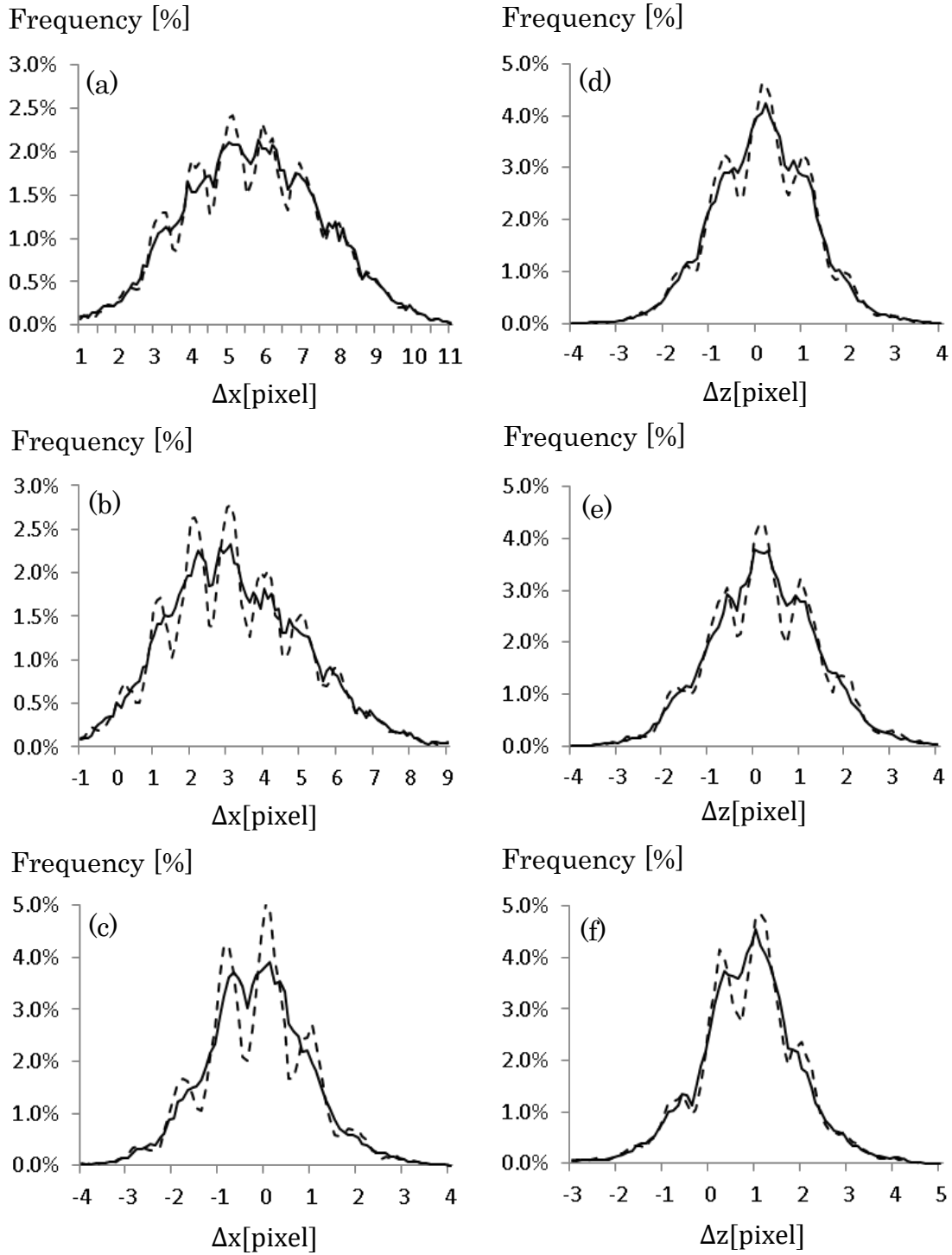


Figure 3-10 Histograms of the instantaneous displacement in pixel units, dashed line: without MCM, solid line: with MCM, (left): streamwise displacement, (right): vertical displacement, (a),(d): $(x/H, z/H)=(1.5, 1.5)$, (b),(e): $(x/H, z/H)=(1.5, 1.0)$, (c),(f): $(x/H, z/H)=(1.5, 0.5)$

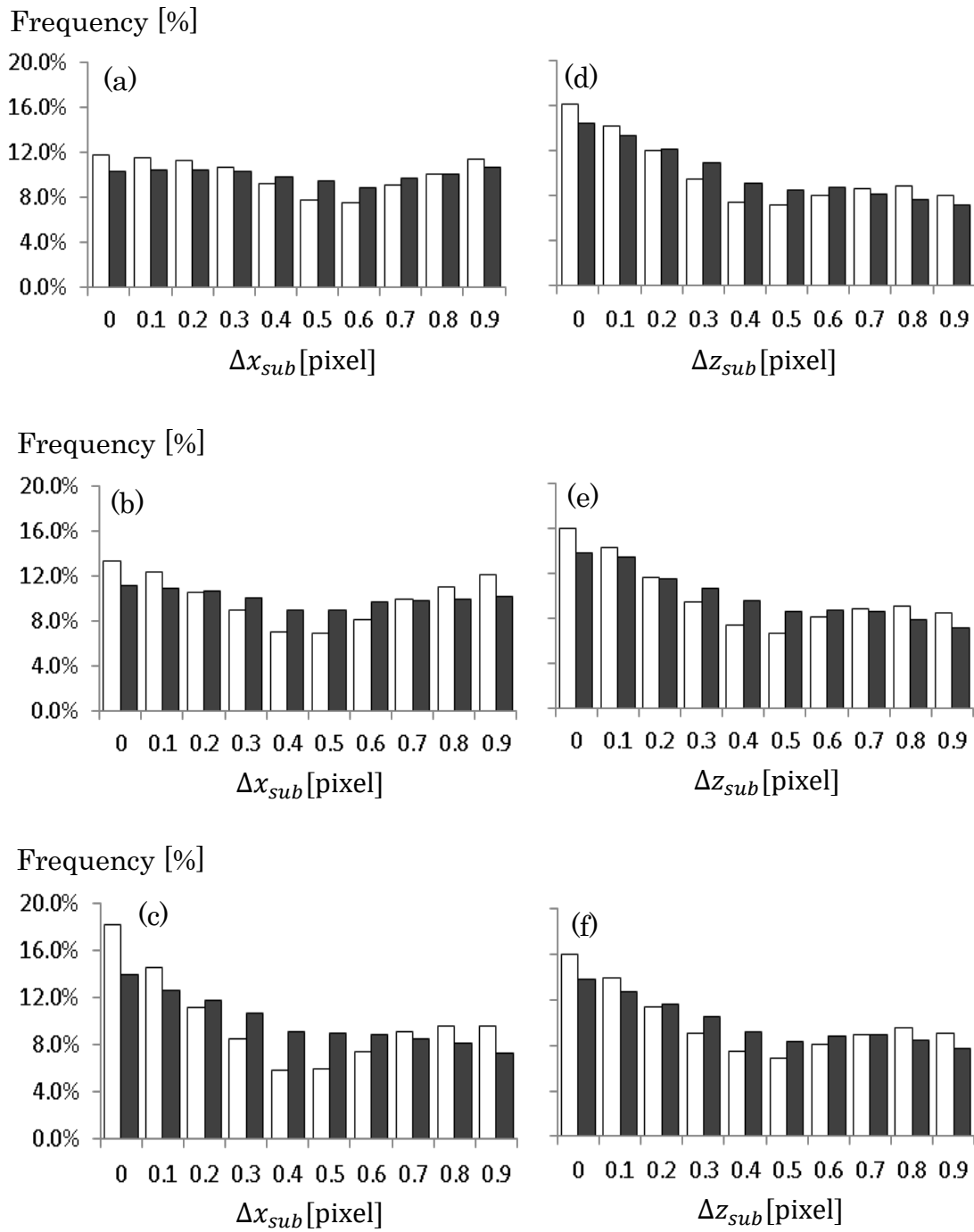


Figure 3-11 Histograms of the sub pixel part of instantaneous displacement, white bar: without MCM, gray bar: with MCM, (left): streamwise displacement, (right): vertical displacement, (a),(d): $(x/H, z/H)=(1.5, 1.5)$, (b),(e): $(x/H, z/H)=(1.5, 1.0)$, (c),(f): $(x/H, z/H)=(1.5, 0.5)$

bias error is especially serious within the canyon (figure 3-10(c) and figure 3-10(f)), where the variation width of the velocity is small. For example, in figure 3-10(c), the frequency in -0.5pixel is supposed to be higher than that in -0.9pixel considering that the maximum peak appears in 0pixel. However, the opposite result is observed and the frequency in -0.5pixel is 2.2 % lower than that in -0.9pixel.

Figure 3-11 are histograms of the sub pixel part of the instantaneous moving distances of particle groups at the same locations with figure 3-10. White bars are the results of the raw data. Frequencies at each pixel should be equal if bias error does not occur however, frequencies at 0.4, 0.5, and 0.6 pixel are unreasonably small in all the figures.

On the other hand, peak locking is drastically mitigated in case MCM is applied (solid lines) although it is not solved completely. For example, the difference of the frequencies between -0.5pixel and -0.9pixel is only 0.1% in figure 3-10(c). Similarly, the difference of the frequencies between 0pixel and 0.5pixel is reduced to 1% in figure 3-11(a) and figure 3-11(b). Moreover, the frequency distributions in figure 3-11(c), (d), (e), and (f) are approximately smooth. As it was mentioned above, turbulent flow field properties are different at the three locations where sample data are obtained, however, peak locking is largely mitigated at all the positions, indicating a wide application scope of MCM.

$\Delta x[\text{pixel}]$, $\Delta z[\text{pixel}]$ are converted to the streamwise and vertical velocity components ($u[\text{m/s}]$, $w[\text{m/s}]$) by equation 3-6.

$$u = m \frac{\Delta x}{\Delta t}, \quad w = m \frac{\Delta z}{\Delta t} \quad 3-6$$

Here, $m[\text{mm/pixel}]$ is the transformation coefficient of real scale and pixel scale ($=a^{-1}$). Figure 3-12 presents vertical profiles of temporally averaged wind velocity (U/U_{20H}), standard deviations of streamwise and vertical velocity component (σ_u/U_{20H} and σ_w/U_{20H}), Reynolds stress ($-\overline{u'w'}/u_2^*$), and skewness of the two velocity component

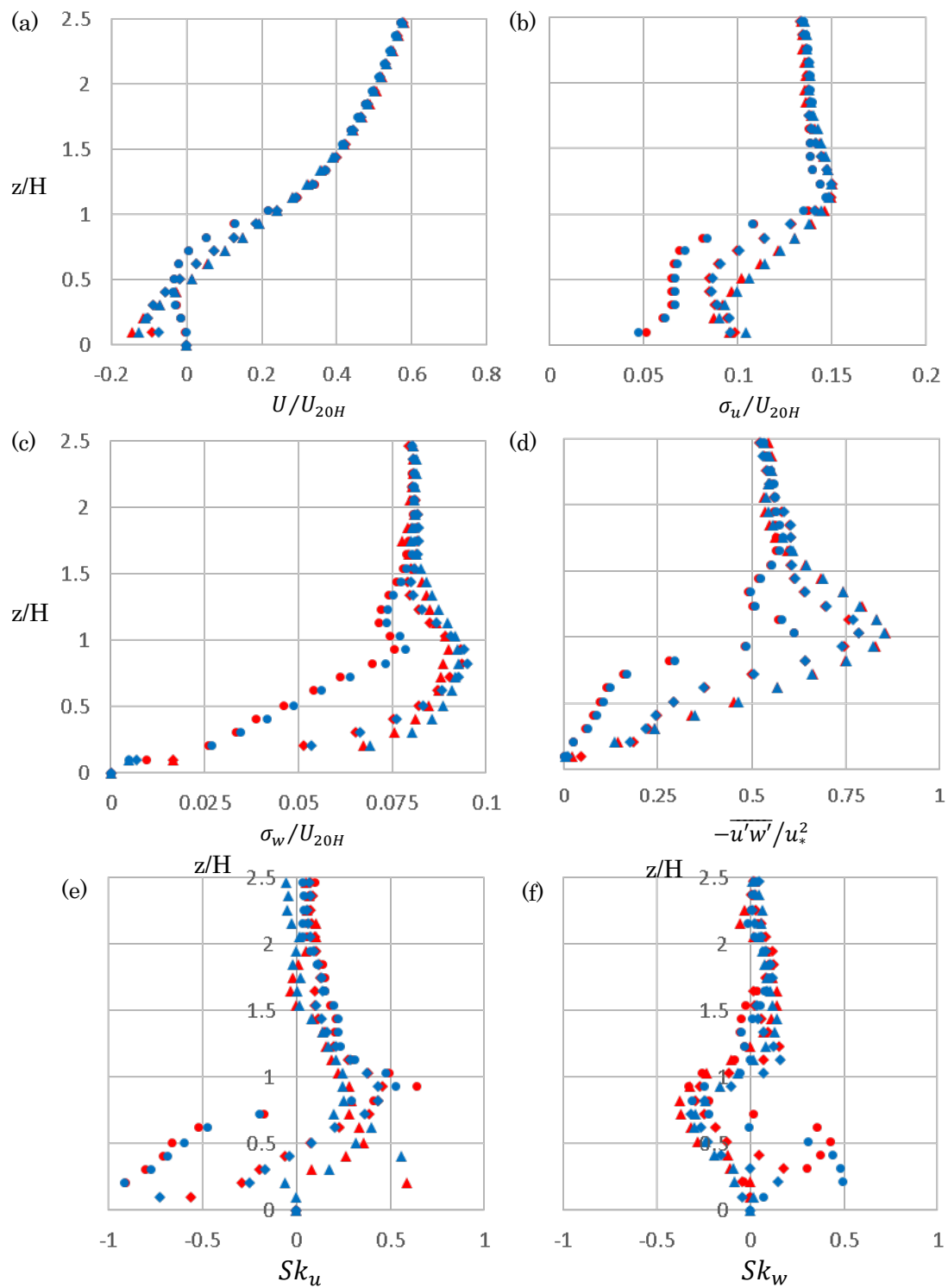


Figure 3-12 Vertical profiles of streamwise wind velocity and turbulent statistics measured at the three lines in figure 3-8. Blue plots: without MCM, red plot: with MCM. (a) U/U_{20H} , (b) σ_u/U_{20H} , (c) σ_w/U_{20H} , (d) $-\overline{u'w'}/U_*^2$, (e) Sk_u , (f) Sk_w

(Sk_u , and Sk_w) measured at the three lines in figure 3-8. Here, U_{20H} [m/s] is the free stream wind velocity measured at 20 times of the roughness height, and u_* [m/s] is the friction velocity calculated by the drag coefficient. The difference between blue plots (MCM is not applied) and red plots (MCM is applied) is negligible in figure 3-12(a) (U/U_{20H}), while a several percent difference confirmed in figure 3-12(b), (c), and (d) (σ_u/U_{20H} , σ_w/U_{20H} , and $-\overline{u'w'}/u_*^*$) especially within the canyon. As figure 3-10 and figure 3-11 indicates, peak locking is error that the subpixel part of the moving distance of particle groups is not calculated correctly, and the frequency becomes large at integer values as if the moving distance is rounded off. Thus, peak locking have a little difference on arithmetical mean, while distinguishable error is caused in standard deviation and Reynolds stress. The small standard deviation might be one of the reasons of large skewness in case MCM is applied (figure 3-12(e) and figure 3-12(f)). The sign of Sk_u is unchanged between the two cases in the most parts of profiles, on the other hand, the sign of Sk_w is opposite at several points in figure 3-12(f). The shapes of histograms of Δz are close to Gaussian distribution with small distribution width, thus the sign of Sk_w is sensitive to the peak locking.

Meanwhile, Eto et al. (1996) points out the possibility that a preprocessing by MCM might increase negative effects of noise. It is considered that strong noise decreases correlation coefficients calculated in the image processing step (step (e), figure 3-2). Thereby, the negative effect of MCM is investigated by the vertical profiles of correlation coefficients on the center line of the canyon (figure 3-13). The white and black plots indicate the image processing results of the raw and enhanced images. The correlation coefficients of the enhanced images is about 10 % larger than that of the raw images.

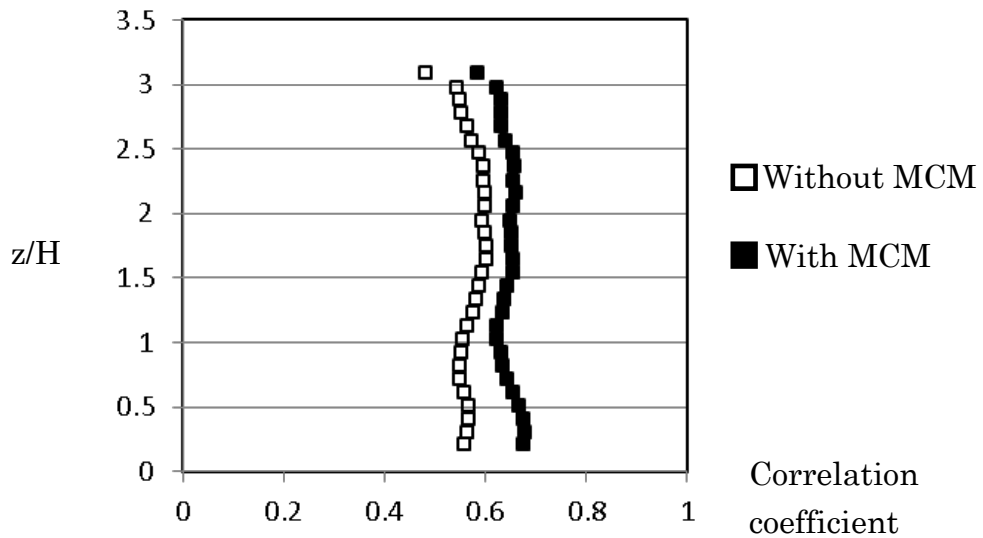


Figure 3-13 Vertical profiles of correlation coefficients on the center line of canyon ($x/H=1.5$), white plots: without MCM, black plot: with MCM

Hence, it is considered that the positive effect of MCM exceeded the negative effect, and the accuracy of image processing was improved at least in the present study.

3.6 Conclusion

This chapter overviewed past PIV experiments in wind engineering and urban atmospheric boundary layer science, and identified the typical experimental condition, and then we discussed peak locking problem.

The peak locking problem seems to be unavoidable especially if a PIV experiment is conducted in a large-size wind tunnel due to the fact that the averaged particle diameter on images tends to be smaller than the ideal size (2~3pixel). Hence, the author tried to mitigate the problem by applying MCM in the image preprocessing step. The particle diameter, particle luminance, and image contrast were enlarged compared to the raw images by the image correction with MCM. Subsequently the performance of MCM to mitigate peak locking problem was investigated using the experimental data obtained in

the actual wind tunnel experiment conducted by the authors (Sato et al. 2016). The particle diameter on the raw images was smaller than the ideal size, and strong peak locking arose without image correction, however, peak locking was solved almost completely by applying MCM regardless of flow field properties. In addition, MCM is not affected by the experimenter's skill, and does not increase calculation load, thus, MCM is considered to be a useful method for improving data accuracy of PIV experiments from a practical point of view.

Reference

- Adrian, R. J. (1984) Scattering particle characteristics and their effect on pulsed laser measurements of fluid flow: speckle velocimetry vs particle image velocimetry. *Applied optics*, 23(11), 1690-1691.
- Adrian, R. J. (2005) Twenty years of particle image velocimetry, *experiments in fluids*, vol. 39, pp. 159-169
- Akabayashi, S., Ohshima, T., Arinami, Y., Okubo, H., Yang, X., Sakagushi, J. (2013) Air flow measurements in a scale model of a room and method selection of seeding with tracer particles: study on PIV measurement and analysis for room air flow distribution part 1 (in Japanese), *journal of environmental engineering (transactions of AIJ)*, vol.78, pp. 631-638
- Annalisa, B. D., Paolo, M., Giovanni, L., Giorgio, Q. (2014) Water-channel study of flow and turbulence past a two-dimensional array of obstacles, *boundary-layer meteorology*, published online: DOI 10.1007/s10546-014-9987-2
- Arinami, Y., Akabayashi, S., Takano, Y., Tomnaga, Y., Sakagushi, J. (2015) Visualization and measurements for fluctuating cross ventilation air flow in simple house model using large size boundary layer wind tunnel study on PIV measurement and analysis for room air flow distribution part 2, *journal of environmental engineering (transactions of AIJ)*, vol. 708, pp. 127-134
- Caton, F., Britter, R.E., Dalziel, S. (2003) Dispersion mechanisms in a street canyon, *atmospheric Environment*, vol.37, pp. 693-702
- Chen, J. and Katz, J. (2005) Elimination of peak-locking error in PIV analysis using the correlation mapping method, *measurement science and technology*, vol.16, pp.1605-1618
- Eto, T., Takehara, Y. Michioku, K. Hisano, S. (1996) A study on particle identification in PTV –particle mask correlation method- (in Japanese), *proceedings of hydraulic engineering*, vol.40, pp.1051-1058
- Hain, R. and Kahler, C. J. (2007) *Fundamentals of multiframe particle image velocimetry*

- (PIV), experiments in fluids, vol. 42, pp. 575-587
- Hain, R., Kahler, C. J., Tropea, C. (2007a) Comparison of CCD, CMOS and intensified cameras, experiments in fluids, vol. 42. pp. 403-411
- Hart, D. P. (1999) Super-resolution PIV by recursive local-correlation, Journal of Visualization, vol. 103, pp.1-10
- Hino, M. (1992) *Fluid dynamics*, (in Japanese), asakura-shuppan press, Tokyo, Japan
- Huq, P., White, L. A., Carrillo, A., Redondo, J., Dharmavaram, S., Hanna, S. R., (2007) the shear layer above and in urban canopies, journal of applied meteorology and climatology, vol.46, pp. 368-376
- Kahler, C. J., Astarita, T., Vlachos, P. P., Sakakibara, J., Hain, R., Discetti, S., La F. R., Cierpka, C. (2016) Main results of the fourth international PIV challenge, experiments in fluids, vol.57, pp. 57-97
- Katsuki, T., Sato, A., Michioka, T., Hagishima, A. (2012) Comparison between wind tunnel experiments and field measurement values on flow field in real urban canyons (in Japanese), journal of environmental engineering (transactions of AIJ), vol.77, pp. 313-319
- Kikitsu, H., Okuda, Y., Ohashi, M., Kanda, J. (2007). Experimental evaluation of interaction phenomenon based on PIV measurement, fundamental study on vibration mechanism of three-dimensional prisms in consideration of wake interaction, journal of structural and construction engineering (transactions of AIJ), 612, 31-38
- Keane, R. D., Adrian, R. J. (1992) Theory of cross-correlation analysis of PIV images, applied scientific research, vol. 49, pp.191-215
- Kellnerova, R., Kukacka, L., Jurcakova, K., Uruba, V., Janour, Z. (2012) PIV measurement of turbulent flow within a street canyon: detection of coherent motion, journal of wind engineering and industrial aerodynamics, vol. 104-106, pp.302-313
- Koutani, H. and Kobayashi, T. (2015) Accuracy verification of processing methodology

- in particle image velocimetry for flow around building, *journal of environmental engineering (transactions of AIJ)*, vol.80, pp. 741-749
- Kline, S. J., Reynolds, W. C., Schraub, F. A., Runstadler, P. W. (1967) The structure of turbulent boundary layers, *journal of fluid mechanics*, vol. 30, pp. 741-773
- Liu, H., Liand, B., ZHU, F., Zhang, B., Sang, J. (2003) A laboratory model for the flow in urban street canyons induced by bottom heating, *advances in atmospheric sciences*, vol. 20, pp. 554-564
- Okamoto, K. (2004) PIV image evaluation algorithms (in Japanese), *transactions of the visualization society of Japan*, vol.24, pp.31-35
- Park, C. W., and Lee, S. J. (2000), Free end effects on the near wake flow structure behind a finite circular cylinder, *Journal of Wind Engineering and Industrial Aerodynamics*, 88, 231-246
- Pokrajac, D., Campbell, L. J., Nikora, V., Manes, C., McEwan, I. (2007) Quadrant analysis of persistent spatial velocity perturbations over square-bar roughness, vol. 42, pp. 413-423
- Raffel, M., Willert, C. E., Kompenhans, J. (2002) *Particle image velocimetry*, springer Japan, Tokyo, Japan
- Reynolds, R. T., Castro, I. P. (2008). Measurements in an urban-type boundary layer. *Experiments in Fluids*, 45, 141-156
- Salizzoni, P., Marro, M., Soulhac, L., Grosjean, N., Perkins, R. J. (2011) Turbulent transfer between street canyons and the overlying atmospheric boundary layer, *boundary-layer meteorology*, vol. 141, pp.393-414
- Sato, T., Hagishima, A., Ikegaya, N., Tanimoto, J. (2013) Particle image velocimetry measurement of unsteady turbulent flow around regularly arranged high-rise building models, *international journal of high-rise buildings*, vol.2, pp. 105-113
- Sato, T., Hagishima, A., Ikegaya, N., Tanimoto, J. (2016) Wind tunnel experiment on

- turbulent flow field around 2D street canyon with eaves, *journal of environmental engineering (transactions of AIJ)*, vol.81, pp. 467-476
- Scarano, F. (2005). Iterative image deformation methods in PIV, *Measurement Science and Technology*, 13, R1-R19
- Sharon, M., Yardena, B., Tomer, D., URe, S. (2014) Canopy edge flow: a momentum balance analysis, *Journal of hydrology*, vol.6, pp. 1-15
- Simoens, S., Ayrault, M., Wallace, J. M., (2007) The flow across a street canyon of variable width—part 1: kinematic description, atmospheric environment, vol.41, pp. 9002-9017
- Stanislas, M., Okamoto, K., Khler, C. J. (2003) Main results of the first international PIV challenge, *measurement science and technology*, vol.14, pp. R63-R89
- Stanislas, M., Okamoto, K., Khler, C. J., Westerweel, J. (2005) Main results of the second international PIV challenge, *experiments in fluids*, vol.39, pp. 170-191
- Stanislas, M., Okamoto, K., Kahler, C. J., Westerweel, J., Scarano, F. (2008) Main results of the third international PIV challenge, *experiments in fluids*, vol.45, pp.27-71
- Takimoto, H., Moriwaki, R., Tsukuni, M., Kanda, M. (2008) PIV method for turbulence statistics within and above outdoor urban scale model (in Japanese), *proceedings of hydraulic engineering*, vol.52, pp.259-264
- Takimoto, H., Sato, A., Onomura, S., Kanda, M. (2009) PIV measurement of urban canopy turbulence intercomparison study between outdoor and indoor urban scale model (in Japanese), *proceedings of hydraulic engineering*, vol.53, pp.241-246
- Takimoto, H., Sato, A., Barlow, J. F., Moriwaki, R., Inagaki, A., Onomura, S., Kanda, M. (2011) Particle image velocimetry measurements of turbulent flow within outdoor and indoor urban scale models and flushing motions in urban canopy layers, *boundary-layer meteorology*, vol. 140, pp. 295-314
- Takimoto, H., Inagaki, A., Kanda, M., Sato, A., Michioka, T. (2012) Length-scale

similarity of turbulent organized structures over surfaces with different roughness types, boundary-layer meteorology, vol.147, pp. 217-236

The visualization society of Japan (2002) *PIV handbook* (in Japanese), morikita-shuppan press, Tokyo, Japan

Uehara, K., Mochida, A., Yamao, Y., Oikawa, S. (2007) Wind tunnel experiments on improving the natural ventilation of a street canyon, journal of Japan society for atmospheric environment, vol.42, pp. 301-309

Willert, C. E. and Gharib, M. (1991) Experiments in fluids digital particle image velocimetry, experiments in fluids, vol. 193, pp. 181-193

Westerweel, J. (2000) Theoretical analysis of the measurement precision in particle image velocimetry, experiments in fluids, vol.29, pp.S003-S012

Yamada, S., Koutani, H., Momoi, Y., Nishimura, K. (2015) Space scaling of velocity modulation in separation flow around building, proceeding conference of SHASE, Osaka, Japan

Yoshikawa, K., Okuda, Y., Ito, S., Ohashi, M., Sasaki, Y. (2003). Experimental study on aerodynamic force and wind flow around a three dimensional slender cylinder by synchronous wind pressure measurements with PIV, journal of structural and construction engineering (transactions of AIJ), 573, 53-6

Chapter IV

Study of coherent structure around high rise buildings

4.1 Introduction

The accurate estimation of wind characteristics in urban canopy layer and roughness sublayer has been one of the significant issues in terms of pollutant dispersion, thermal condition of pedestrian, and heat transfer between urban surfaces and the atmosphere. Thus, numerous wind tunnel experiments, computational simulations, and field observations have been performed for more than decades.

The classification of three flow regimes (skimming flow, wake interference, and skimming flow) in an urban canyon in terms of the canyon aspect ratio (ratio of the street width to canyon roof height) is one of significant phenomenological description (Oke 1988). This fundamental classification of mean flow structures in urban canyons has been used in following research. For example, Hunter et al. (1991) performed Reynolds averaged Navier-Stokes (RANS) simulations on flow fields around 2D street canyons under four conditions of canyon aspect ratio (1, 3, 5, and 7), and presented typical features of each flow regime. Similarly, Leonaldi et al. (2003) performed direct numerical simulations (DNS) for 2D street canyons with canyon aspect ratio from 0.33 to 19, and quantitatively evaluated the size of recirculation flows, locations of flow reattachment on the bottom of a canyon, and the size of a small vortex in front of the leeward building. Furthermore, more complicated flow structures around 3D roughness models have been also investigated by numerical simulations (e.g. Kanda et al. 2004, Coceal et al. 2006, Santiago et al. 2007) and wind tunnel experiments (e.g. Uehara et al. 2007, Reynolds and

Castro 2008). DNS conducted by Coceal et al. (2006) provides highly accurate data of temporally averaged flow field structures and spatial distributions of turbulent statistics for three cubical arrays (staggered, aligned and square array) with $\lambda_p = 25\%$ (λ_p is building plan area index, the ratio of the plan area occupied by obstacles to the total floor area). Furthermore, not only temporally averaged flow properties, unsteady turbulent organized structure (TOS) around urban roughness models have also been investigated in recent studies. For example, Large Eddy Simulation (LES) conducted by Kanda et al. (2004) on turbulent flow fields for square and staggered cubic arrays with various λ_p presents snapshots of low speed streaks elongated in the streamwise direction above the roughness models. Takimoto et al. (2011) performed outdoor and indoor experiments of turbulent flow fields around a cubic array with $\lambda_p = 25\%$ using PIV technique, and found out that instantaneous ‘flushing’ flow events occur intermittently around the roughness models in both outdoor and indoor experiments. Namely, low-speed upward flow (ejection) and high-speed downward flow (sweep) motions are observed once in a few minutes (outdoor experiment) and several seconds (indoor experiment). LES simulations by Inagaki et al. (2011), Michioka et al. (2011), and Michioka et al. (2014) demonstrates that strong ejection events are caused in urban canopy in association with the passing of low speed streaks above the roughness, instantaneously increasing the scalar and heat transport from UCL.

Owing to these studies, various features of turbulent flow fields around urban roughness models have been disclosed, however, most of these studies were conducted with block arrays which consists of cubes or short blocks characterized by low building aspect ratio (ratio of frontal area to roof area), and it is uncertain to what extent the airflow nature of idealized block arrays can be treated as prototypes of flow fields in real urban conditions.

Namely, the geometrical conditions with cubes and short blocks might be suitable for simplifying residential districts of detached houses or traditional European cities, however, airflow characteristics of real urban areas consist of not only low rise buildings but also slender high rise buildings are difficult to be modeled. In particular, several researchers pointed out that various geometry factors such as height variability, rotation angle of blocks against mean flow direction, and slenderness of blocks affect the nature of turbulent flow fields around urban building models. According to the effect of slenderness of blocks, Huq et al. (2007) conducted PIV experiments on turbulent flow fields for two uniform block arrays with different building aspect ratio (1 and 3) in a water tunnel. Their experiments revealed that the shapes of streamwise velocity profiles are different between the two cases, and shear layer which is defined as the vertical extent of the linear region of the mean velocity profile near the building height shows different tendency. Hagishima et al. (2012) measured drag coefficients (C_d) of staggered uniform block arrays with various conditions, and presented that the relations between C_d and λ_p are different by the block slenderness and block rotation angle. This result suggests that 1) aspect ratio is an index of both slenderness and streamline nature of a roughness element, 2) the flow field around a slender block array with high aspect ratio is different from the typical skimming flow observed around block arrays with low-aspect ratio under high λ_p condition due to the less bluff-body nature. In fact, Li et al. (2008) conducted numerical simulation of flow over a block array with high aspect ratio using LES and investigated vertically aligned primary recirculation of mean flow within the canopy.

Although these researches imply the necessity of considering the flow around high rise building arrays, the existing data is still limited, and the holistic features have not been clarified. Under these circumstances, in this Chapter, turbulent flow fields around a

building model consist of slender rectangular blocks are observed by PIV experiment in a wind tunnel. The experimental set-up is outlined in the following section and the profiles of turbulent statistics as well as the results of quadrant analysis are presented in section 4.2. Subsequently, in section 4.3, several typical features of instantaneous flow field are depicted, and section 4.5 presents discussion and major conclusion.

4.2 Experimental set up

4.2.1 Wind tunnel and configuration of the array

The experiment was conducted in the wind tunnel at the Interdisciplinary Graduate School of Engineering Sciences, Kyushu-university, Japan. The facility was a low-speed single-return tunnel with a test section of height 1m, width 1.5m and length 19.5m including an underground pit. The floor of the test section with a length of 8m was covered by a block array. All blocks made from wood with a uniform base of 8mm×8mm and height of 25mm were arranged in the staggered layout with plan area ratio $\lambda_p = 4\%$. The layout of the measurement system and block array is schematically shown in figure 4-1 and figure 4-2.

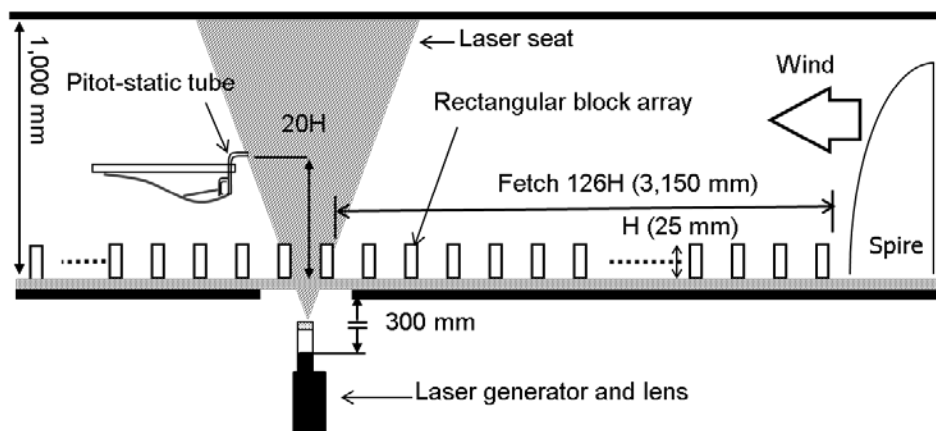


Figure 4-1 Side view of experimental set up

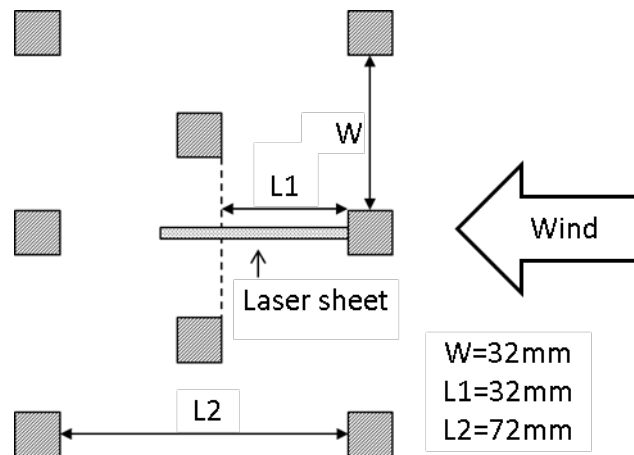


Figure 4-2 Schematic plan view of block array and the position of laser sheet

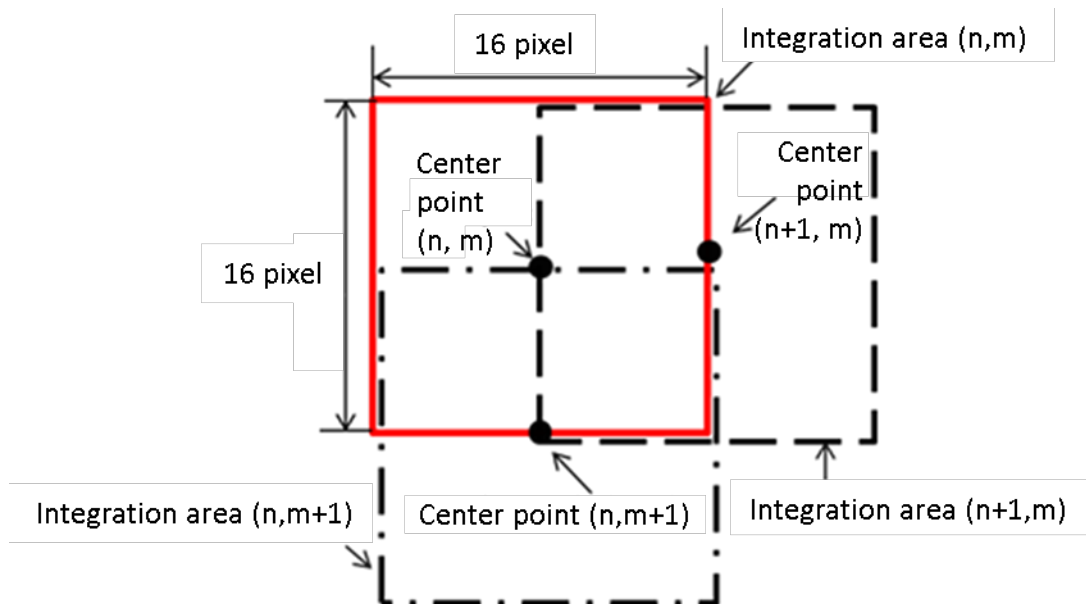


Figure 4-3 Size and position definition of integration area

4.2.2 Particle image velocimetry

The PIV measurement was performed by illuminating oil particles of about $1\mu\text{m}$ diameter with a 3mm thick light sheet produced by Nd:YAG 2W laser (operating at 532nm) and a concave lens (focus length is -20mm). The images were photographed at a

frequency of 1,000Hz for a period of 43.6 seconds by using a CCD camera (FASTCOM SA-1, Photron) with a camera lens of 85mm length f/2.8 (PC Micro-Nikkor 85mm f/2.8D, Nikon). The laser sheet was introduced from the laser generator placed beneath the wind tunnel floor through an acrylic plate to the measurement target area (56mm×70mm) in a streamwise and wall normal plane. The position of the laser sheet was shown in figure 4-2 and the camera was placed out of the wind tunnel at a distance of 470mm from the light sheet in spanwise direction. Although the author revealed that mask correlation method (MCM) contributes to mitigate peak locking problem in Chapter 3, MCM was not used in PIV measurement in this chapter for the reason that the PIV experiment was conducted before peak locking problem is recognized as an unavoidable problem.

Local displacement of a particle image was determined by a correlation coefficient of particle brightness pattern calculated at a frequency of 500Hz by the FFT-based cross-correlation method developed by Willert and Gharid (1990), and it is transformed into the instantaneous wind velocity. The correlation coefficient is calculated by the following process: an integration area is selected on a PIV photograph and another integration area is defined at the same location of contiguous PIV photograph, and then a correlation coefficient of the particle brightness pattern is calculated. A sub pixel scale analysis is subsequently performed to determine the displacement of particles in smaller scale. Each adjacent integration area overlapped by 50% region, in other words, the center of an integration area is located on the side of the next integration area as shown in figure 4-3, thus, wind vectors are obtained each 8 pixel.

After all wind vectors are obtained, data validation is performed for a post processing to remove erroneous wind vectors using two types of linear filters: dynamic mean filter

and median filter. Dynamic mean filter is used to identify the erroneous wind vector which has abnormally large absolute value compared to vectors surrounding the target vector, and median filter is employed to determine and remove erroneous vector which is not consistent with the general tendency of surrounding vectors (Westerweel 1994).

After erroneous vectors are removed, the alternative vectors are calculated based on the second largest peaks of correlation coefficients in each integration areas and validated by the same method. If these vectors are confirmed to be invalid or an adequate secondary peak of correlation coefficient does not exist, interpolated vectors are calculated based on surrounding vectors. Since ratio of the number of interpolated vectors to that of valid vectors was only 3.44%, thus the influence of interpolation seemed to be not so large.

Prior to the main analysis, the author validated our experimental data based on the spatial distribution of turbulent statistics and time series fluctuation of streamwise and vertical wind component, and determined the target area for the analysis in which noise effect is relatively small and experimental data seems accurate (Figure 4-4).

4.3 Experimental results

4.3.1 Streamwise velocity

Several studies suggest that turbulent flow properties around block arrays with high aspect ratio are similar to those appear in vegetation canopy, for example, Huq et al. (2007) performed a water tunnel experiment using two types of blocks with aspect ratio 1.0 and 3.3 as simplified models of the midtowns of Los Angeles and New York City. They indicated the similarity of vertical profiles of streamwise velocity between vegetation canopy and urban-like canopy consists of high aspect ratio blocks. Furthermore, Moriwaki et al. (2009) conducted a series of field measurement in a rice

paddy field and two types of block arrays with aspect ratio 1.0 and 3.3 ($\lambda_p = 25\%$) under almost stable condition and showed the difference and similarity of turbulent statistics and momentum transfer among these three canopies. In this section, the several turbulent statistics obtained in present experiment are compared with a variety of the previous data for vegetation canopy.

Figure 4-5(a) shows vertical profiles of U/U_H (U_H is the time averaged streamwise wind velocity at the canopy height) measured at the center of the measurement area (dotted line shown in figure 4-4). The turbulent statistics presented in Raupach et al. (1996), which are based on field observations and wind tunnel experiments for various types of vegetation canopy and plant like models, are also included in the graphs. The mean wind profile of this experiment shows good agreement with those for vegetation canopy. U/U_H between a height from $0.3H$ to $0.7H$ obtained by our experiment is in a range from 0.46 to 0.50 and almost constant with height; this tendency coincides in

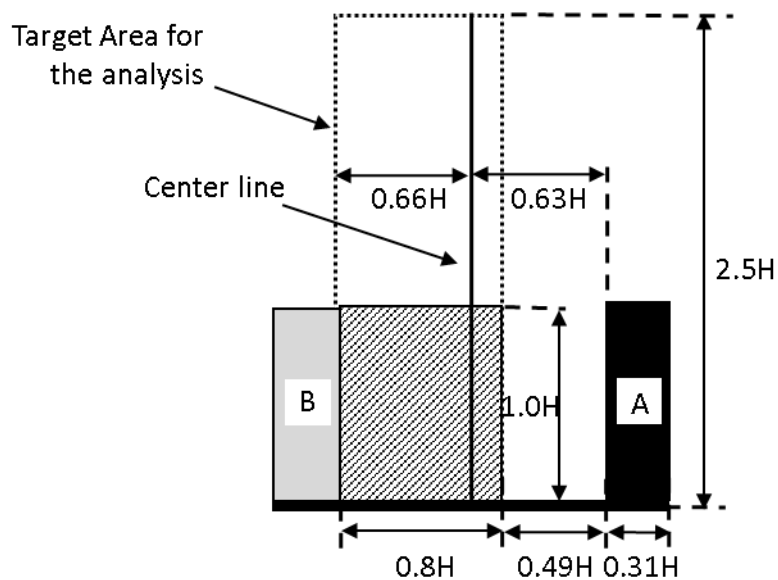


Figure 4-4 Dotted square: experimental data has high accuracy,
solid line: center of measurement area.

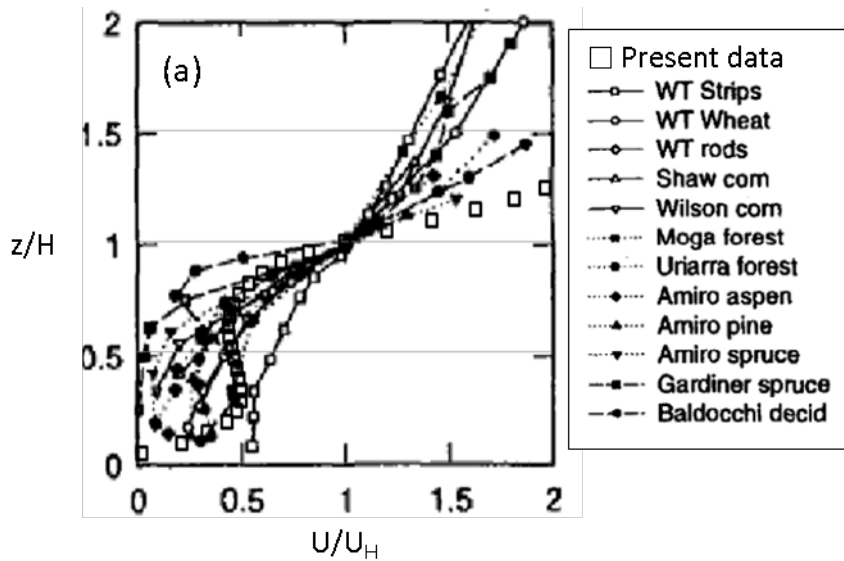


Figure 4-5 Comparison of vertical profiles of streamwise wind velocity and turbulent statistics in various types of vegetation canopies and present study. All profiles of present experiment are measured at the center of the measurement area (figure4-4). U_H is time averaged streamwise velocity measured at canopy roof height and u_* is friction velocity. (a) U/U_H , (b) σ_u/u_* , (c) σ_w/u_* , (d) Sk_u , (e) Sk_w , (f) $-\overline{u'w'}/u_*^2$, (g) $-\overline{u'w'}/\sigma_u\sigma_w$

particular with that of Uriarra forest (Denmead and Bradley 1987). In addition to that, the mean wind profiles of both the present experiment and Uriarra forest exhibit two inflection points within the canopy. Similar inflection points within the canopy are also founded in the data of LES simulation (Kanda et al (2004), a square array of cubical obstacles, $\lambda_p = 25\%$) and field experiment (Baldocchi and Meyers 1988, a forest consists of mixing species stand of predominantly oak and hickory trees, the average height is 23m and frontal area index (ratio of projected area to roof area) $\lambda_f = 2.5$).

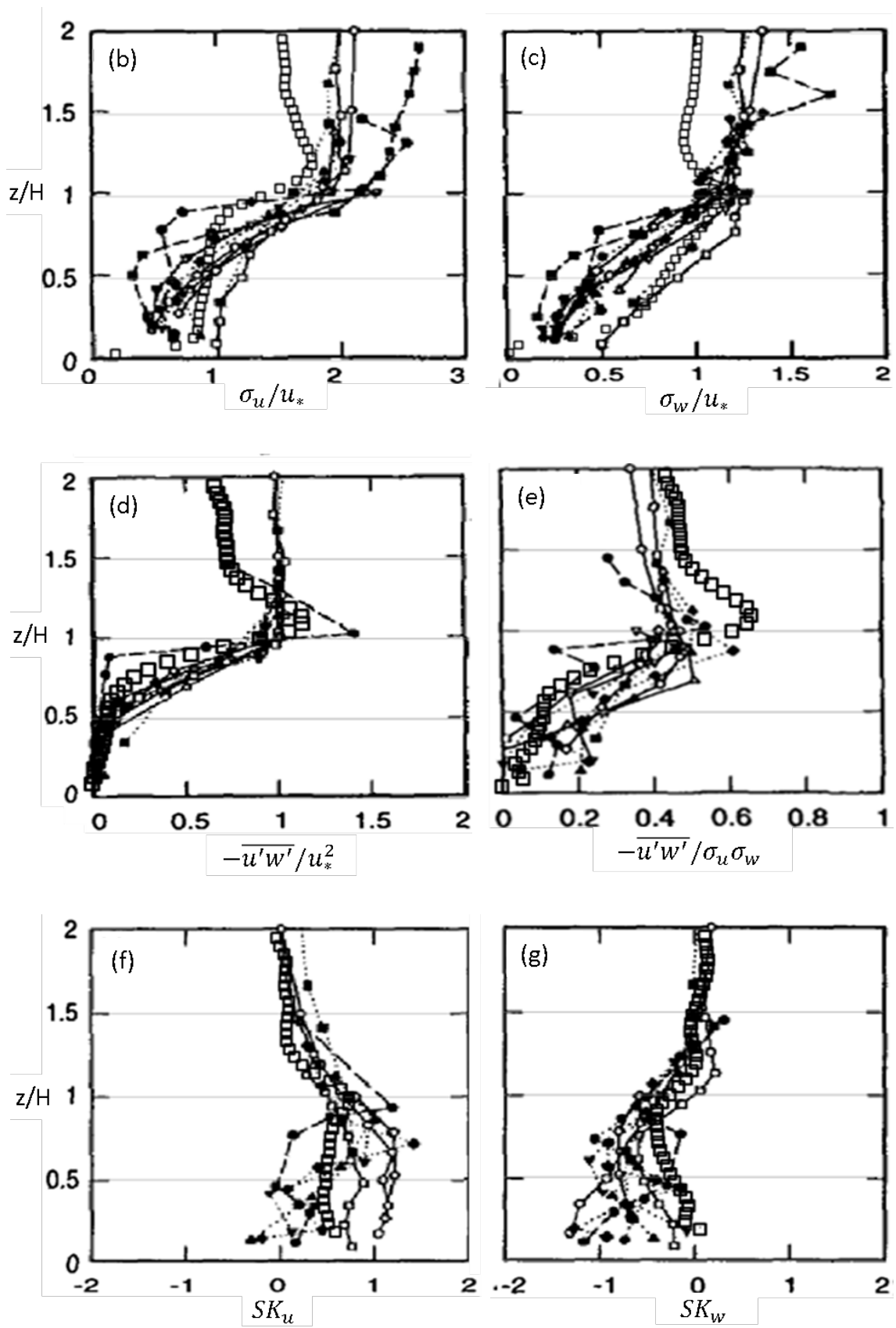
On the other hand, although wind profile of this study are in correspondence with those of Amiro Spruce (Amiro 1990) and Baldocchi decid (Baldocchi and Meyers 1988), the difference of wind profiles among each experiment become large above canopy height, and wind profile of our experiment shows relatively large value compared to those in

vegetation canopies. Raupach et al. (1996) suggested such difference is attributed to the difference of canopy morphology characterized by leaf area density (LAD). Although the block array used in this study consists of slender blocks with relatively high aspect ratio compared to ordinary cube arrays and the shape of them is relatively similar to those of tree trunk, the morphology differs from those of vegetation near the canopy top, hence it is thought that difference of wind profiles appeared only above the canopy top.

4.3.2 Turbulent statistics

Figure 4-5(b) and (c) show standard deviation of streamwise and vertical wind velocity normalized by friction velocity (u_*) which is defined by a peak value of spatial averaged Reynolds stress ($z/H=1.14$) with the data from Raupach et al. (1996). The profiles for two components obtained in the present experiment within the canopy ranges in the scatter of the data of vegetation canopy, in contrast, they are little smaller than those of vegetation canopies above canopy height.

Same tendency is observed in figure 4-5(d) and (e), which show vertical profile of Reynolds stress normalized by friction velocity ($-\overline{u'w'}/u_*^2$) and correlation coefficient of streamwise and vertical velocity component ($-\overline{u'w'}/\sigma_u\sigma_w$). The value of the Reynolds stress in this research is little smaller above canopy but well accorded with the others in plant canopies under the height of $z/H=1$. On the other hand, the values of $-\overline{u'w'}/\sigma_u\sigma_w$ are relatively similar except for the layer from $z/H=1$ to $z/H=1.4$, and almost constant above $z/H=1.4$. The constant value of $-\overline{u'w'}/\sigma_u\sigma_w$ above canopy height is observed in previous study (e.g.; Macdonald et al. 2002). Raupack et al. (1996) defined flow properties in surface, mixing and canopy layer by investigating turbulent statistics and suggested that the typical value of $-\overline{u'w'}/\sigma_u\sigma_w$ in mixing layer is -0.44, meanwhile, the



value of $-\overline{u'w'}/\sigma_u\sigma_w$ in present study above $z/H=1.4$ fluctuates between 0.430 to 0.485 (figure 4-5(e) shows inverse signed value). This fact indicates the similarity of flow properties between vegetation canopy and urban like models with high rise building models.

By contrast, skewness of both two wind components presented in figure 4-5(f) and (g) correspond well with the profile of them in vegetation canopies for both within and above the canopy. It is noteworthy that skewness of streamwise velocity is positive within the canopy and that of vertical component is negative between $z/H=0.5$ to 1.1. This tendency is associated with the transition of a mechanism of momentum transfer which is strongly related to intermittent flow patterns in canopy layer as described below.

Quadrant technique was applied for the data of the target area shown in figure 4-4, and the contribution of each quadrant for momentum transfer was calculated by the following equation.

$$\langle \overline{S_j} \rangle = \left\langle \frac{\sum_i^N (u_i' w_i')_j}{N \times u_*^2} \right\rangle \quad (j = 1,2,3,4) \quad 4-1$$

Here, $\langle \rangle$ represents a horizontal average in the target area and N means the number of time-series data (=21840).

Figure 4-6 shows the vertical profile of the contribution of each flow mode for momentum transfer and the results of Kanda et al. (2004) based on LES of a cube array with $\lambda_p = 25\%$ are also included. The contribution of S2 ($u'<0, w'>0$) mode and S4 ($u'>0, w'<0$) mode become large rapidly above $z/H=0.5$. In addition, S4 mode have a larger contribution than S2 mode within and a little above the canopy, however, the magnitude relationship of the influence of these two modes become reverse and the effect of S2 mode is slightly larger for momentum transfer above $z/H=1.25$. This tendency is

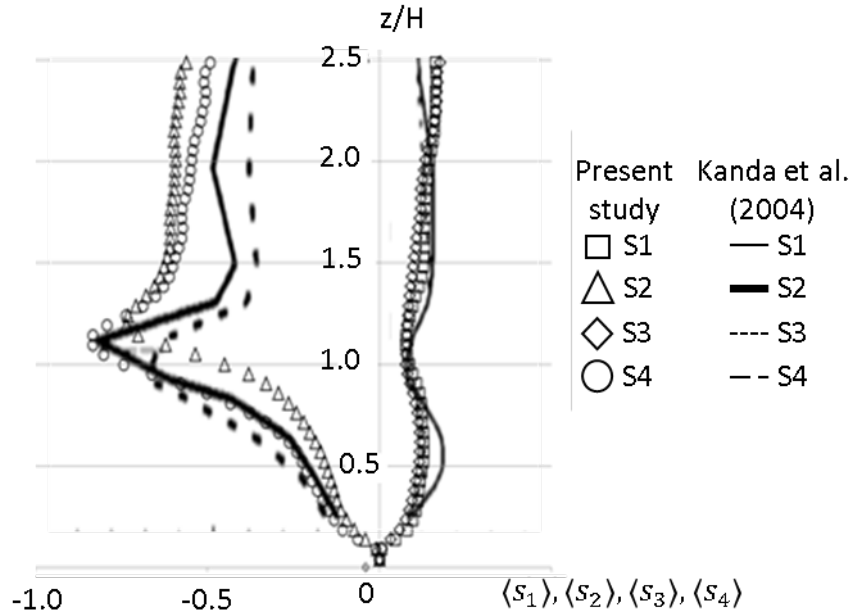


Figure 4-6 Special averaged profile of contribution for the momentum transfer by four quadrants. Square, triangle, diamond and circle plots are from this study; thin, solid, dotted and broken line are from Kanda et al. (2004)

consisted with the vertical distribution of skewness shown in figure 4-5(f) and (g). The transition of the contribution ratio of S2 mode and S4 mode is also confirmed in a cube array (Kanda et al. (2004)) and vegetation canopy (e.g. Finnigan et al. 2009), thus this tendency is considered to be universal regardless of shape of roughness elements.

As figure 4-5(b)-(g) shows, although standard deviation, Reynolds stress and $-\overline{u'w'}/\sigma_u\sigma_w$ above the canopy height in the present experiment differ from those in vegetation canopy, all turbulent statistics presented here fall within the range of scattering of vegetation canopy under a height of $z/H=1.0$. This result suggests that the flow characteristics characterized by the basic turbulent statistics in high aspect ratio block arrays is close to those in vegetation canopy under the canopy height.

4.3.3 Typical instantaneous upward flow fields

Several previous studies imply the possibility that some typical instantaneous flow patterns have a large contribution for momentum transfer between within and above canopy, for example, Takimoto (2011) performed a field measurement and a wind tunnel experiment using PIV and presented instantaneous wind vectors of strong upward flow happens almost entire the canopy layer and just above the canopy, and they call this flow pattern as “Flushing”. Similar type flow patterns were also observed in numerical study; Inagaki (2011) performed LES of airflow over a cubical array assuming atmospheric boundary layer (ABL) in daytime and demonstrated that temperature within the canopy become higher at the moment in which a flushing event occurs and upward flow occupies whole of canopy. Under the circumstances, the author investigated the features of instantaneous flow fields under the condition that the flow satisfies one of the following criteria, A) upward mode: $u' < 0$ and $w' > 0$ are fulfilled more than 60% of shaded square, B) downward mode: velocity of more than 60% of the area is $u' > 0$ and $w' < 0$, and extracted six typical flow patterns.

Figure 4-7(a) and (b) show vector maps of typical upward mode which satisfy the condition A. In figure 4-7(a), obliquely upward flow covers entire the canopy layer, in contrast, the flow over the canopy is relatively smooth and parallel to the roof and the boundary of these two flow results in meandering flow near the roof (red ellipse). Wind above the canopy is prevented from penetrating into the canopy by upward flow within the canopy and glides over canopy like skimming flow (Oke, 1988). In contrast, figure 4-7(b) illustrates not only within the canopy but also above the canopy up to a height of $z/H=2.2$ are occupied by strong obliquely upward mode with about 45 degree angle. This type of flow pattern moves downward with time maintaining its intensity.

Figure 4-8(a) and (b) present two instantaneous flow fields which also satisfy the

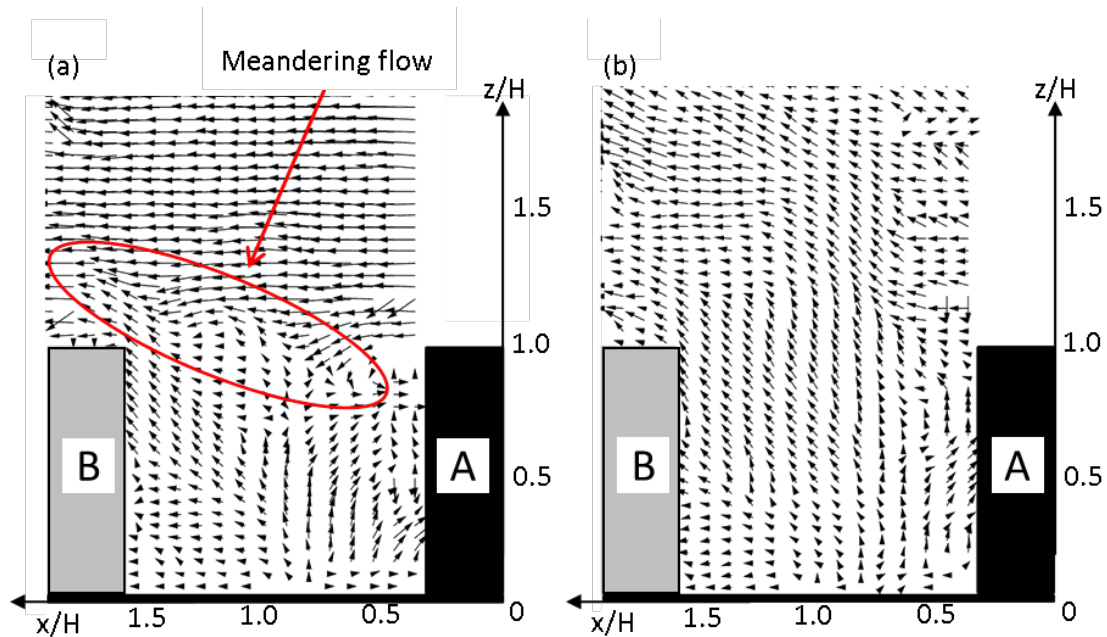


Figure 4-7 Vector maps of two characteristic flow patterns. Strong upward wind occur within the canopy in both instantaneous flow fields and the condition A is satisfied ($u' < 0$, $w' > 0$ are fulfilled more than 60% of measurement points in shaded square in figure 4-4).

condition A, and the one illustrated in figure 4-8(b) was captured 0.02 seconds (twenty frames) prior to figure 4-8(a). These two flow patterns depict intermediate behavior of the two flow patterns presented in figure 4-7, namely, strong obliquely upward flow within the canopy extends to outside of the canopy but the top of that flow remains at $z/H=1.4$. Furthermore, parabolic flows are observed inside the red circles in both figures and streamwise flows from upper stream circumvent that hyperbolic streamline. These types of flow patterns are obviously similar to the flushing mode Takimoto et al. (2011) presented. They indicated the mean duration time and frequency of flushing mode are $0.23T$ and $1/9.87T$, here T is the time scale defined by the building height and friction velocity which is defined by Reynolds stress at the twice of building height ($T=H/u_{*(2H)}$). The normalized duration time and frequency of the intermittent flow events in present

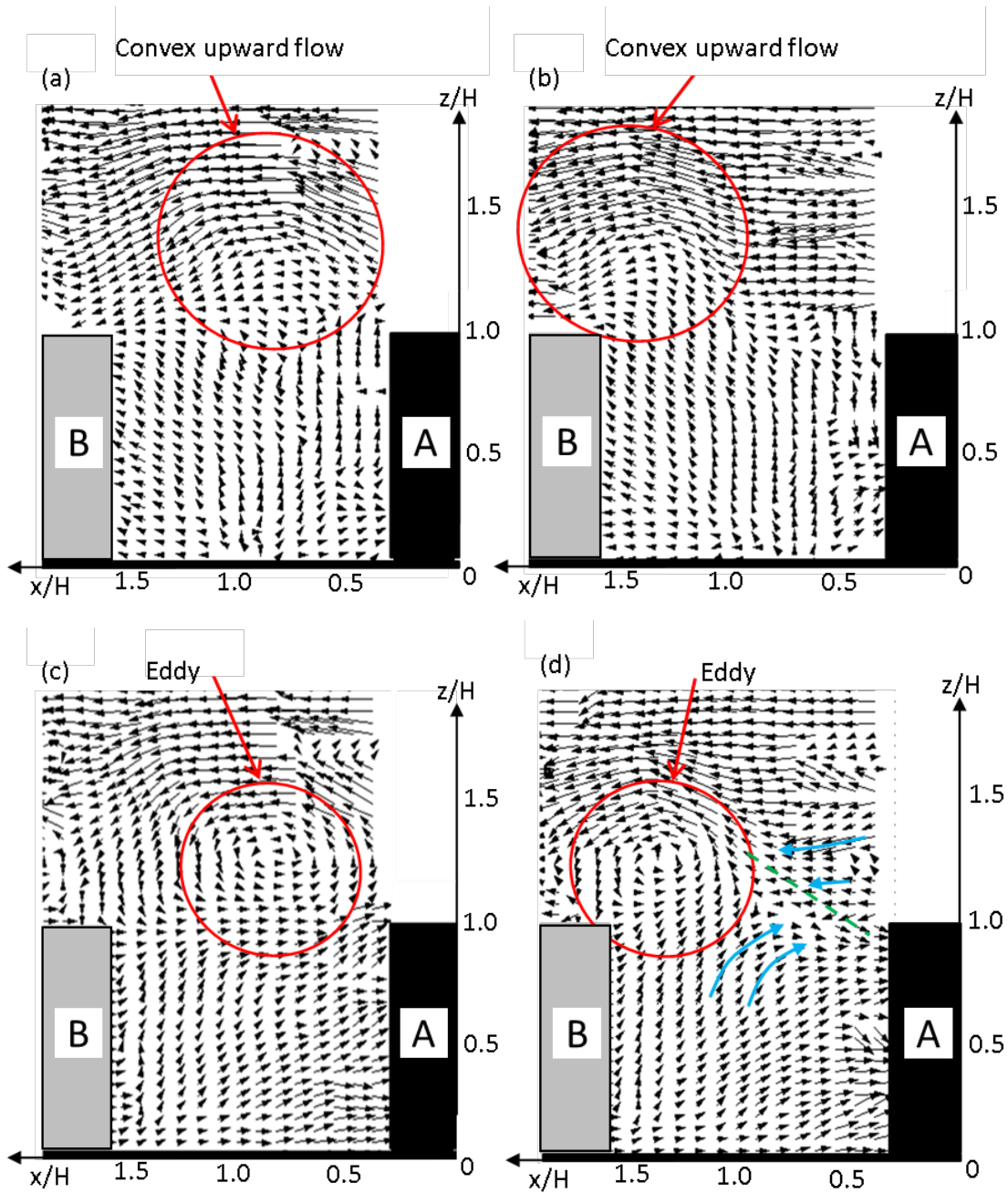


Figure 4-8(a) and (b) Instantaneous flow fields captured at 26.760s and 26.780s after experiment began, both two satisfied condition A. (c) and (d) vector views produced by subtracting convective wind speed ($U_c/U_{1.25H}=0.47$) from figure 4-7 (a) and (b) according to the method Adrian et al . (2000) developed.

study are $0.316T$ and $1/8.22T$, and approximately consistent with the results of Takimoto et al. (2011).

Next, vortices associated with coherent structures in figure 4-8(a) and (b) are extracted by using a method Adrian et al. (2000) used. Figure 4-8(c) and (d) show the vector map of $(u - U_c, w)$ produced by subtracting convection velocity, $U_c/U_{1.25H} = 0.47$, from instantaneous flow fields presented in figure 4-8(a) and (b) (determination of U_c is discussed in Appendix 4-1). A large eddy is observed above the canopy in both figure 4-8(c) and (d), and the location of the eddy corresponds to the positions of the convex upward flow in figure 4-8(a) and (b) (All snapshots during 0.02 second show agreement of locations of the convex upward flow and these eddies). It should be noted that the flow structure around the eddy in figure 4-8(d) is closed to that around a hairpin vortex consist of hairpin packet structures (Adrian et al. 2000, figure 4-9). A strong upward flow arises diagonally downward of the vortex head, and it impinges on a downward flow in upstream of the vortex head, forming a shear layer. Furthermore, the stream lines drawn by vectors suggest that the effect of the eddy reaches to a height of $z/H=0.35$ and air within the canopy is plucked up to outside the canopy. Although it is difficult to affirm that the eddy

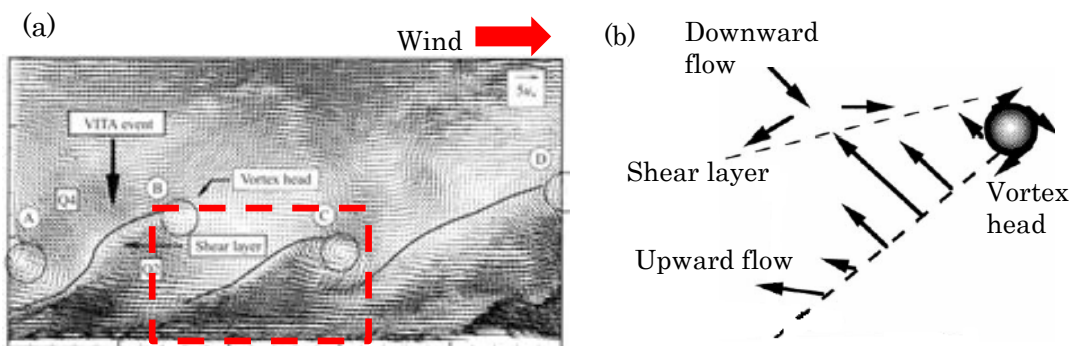


Figure 4-9 (a) Vertical cross section of hairpin packet structure, (b) Flow structure around a hairpin vortex (Adrian et al. 2000)

in figure 4-8(d) is a part of a hairpin vortex because of the small measurement area, this result might indicate a direct correlation between canopy flow and turbulent organized structure above the canopy.

4.3.4 Typical instantaneous downward flow fields

Figure 4-10(a) and (b) show the two typical instantaneous flow fields which satisfy the condition B where strong downward wind dominates above the canopy in both case and it penetrates into the canopy. Although the flow fields above the canopy are almost same, the flow regimes within the canopy are significantly different.

In figure 4-10(a), the slantwise downward flow comes from the upper layer separates

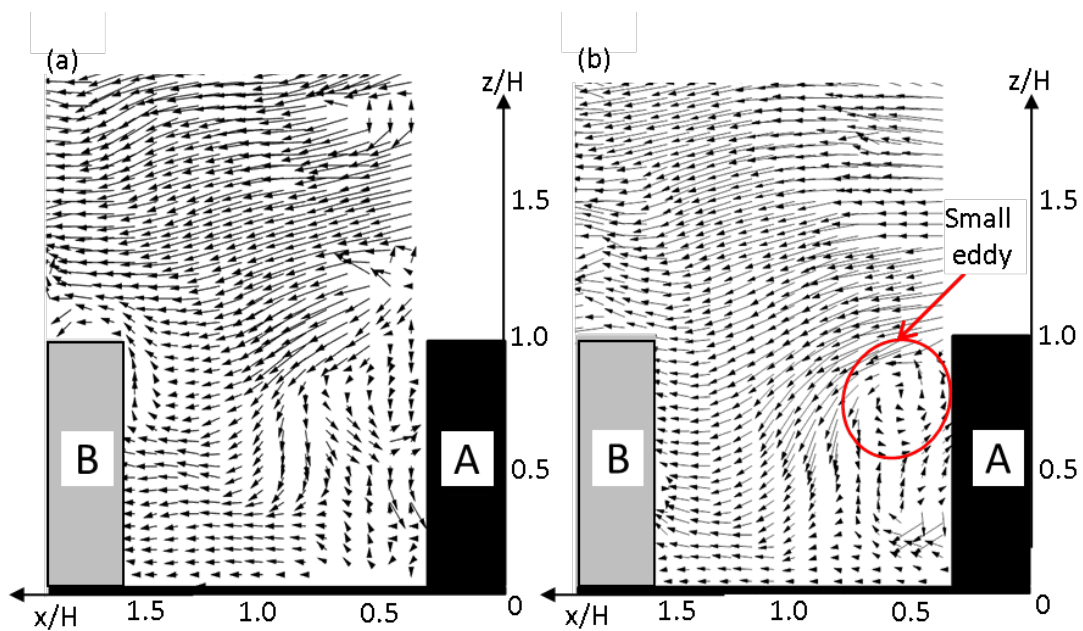


Figure 4-10(a) and (b) Vector maps of two characteristic flow patterns. Strong downward wind occurs above the canopy and it penetrates into canopy. The threshold B is satisfied in both flow field ($u' > 0$, $w' < 0$ are fulfilled more than 60% of measurement points in shaded square in figure 4-4).

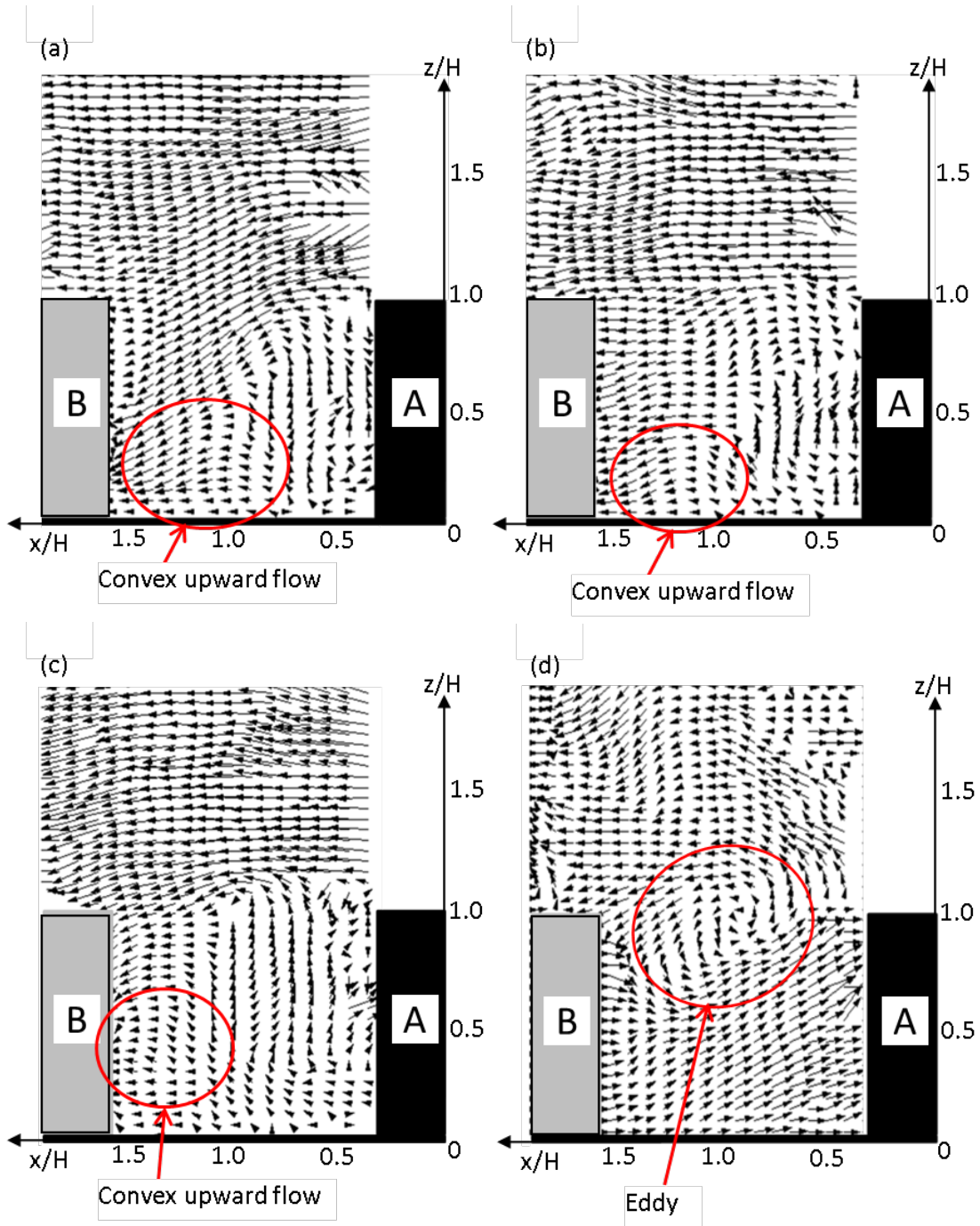


Figure 4-11(a), (b) and (c) Instantaneous flow patterns at the moment when strong bent flow observed at the canopy roof height. Figure 4-9(d) Vector views produced by subtracting convective wind speed ($U_c/U_{1H} = 1.5$) from figure 4-9(a).

into three parts. The one near the obstacle A changes its direction, resulting in a small wake vortex around a corner of block A. On the other hand, the one located at $x/H=0.9$ descends almost vertically and the other penetrates downward obliquely. In contrast, in figure 4-10(b), the strong downward flow from above the canopy is not separated into three parts and a small eddy is observed just behind the obstacle A, which stays in the same position and gradually collapse with the decrease of intensity of the downward flow. This small eddy is supposed to be generated by the strong shear stress due to the strong downward flow come from above the canopy and low speed stream near the obstacle A.

Figure 4-11(a), (b) and (c) show other typical instantaneous flow fields which fulfill the condition B. The most notable feature is the stream near the obstacle A: which bends sharply near the roof height. Specifically, small upward flow from the bottom of the canopy reaches to the canopy roof height and is affected by the strong downward flow from above the canopy, and finally incorporates into downward wind. In addition to this bent shape flow, small parabolic flows observed near the bottom of the canopy (red circles) in figure 4-11(a), (b) and (c). Although the size, intensity, and position of these small convex upward flows are not same, similar small hilly streams can be observed not only these three flow fields but also almost all of this type flow fields happen at different times.

Figure 4-11(d) shows the large eddy at the canopy roof height advected by convection velocity, $U_c/U_H=1.5$, in flow field figure 4-11(c) presented. Similar to figure 4-8, the location of the eddy completely corresponds to the position of the bent flow, and furthermore, the location of inverse flow which consists of a part of this eddy is in according with the gap between the bent flow and small hilly flow. Although the size of the eddy is little smaller than that shown in figure 4-8(c) and (d), the eddy have a large

influence on flow field and determine the flow structure within the canopy.

4.4 Conclusion

In the present study, PIV measurement on the air flow around an urban like canopy consists of blocks with high aspect ratio assuming an array of high-rise buildings revealed typical instantaneous flow patterns associated with turbulent organized structure (TOS) as follows.

First notable point is that the instantaneous flow field for upward mode presented in figure 4-8(a) is quite similar to the typical instantaneous flow pattern called flushing (Takimoto et al. 2011, Inagaki et al. 2011) in both qualitative and quantitative aspects. Although transport phenomena of heat and pollutant materials are out of scope of this study, previous studies suggested that flushing mode appears around low-aspect building models has a large influence on the heat and pollutant removal (e.g. Michioka et al. 2010), hence, it might be considered that the flow field presented in present study also strongly relates to the heat and air pollutant condition around high rise buildings.

Second remarkable result is five typical instantaneous flow patterns which enhance the mixing of the air between canopy layer and roughness sub layer. Large scale downward flow presented in previous studies is also observed in present study, and moreover, it divided into three typical patterns based on flow field within the canopy. In particular, the flow field when strong bent flow occurs (figure 4-11(a), (b) and (c)) were quite complicated, specifically, the air once uprises from the bottom of the canopy to the roof height and then descends into the canopy with strong downward wind from above the canopy. To understand the influence of this flow field on the scalar transfer, further investigation is needed, nevertheless it might be predicted that temperature and scalar

concentration within a canopy is significantly related with such a specific flow field.

Adrian et al. (2000) presented a stream of a series of eddies as an indication of cross section surface of hairpin packet structure in surface layer over a smooth wall. Although it is not definitive that the eddies shown in the present study are parts of hairpin packet structure because only one eddy was observed in each vector views (figure 4-8(c) and (d)) due to the small measurement area, the condition of flow field around these eddies are well correspond to that they defined as the feature of the hairpin packet structure. It is interesting if the large eddy above the canopy associated with a hair-pin packet structure result in a certain type of instantaneous flow fields within the canopy. Future work will aim to acquire instantaneous flow field with wider measurement area to corroborate the present conjecture.

References

- Adrian, R. J., Meinhart, C. D. and Tomkins, C.D. (2000) Vortex organization in the outer region of the turbulent boundary layer, *Journal of Fluid Mechanics*, vol.422, pp. 1-54.
- Amiro, B. D. (1990) Comparison of turbulence statistics within three boreal forest canopies, *Boundary-Layer Meteorology*, vol.51, pp.99-121.
- Baldocchi, D. D. and Meyers, T. P. (1988) Turbulence structure in a deciduous forest, *Boundary-Layer Meteorology*, vol.43, pp.345-364.
- Coceal, O., Thomas, T. G. Castro, I. P. and Belcher, S. E. (2006) Mean flow and turbulent statistics over groups of urban-like cubical obstacles, *Boundary-Layer Meteorology*, vol. 121, pp.491-519.
- Denmead, O. T. and Bradley, E. F. (1987) On scalar transport in plant canopies, *Irrigation Science*, vol.8, pp.131-149.
- Finnigan, J. J., Shaw, R. H. and Patton, E. G. (2009) Turbulent structure above a vegetation canopy, *Journal of fluid mechanics*, vol.637, pp.387-424.
- Grimmond, C. S. B. and Oke, T. R. (1998) Aerodynamic properties of urban areas derived from analysis of surface form, *Journal of Applied Meteorology*, vol.38, pp.1262-1292.
- Hagishima, A., Ikegaya, N., Tanimoto, J. and Yamaguchi, M. (2012) Drag coefficients of staggered arrays with various block aspect ratio, *Proc. 8th International Conference on Urban Climates (ICUC8)*, IAUC, Ireland.
- Huq, P., White, L.A., Carrillo, A., Redondo, J., Dharmavaram, S. and Hanna, S. R. (2007) The shear layer above and in urban canopies, *Journal of Applied Meteorology and Climatology*, AMS, vol.46, pp.368-376.
- Inagaki, A., Castillo, M. L., Yamashita, Y. Kanda, M. and Takimoto, H. (2011) Large-eddy simulation of coherent flow structures within a cubical canopy, *Boundary-Layer Meteorology*, vol.142, pp.207-222.
- Kanda, M., Moriwaki, R. and Kasamatsu, F. (2004) Large-eddy simulation of turbulent

- organized structures within and above explicitly resolved cube arrays, *Boundary-Layer Meteorology*, vol.112, pp.343-368.
- Kanda, M. (2006) Large eddy simulations of the effects of surface geometry of building arrays on turbulent organized structure, *Boundary-Layer Meteorology*, vol.118, pp.151-168.
- Li, X., Liu, C. and Leung, D. Y. C. (2008) Large-eddy simulation of flow and pollutant dispersion in high- aspect-ratio urban street canyons with wall model, *Boundary-Layer Meteorology*, vol.129, pp.249-268.
- Macdonald, R. W., Carter, S. S. and Slawson, P. R. (2002) Physical modelling of urban roughness using arrays of regular roughness elements, *Water, Air and Soil Pollution: Focus*, vol.2, pp.541-554
- Michioka, T., Sato, A., Takimoto, H. and Kanda, M. (2011) Large-eddy simulation for the mechanism of pollutant removal from a two-dimensional street canyon, *Boundary-Layer Meteorology*, vol.138, pp.195-213
- Moriwaki, R., Fujimori, Y. and Aoki, S. (2009) Comparison of turbulence statistics above outdoor urban scale model and rice paddy, *Proc.7th International Conference on Urban Climate (ICUC-7)*, IAUC, Japan.
- Oke, T. R. (1988) Street design and urban canopy layer climate, *Energy and Buildings*, vol.11, pp.103-113
- Pokrajac, D., Campbell, L., Nikora, V., Manes, C. and McEwan, L. (2007) Quadrant analysis of persistent spatial velocity perturbations over square-bar roughness, *Experiments in Fluids*, Springer-Verlag, vol.42, pp.413-423
- Raupach, M. R., Finnigan, J. J. and Brunet, Y. (1996) Coherent eddies and turbulence in vegetation canopies: the mixing-layer analogy, *Boundary-Layer Meteorology*, vol.78, pp.351-382
- Reynolds, R. and Castro, I. (2008) Measurements in an urban-type boundary layer, *Experimental in Fluids*, vol.45, pp.141-156

- Takimoto, H., Sato, A., Barlow, J. F., Moriwaki, R., Inagaki, A., Onomura, S. and Kanada, M. (2011) Particle image velocimetry measurements of turbulent flow within outdoor and indoor urban scale models and flushing motions in urban canopy layers, *Boundary-Layer Meteorology*, vol.140, pp. 295-314
- Westerweel, J. (1994) Efficient detection of spurious vectors in particle image velocimetry data, *Experiments in Fluids*, vol.16, pp.236-247
- Willert, C. E. and Gharib, M. (1990) Digital particle image velocimetry, *Experiments in Fluids*, vol.10, pp.181-193

Chapter V

Study on the effect of ancillary structures on turbulent flow fields

5.1 Introduction

The turbulent flow nature around buildings has attracted much interest in both urban climatology and wind engineering, and a vast number of experiments and numerical simulations have been conducted for decades in order to reveal the relation between turbulent flow fields and urban geometries.

As it was explained in Chapter 4, The classification of three flow regimes (skimming flow, wake interference, and skimming flow) in an urban canyon in terms of the canyon aspect ratio (ratio of the street width to canyon roof height) is one of significant phenomenological description (Oke 1988). This fundamental classification of mean flow structures in urban canyons has been used in following research. For example, Hunter et al. (1991) performed Reynolds averaged Navier-Stokes (RANS) simulations on flow fields around 2D street canyons under four conditions of canyon aspect ratio (1, 3, 5, and 7), and presented typical features of each flow regime. Similarly, Leonaldi et al. (2003) performed direct numerical simulations (DNS) for 2D street canyons with canyon aspect ratio from 0.33 to 19, and quantitatively evaluated the size of recirculation flows, locations of flow reattachment on the bottom of a canyon, and the size of a small vortex in front of the leeward building. Furthermore, more complicated flow structures around 3D roughness models have been also investigated by numerical simulations (e.g. Kanda et al. 2004, Coceal et al. 2006, Santiago et al. 2007) and wind tunnel experiments (e.g. Uehara et al. 2007, Reynolds and Castro 2008). DNS conducted by Coceal et al. (2006) provides highly accurate data of temporally averaged flow fields, spatial distributions of

turbulent statistics, and characteristics unsteady turbulent motions for three cubical arrays (staggered, aligned and square array) with $\lambda_p = 25\%$ (λ_p is building plan area index, the ratio of the plan area occupied by obstacles to the total floor area).

Meanwhile, most of the past studies simplified real urban geometries as highly idealized block arrays, however, in general, real urban surfaces include diverse and complicated topography derived from secondary roughness such as balconies and penthouses. Therefore, it is uncertain to what extent the airflow nature of idealized block arrays can be treated as prototypes of flow fields in real urban conditions. For example, Kastner and plate (1999) conducted wind tunnel experiments using 2D street canyons with 6 different roof shapes, and presumed the variation of mean flow structures within the street canyons based on differences of the scalar concentration. The influence of complex building topology on temporally averaged flow fields are presented more detail by recent studies. For example, Huang et al. (2009) carried out RANS simulation on 2D street canyons which consist of roughness models with flat and inclined roofs. They classified roughness conditions into three groups (step-down, even, step-up) based on the relative height of the roofs of windward and leeward buildings, and demonstrated characteristic features of temporally averaged flow fields in each roughness group. Similarly, Takano and Moonen (2013) presented how mean flow structures within 2D street canyons vary with approaching wind directions and building roof shapes by RANS simulations. RANS simulations conducted by Mohamad et al. (2014) demonstrated the influence of the flat eaves extending from building roofs towards street canyons on the temporally averaged flow fields. They revealed that the structures of temporally averaged flow fields are much different from the fundamental flow regimes presented by Oke (1988), and they indicated the wind induced natural ventilation rate inside a building

significantly varies with the length of eaves. The effects of complex surface topology on unsteady turbulent flow fields are also examined by a few pioneering studies. The particle image velocimetry (PIV) experiment conducted by Kellnerova et al. (2012) and large eddy simulation (LES) by Takano et al. (2015) investigated the influence of building roof shapes on unsteady turbulent motions around 2D street canyons. They applied proper orthogonal decomposition (POD) analysis to instantaneous flow fields and extracted dominant turbulent modes based on turbulent kinetic energy. However, the existing data of the influence of complex urban topology on unsteady turbulent flow fields are still limited, and the holistic features have not been clarified.

Under these circumstances, in this chapter, PIV experiment is conducted in order to investigate how turbulent flow fields around 2D street canyon are changed by the effect of flat eaves overhang the street canyon. By using PIV technique, detailed structures of temporally averaged flow fields, spatial distributions of turbulent statistics, turbulent coherent structures, and unsteady flow motions around the canopy are examined.

In addition, this chapter investigates how the variation of turbulent flow fields around the roughness affects spatially and temporally averaged indications of urban air conditions, namely the urban ventilation rates and the bulk drag force (figure 5-1). Urban ventilation rate is one of the most important factors which is relevant to heat and scalar emission from an urban canopy, thus, numerous number of research has been conducted. For example, Uehara et al. (2007) examined the optimal arrangement of roadside buildings which promotes air ventilation in a street canyon by PIV experiment. The optimal building arrangement in their experiment was the zigzag array of tall and short buildings. In this case, ascending flows and descending flows, which arise along windward and leeward wall of tall buildings respectively, are connected by spanwise flow

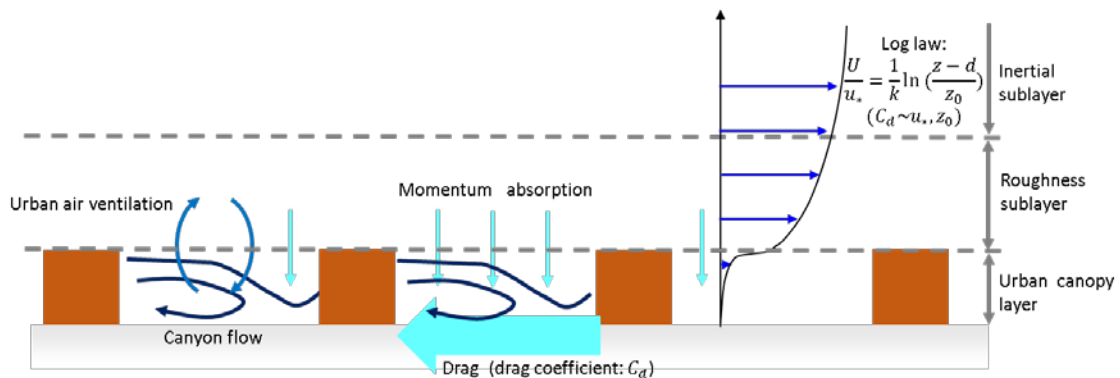


Figure 5-1 Canyon flow, air ventilation, and drag force

near the bottom of the canyon, forming three dimensional flow structures and thus air ventilation is stimulated. Simoens and Wallace (2008) demonstrated the result of simultaneous measurements of flow fields and scalar concentrations in a wind tunnel using 2D urban street canyons with three canyon aspect ratio (1, 4, and 8), and analyzed scalar transport process associated with temporally averaged flow field structures. The above two studies focused on temporally averaged air ventilation mechanism, while several recent studies have investigated the contribution of unsteady turbulent motions (e.g. Liu et al. 2004, Liu et al. 2005, Li et al. 2008). LES conducted by Inagaki et al. (2011), Michioka et al. (2011), and Michioka et al. (2014) demonstrated noteworthy curious results on the relation between turbulent coherent structures and scalar/heat emissions from urban canyons. Namely, low speed upward flow arise throughout an urban canopy and large scalar emission is caused at the moment in which low speed streak-like structures passed just above the urban canopy. This trend is observed in various types of roughness conditions including 2D street canyons and cubic arrays, indicating importance of coherent structures on urban air ventilation. In the present study, air ventilation rate can be directly calculated from vertical velocity component at the canyon roof level measured by PIV experiments, thus, the relationship between turbulent flow fields and

urban air ventilation mechanisms can be investigated in detail.

Meanwhile, in regards to bulk drag force, a wind tunnel experiment performed by Maruyama (1991) provides sectional drag coefficients (C_d) for both staggered and square cubic arrays under the various conditions of λ_p . He figured out C_d increases with λ_p in sparse canyons, while it begins to decline after maximum peaks appeared at $\lambda_p \doteq 0.1$ (square array) and $\lambda_p \doteq 0.2$ (staggered array), and concluded this tendency of C_d with the variation of λ_p is explained by the transition of three fundamental flow regimes within canyons as presented by Oke (1998). Following to the experiment by Maruyama (1991), experiments and numerical simulations on C_d have been conducted including more various urban geometrical factors (e.g. Hagishima et al. 2007, Zaki et al. 2010, Hagishima et al. 2012, Kanda et al. 2013, Santiago et al. 2013). Hagishima et al. (2012) measured C_d of staggered uniform rectangular block arrays with different slenderness of blocks, and revealed that the maximum peak of C_d appears in low λ_p and the value of maximum peak of C_d increases under the condition of high roughness aspect ratio. A possible reason is that slender blocks are more streamlined than short and thick blocks, and the air flow can pass around the side of blocks, resulting in making it difficult to form skimming flow in canyons. Santiago et al. (2013) examined the drag and lift force of cubic aligned array under the condition that the mean wind direction is not orthogonal to block faces by RANS simulations. They analyzed variations of the magnitude of the forces and their directions in each case associated with the time averaged flow structures in canyons, which drastically change depending on mean flow direction. From the results of RANS simulation by Mohamad et al. (2014), in this study, it is presumed that temporally averaged flow patterns in street canyons are highly different from well-known three flow regimes by the effect of eaves. Hence, drag coefficient might also show a

unique tendency against the roughness geometries.

Section 5.2 describes experimental settings of PIV and drag force measurements. Section 5.3, 5.4, and 5.5 present temporally averaged flow fields, spatial distribution of turbulent statistics, and turbulent coherent structures, respectively. Subsequently section 5.6 and 5.7 analyze the air ventilation rate and drag coefficient based on the results demonstrated in previous sections. Major conclusions are presented in section 5.8.

5.2 Experimental setting

5.2.1 Wind tunnel and roughness configuration

Experiments were conducted in the wind tunnel at the Interdisciplinary Graduate School of Engineering Sciences, Kyushu University, Japan. The facility was the low-speed single-return wind tunnel with the test section of height 1 m, width 1.5 m and length 8 m. The floor of the wind tunnel was flat in PIV experiment, while the floating element with base dimensions of 720 mm \times 720 mm was attached in the square cavity located about 3 m downstream from the entrance of the test section in drag force measurements (figures 5-2(a) and 5-2(b)). The floating element was carefully adjusted so that its top surface was at the same height as the wind tunnel floor, and it was separated from the wind tunnel floor by a few millimeters on all sides.

Horizontally-long bars with a cross section of 25 mm \times 25 mm (hereafter, $H=25\text{mm}$) and horizontally-long bars with eaves which extend 25mm from the edges of bars were used as roughness models. The bars with eaves were made by attaching 2mm thick plates on the top of horizontally-long bars with rectangular cross section (25mm \times 23mm) ensuring the top height of the eaves was exactly 25mm. A part of the eaves were made of

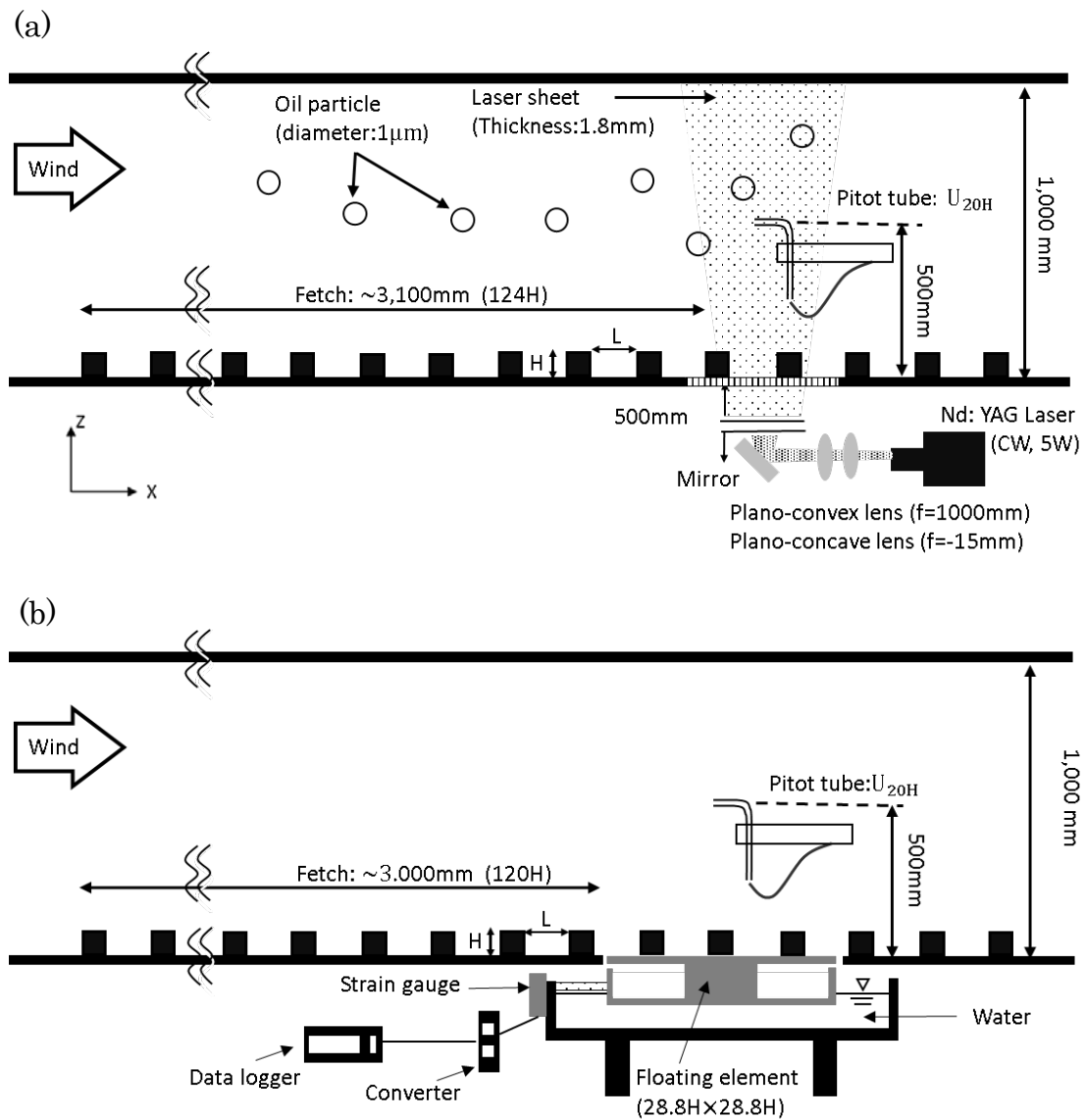


Figure 5-2 Side views of experimental setting
(a)PIV, (b) Drag coefficient

glass plate of 2 mm thick so as to transmit the laser sheet. Both PIV experiment and drag force measurement were conducted under six roughness arrangements (figure 5-3). In Case A, Case C, and Case E, roughness models without eaves were arranged perpendicular to the mean wind direction with three different canyon aspect ratios ($L/H = 3, 5, \text{ and } 7$, hereafter called as narrow, middle, and wide canyon, respectively), while

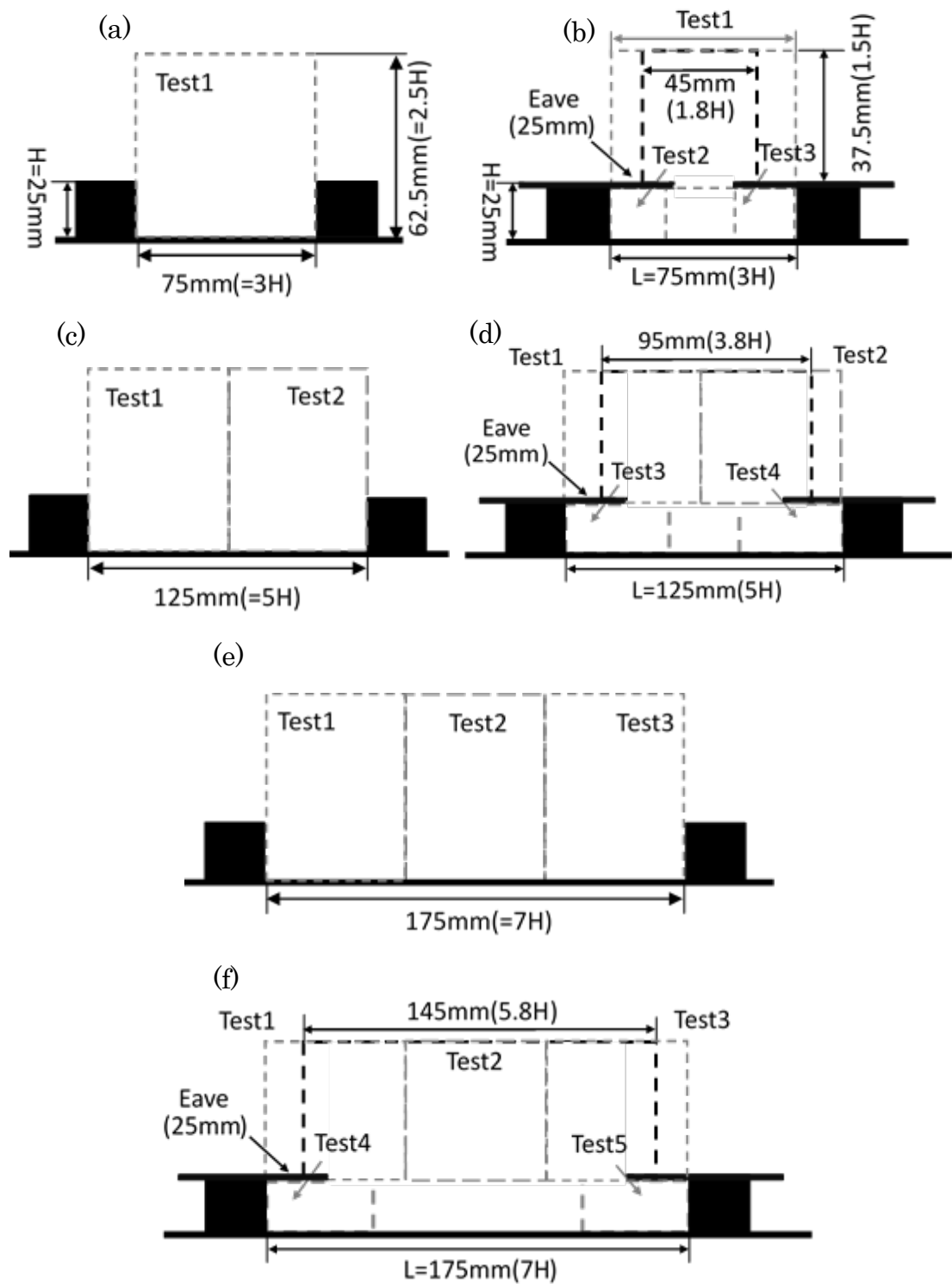


Figure 5-3 Diagrams of 2D street canyon models. Gray lines: separated measurement areas, black lines: regions where experimental data has high accuracy above the canyons

Case B, Case D, and Case F are roughness models with eaves (figure 5-3).

The fetch length was over one hundred times of the roughness height. The reference wind speed (U_{20H}) was approximately 2.2~2.3 m/s, and the corresponding Reynolds number based on H and U_{20H} was about 4000.

5.2.2 PIV setting

The plant oil particles of a 1 μ m diameter on average were used as tracer particles for PIV. The laser light sheet of a 1.8mm thickness was formed by the optical unit which consists of Nd:YAG 5W CW laser of $\lambda = 532\text{nm}$ (Coherent inc., Veldi-G5), a plano-concave lens, and a convex lens (focus length are -15 mm and 1000 mm, respectively). The laser sheet was emitted upward from beneath the wind tunnel through a thin grass plate (Figure 5-2(a)), and streamwise and vertical velocity components were measured. The images were photographed at a frequency of 1000 Hz by using a CMOS camera (Photron inc., FASTCOM SA-X) with a lens of f-number = 2.8 (Nikon inc., PC Micro-Nikkor 85mm f/2.8D).

In Case A, the entire street canyon was measured at once. On the other hand, it was difficult to measure the entire street canyon in a single test in other five cases because of the size limitation of camera view and shortage of the laser power, thus, the target areas were divided into several parts and measured separately (see figure5-3, gray lines). The spatial resolution of the camera and measurement time in each test were determined depending on the size of target area (see table5-1). The measurement time was over thirty seconds in all tests, which is considered enough for temporally averaging. The relative distance mutual position relation of the laser sheet, camera lens, and camera screen were kept at constant in all tests, thus, magnification ratio was constant and it was about 0.17mm/pixel.

Table 5-1 Spatial resolution and measurement duration

Case	Measurement area*	Spatial resolution[pixel]	Measurement time[s]
A	1	521×512	43.6
B	1	521×512	43.6
	2, 3	521×256	43.6
C	1, 2	521×512	43.6
D	1, 2	521×512	43.6
	3, 4	521×256	43.6
E	1, 2, 3	640×512	34.9
F	1, 2, 3	640×512	34.9
	4, 5	521×256	43.6

*The numbers correspond to the measurement area presented in figure 5-2 as test “X”

Image processing was conducted by a direct cross-correlation algorithm comprised of recursive cross-correlation and image transforming (window deformation iterative multigrid, WIDIM). WIDIM is considered highly reliable algorithm and widely used in recent studies (Adrian 2005, Scarano 2005; Stanislas et al. 2005). In WIDIM, the interrogation window size is changed arbitrary in each iteration step and small window size is desirable from the view point of spatial resolution. However, the number of particles in an interrogation window is reduced with the decrease of window size, and peak locking tends to occur. Therefore, the appropriate interrogation window size was determined by a preliminary test using histograms of instantaneous displacements of particle groups between two continuous images. Figures 5-4(a) and 5-4(b) show the results of image processing with different interrogation window size (21 × 21 pixel, 15 × 15 pixel, and 9 × 9 pixel). The peak locking is weak and acceptable level under the condition that the interrogation window size is 21 × 21 pixel and 15 × 15 pixel,

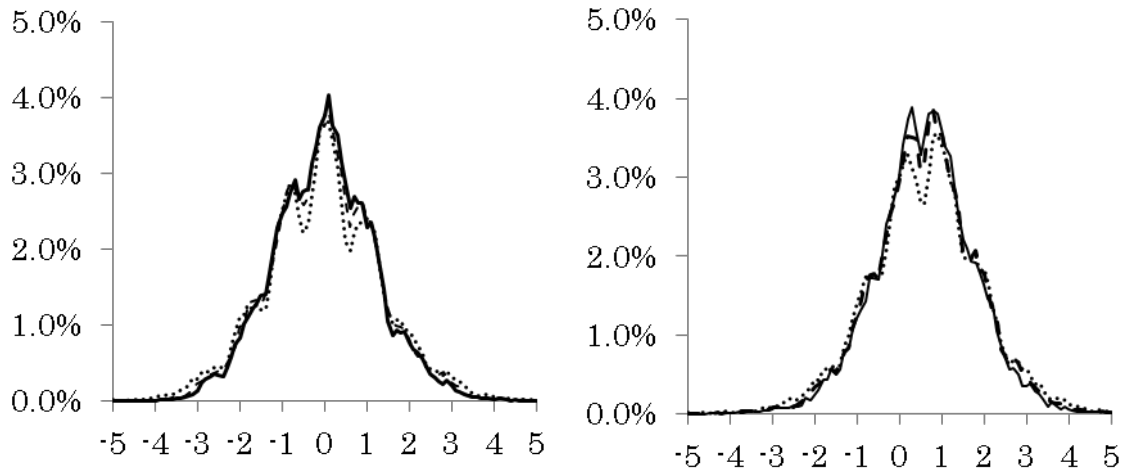


Figure 5-4 Histograms of particle displacement under different conditions of final interrogation window size in Case A. (a) Streamwise displacement ($\Delta x[\text{pixel} / \Delta t]$), (b) Vertical displacement ($\Delta z[\text{pixel}/\Delta t]$). Dashed line: 21×21 pixel, solid line: 15×15 pixel, dotted line: 9×9 pixel.

however, peak locking becomes strong if the window size is reduced to 9×9 pixel. From this result, the interrogation window size was changed in three steps (31×31 pixel, 21×21 pixel, 15×15 pixel) in this study.

5.2.3 Drag measurement

The total drag force acting on the blocks (τ_0) was directly measured using a strain gauge (Inter-face Inc., MB5) connected with the floating element of the wind tunnel. The measurement resolution of the gauge was 7.4×10^{-4} N, which is about 6% of the minimum drag measured in current roughness conditions. The strain gauge was reset to zero before each run using the measured value for 150 s under zero-flow conditions. The drag force was then measured for 950 s at a reference velocity of approximately 2.2 m/s at the height of $20H$, then measurement continued for 500 s under zero-flow conditions to confirm the negligible effect of elastic hysteresis. Measurements were conducted five times for each roughness condition and ensemble averages were calculated. The drag

force was converted into drag coefficient (C_d) by the equation 5-1.

$$C_d = \frac{\tau_0}{0.5\rho U_{20H}^2} \quad 5-1$$

Here, ρ [g/m³] is the density of air measured by a hydrothermograph (T&D corporation, TR-72nw/72nw-H).

The fetch length is important in drag force measurements in a wind tunnel because the decrease in the wind velocity near the arrays due to the fetch have a large influence on C_d . Although this study does not examine the influence of the fetch length on C_d , Hagishima et al. (2009) investigated the effect of fetch length on the drag coefficient in the same wind tunnel facility as this study. They employed a staggered cubical array with λ_p of 17.4%, and measured drag coefficient changing the fetch length from zero to $122.4H$ in five steps (0 , $28.8H$, $57.6H$, $86.4H$, and $122.4H$). Their results indicate the total surface drag of an array rapidly decreases with the increase of fetch length if the fetch length is under $30H$, and drag coefficient slightly decreases with fetch length if it is over $30H$. Drag coefficient does not appear to converge in their experiments, however, the dependence on the fetch length is weak under the condition of over $100H$. Although the shape of roughness in this study was different from that of Hagishima et al. (2009), the fetch length was close to their experiments. Hence, the author believes the experimental conditions of this study is acceptable.

5.3 Temporally averaged flow field structure

Figure 5-5 shows temporally-averaged velocity vector maps in the six cases: (a) $L/H = 3$, no eaves(Case A), (b) $L/H = 3$, having eaves(Case B), (c) $L/H = 5$, no eaves(Case C), (d) $L/H = 5$, having eaves(Case D), (e) $L/H = 7$, no eaves(Case E), (f) $L/H = 7$, having eaves(Case F). Hereafter, x and z indicate the streamwise and vertical direction. u and w

are streamwise and vertical velocity components. Capital letter and prime (*') mean temporally averaged and time variation component, respectively.

The mean wind speed ($\sqrt{U^2 + W^2}$) is indicated by color map. The data accuracy degrades near the edge of the laser sheet, especially in the regions above the eaves. Thus, preliminary tests were conducted to detect the regions with acceptable data accuracy based on the spatial distributions of correlation coefficients of particle pattern matching and data missing rates. The threshold value of correlation coefficients was over 0.3, while that of data missing rates was less than 10% in the present study. Following sections discuss the measurement results in the region where the two requirements are satisfied (black lines in figure 5-3).

In figure 5-5(a), a large recirculation eddy and a small secondary eddy are observed inside the canyon, and the center of the primary vortex is located at $(x/H, z/H) = (2.1, 0.5)$. These characteristics correspond with the well-known features of the wake interference flow in 2D street canyon (e.g. Leonardi et al. 2003). On the other hand, in Figure 5-5(b), a complicated flow structure consisting of multi-vortex arises inside the canyon. Namely, a clockwise eddy arises at the center of the canyon, and two counter-clockwise low-speed eddies appear under the upstream and downstream eaves. Although the center eddy is slightly larger than the other two eddies, the size of three eddies are relatively similar to each other. Wind speed is small in the most part of the canyon, however, the velocity at the crossover region of the center and right eddy around $x/H = 2.1$ is slightly large. This is probably due to the penetration of high-speed downward flow toward the canyon. Moreover, the high-speed flow is thought to be a driving force of the center and right eddies. This supposition is consistent with features of spatial distributions of turbulent statistics shown in the following sections. Meanwhile, the wind speed above the canyon

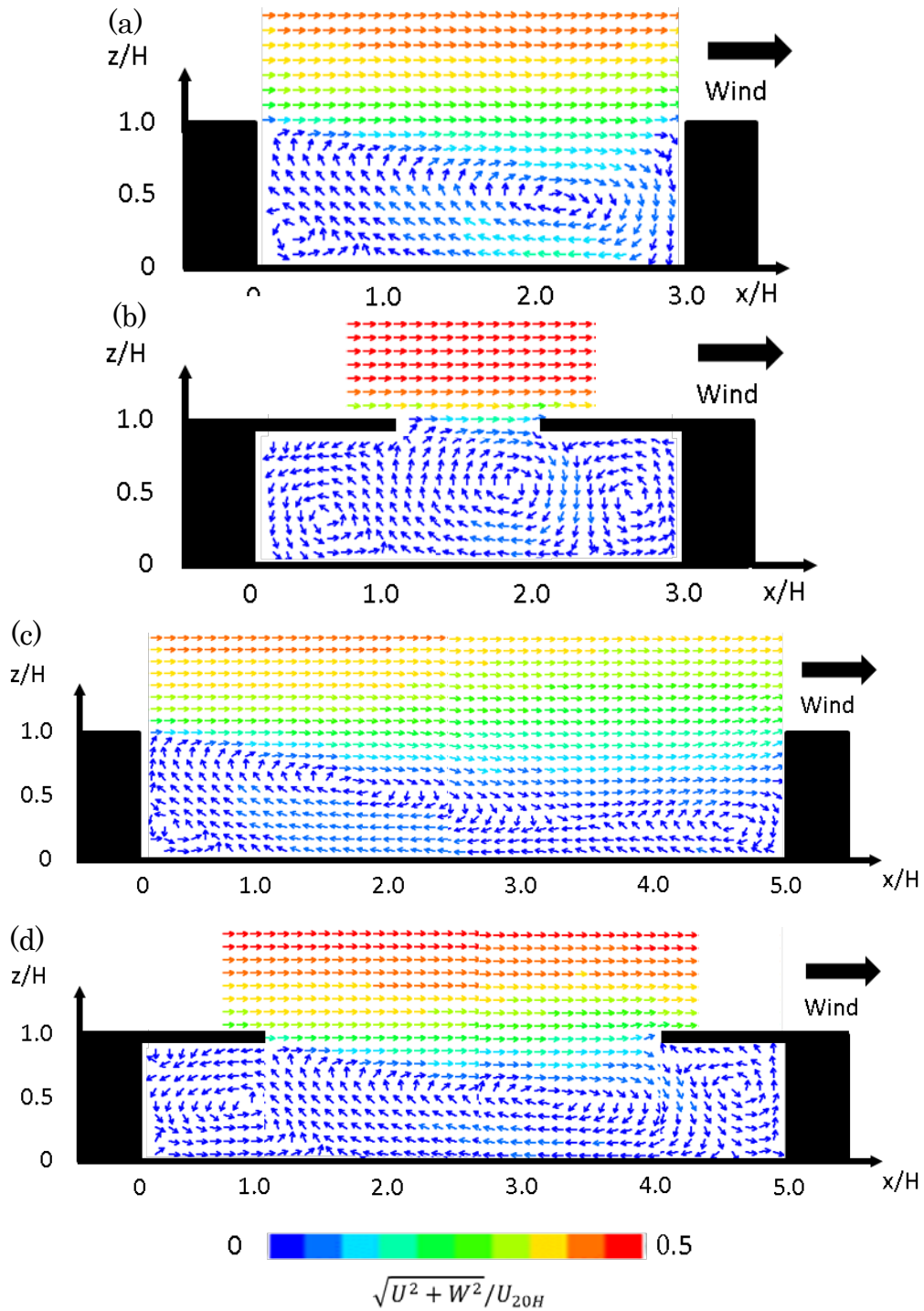
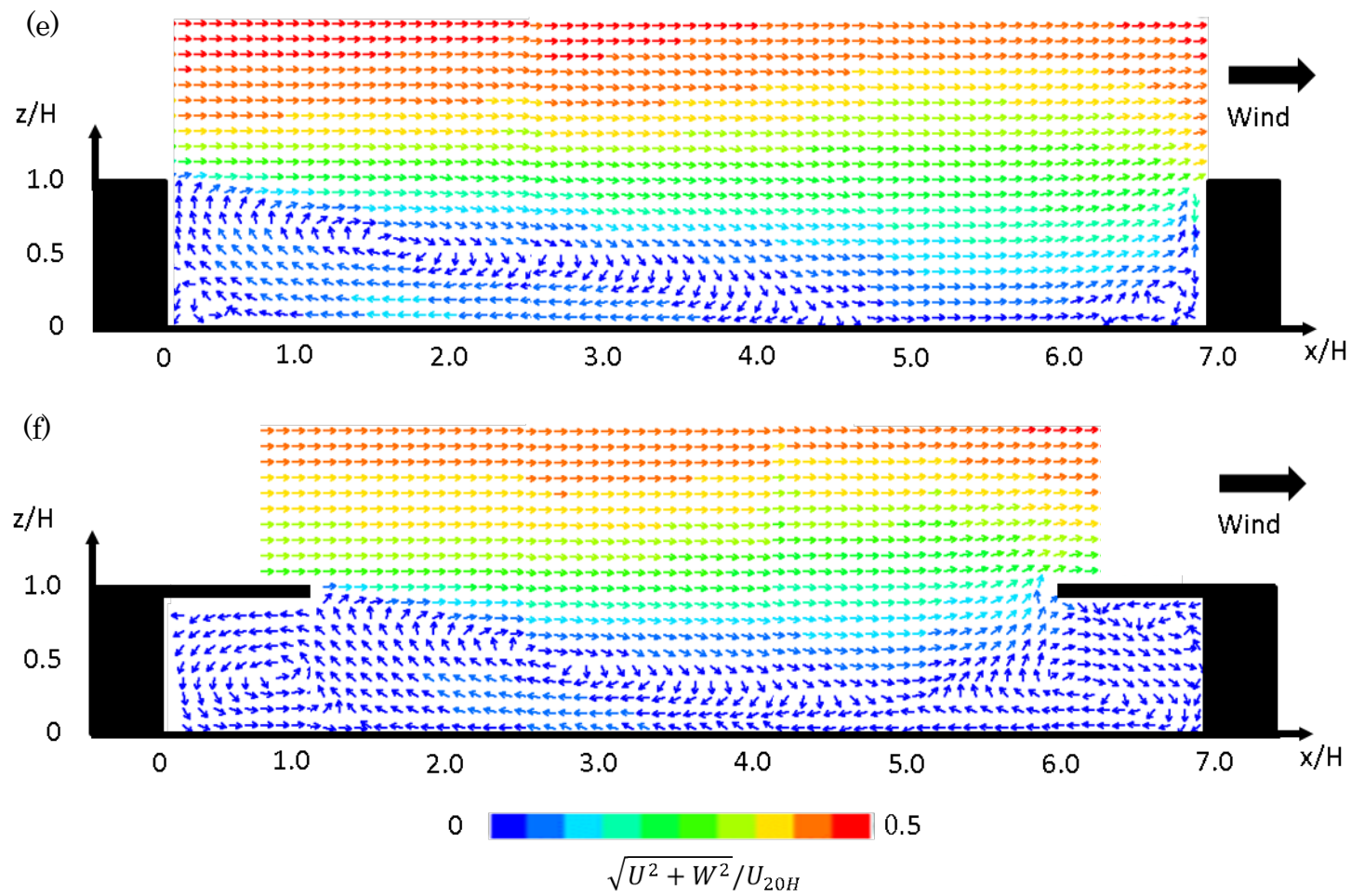


Figure 5-5 Temporally averaged velocity vector maps, (a) Case A ($L/H=3$, no eaves), (b) Case B ($L/H=3$, having eaves), (c) Case C ($L/H=5$, no eaves), (d) Case D ($L/H=5$, having eaves), (e) Case E ($L/H=7$, no eaves), (f) Case F ($L/H=7$, having eaves)

in Case B is larger than that of Case A, indicating the less influence on the flow field above the roof level.

In figure 5-5(c), a large elliptical vortex which is elongated to streamwise direction and a small secondary eddy is observed behind the windward obstacle. In addition, a vortex with a diameter of about $0.4H$ appears in front of the leeward block. The strong downward flow arises within the canyon around $x/H = 2.5$, however, it seems not to reach to the bottom of the canyon. On the other hand, in figure 5-5(d), an elliptical shape vortex appears within the canyon, but its center locates at $(x/H, z/H) = (3.4, 0.6)$ which is about $1.6H$ downstream from the center of the primary eddy in figure 5-5(c). In addition, two counter-clockwise vortexes are observed under the upstream and downstream eaves. The one locates under the upstream eave is driven by the elliptical vortex and its shape is nearly circular, while the other vortex is driven by the downward flow which occurs near the edge of the downstream eave and its shape is approximately a triangle. Similar to the narrow canyon with eaves (figure 5-5(b)), the wind speed above the canyon in Case D is larger than that of Case C, moreover, it is close to that in Case A. This is perhaps due to the same distance between eaves, and might indicate that they are aerodynamically rough in the same level.

In figure 5-5(e), the typical isolated flow pattern which contains an elliptic vortex, flow reattachment to the bottom of the canyon ($x/H = 4.2$), a flow parallel to the streamwise direction around $x/H = 5.0\sim 6.0$, and a small vortex in front of the downstream building, arises. An elliptical eddy is also observed in figure 5-5(f) but its center is shifted to $x/H = 2.9$ from $x/H = 1.8$ by the effect of the upstream eave. A counter-clockwise eddy appears under the upstream eave and its shape, center location and velocity magnitude are almost same with the eddy under the upstream eave in figure 5-5(d). By contrast, the flow



structure under the downstream eave is much different from that in figure 5-5(d) and a clockwise and a small counter-clockwise eddy coexist. It is thought that the clockwise eddy is caused by a strong upward flow around $x/H = 5.0\sim 6.0$, which does not arise in figure 5-5(d). Another important point is the wind speed above the canyon. Specifically, the deceleration degree of velocity above the canyons is similar in figures 5-5(e) and 5-5(f), and this might imply the variation of canyon flow structures has a small difference on flow fields above the canyon roof level.

5.4 Spatial distribution of turbulent statistics

5.4.1 Standard deviation

Figure 5-6 shows the spatial distributions of standard deviation of streamwise velocity normalized by the reference wind velocity (σ_u/U_{20H}), and figure 5-7 shows that of vertical velocity (σ_w/U_{20H}). In the narrow canyon cases (figures 5-6(a), 5-6(b), 5-7(a) and 5-7(b)), it is obvious that the turbulent intensity is drastically reduced nearly the entire regions in Case B compared with Case A, and this fact indicates the turbulence production by roughness is reduced by eaves. However, σ_u/U_{20H} and σ_w/U_{20H} are slightly large in a tongue-like region around $x/H = 2.1$. This seems to be caused by the high speed flow penetrating into the canyon through the gap of eaves. Figure 5-8(a) is a snapshot of a typical instantaneous flow motion around the tongue-like region (see squares with gray dashed lines in figures 5-6(b) and 5-7(b)). A high-speed downward flow arises around $x/H = 2.1$, and the wind speed of the center and right eddy is large. It is confirmed that this high-speed descend flow motion occurs intermittently by observing the continuous images of instantaneous flow fields.

Similar to the narrow canyon case, turbulent intensity is reduced in the most part of the

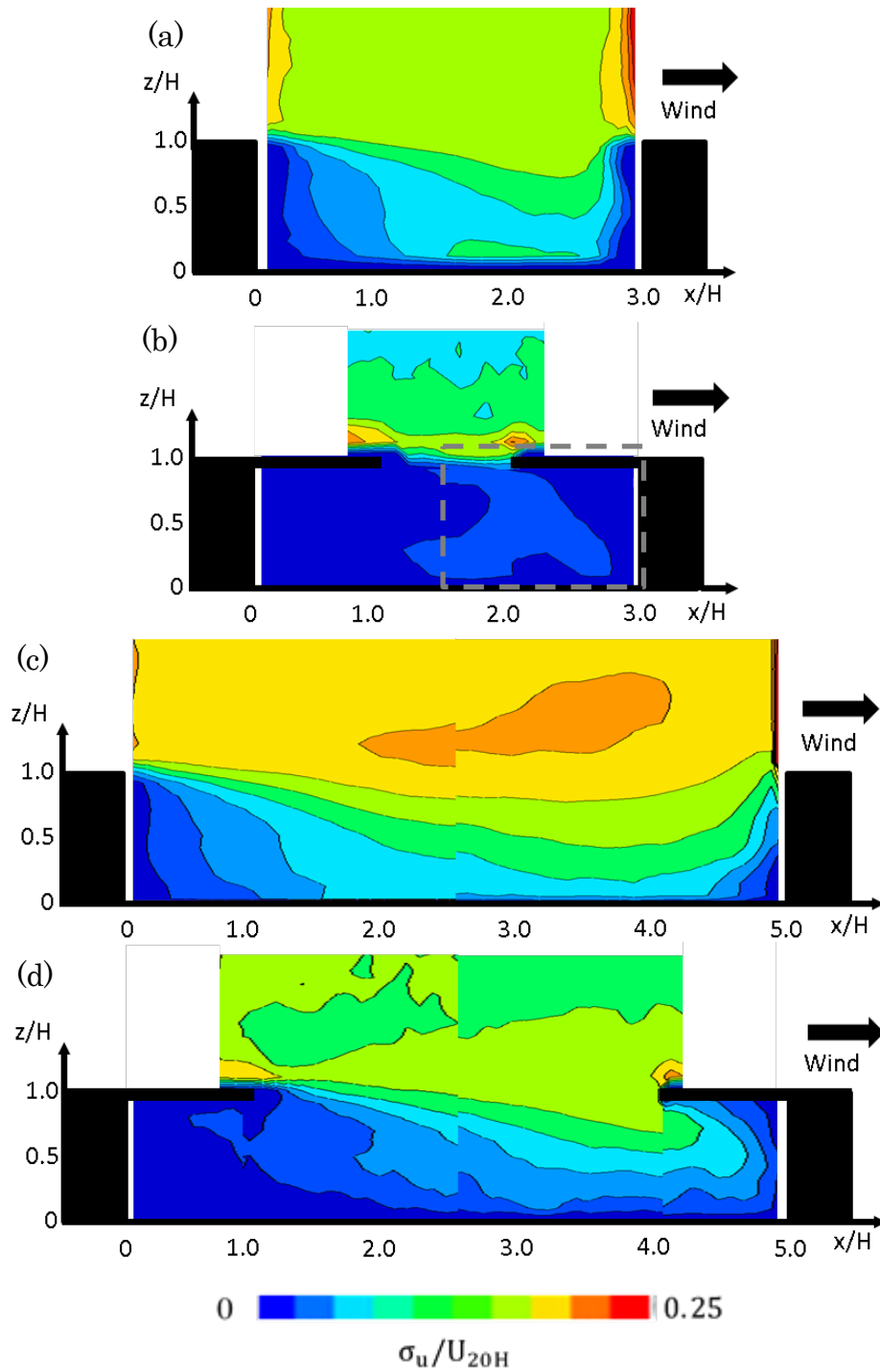
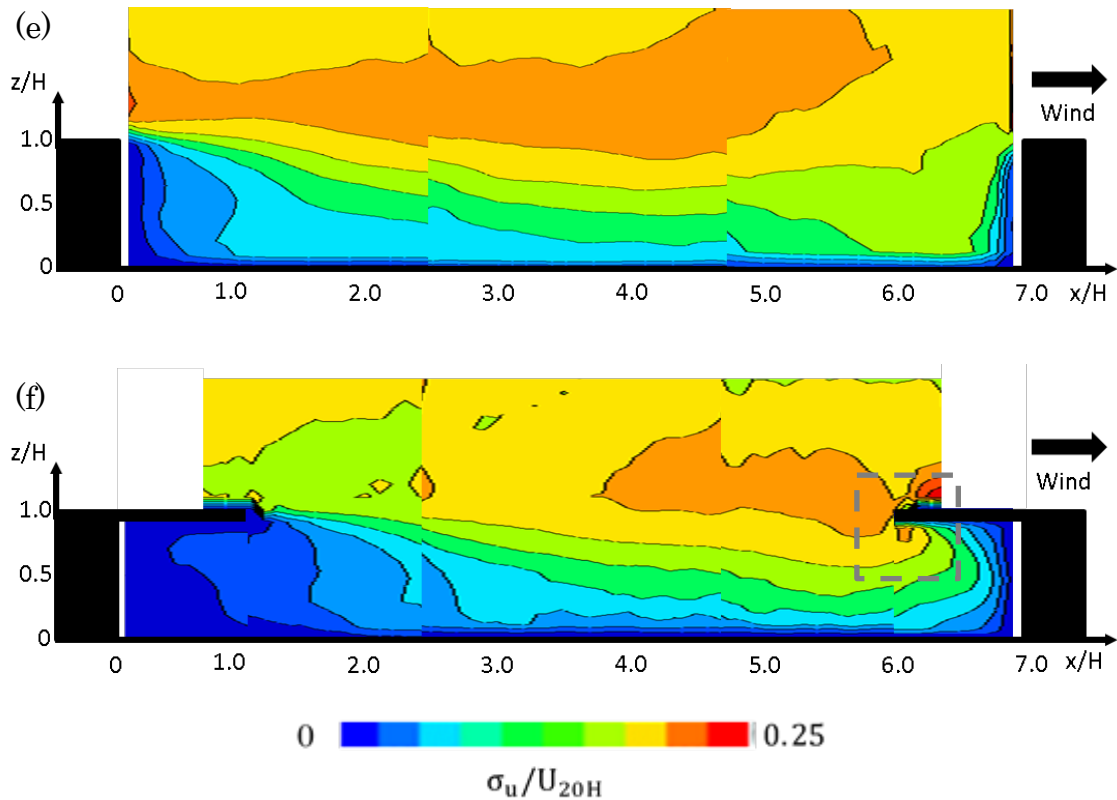


Figure 5-6 Spatial distributions of standard deviations of streamwise velocity component normalized by reference wind velocity (σ_u/U_{20H}), (a) Case A ($L/H=3$, no eaves), (b) Case B ($L/H=3$, having eaves), (c) Case C ($L/H=5$, no eaves), (d) Case D ($L/H=5$, having eaves), Continuation of Figure 5-5 (e) Case E ($L/H=7$, no eaves), (f) Case F ($L/H=7$, having eaves)



measurement area in the middle canyon case (figures 5-6(d) and 5-7(d)), however, both σ_u and σ_w gradually increase from the upstream to the downstream region especially at the canyon roof level, and arrowhead-like regions of large σ_u and σ_w are formed. This tendency is more apparent in the wide canyon case (figures 5-6(f) and 5-7(f)). Although turbulent intensity in the upstream region is much smaller than that in figures 5-6(e) and 5-7(e), the difference is small around the center of the canyon, and maximum peaks appear near the downstream eave.

Another interesting point is that σ_u is extremely large just above the downstream eave (see the square with black dashed line in figure 5-6(f)), and this is probably due to the high-speed streamwise flow and reverse flow which happen alternately. Figures 5-8(b) and 5-8(c) are snapshots of the two flow patterns in that region. Reverse flow with a speed of about $0 \sim 0.25$ occurs at a moment, while high-speed forward flow arises at another

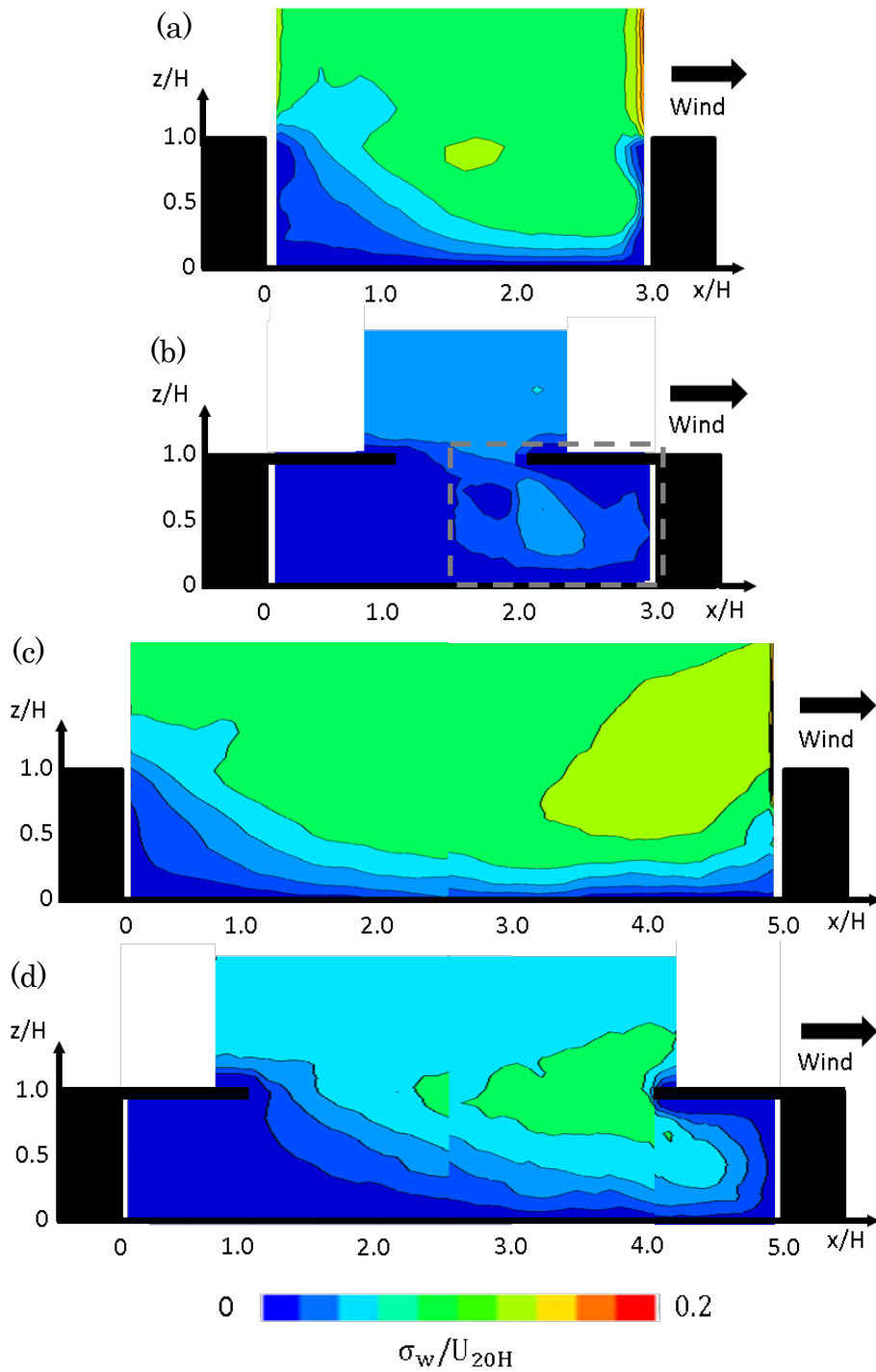


Figure 5-7 Spatial distributions of standard deviations of vertical velocity component normalized by reference wind velocity (σ_w/U_{20H}), (a) Case A ($L/H=3$, no eaves), (b) Case B ($L/H=3$, having eaves), (c) Case C ($L/H=5$, no eaves), (d) Case D ($L/H=5$, having eaves), (e) Case E ($L/H=7$, no eaves), (f) Case F ($L/H=7$, having eaves)

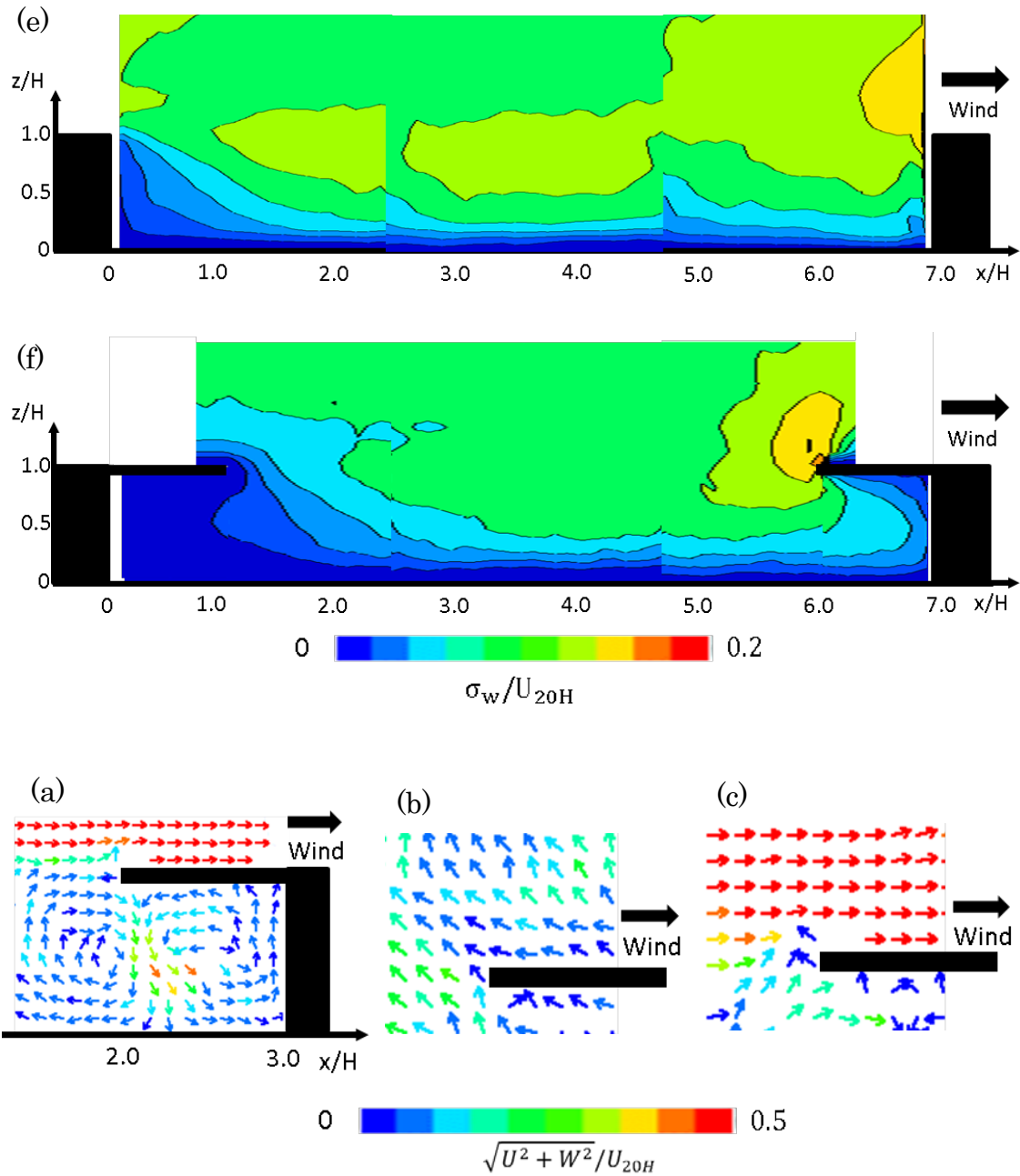


Figure 5-8 Snapshots of typical flow motions near eaves, (a) high-speed downward flow near $x/H=2.1$ in case B (within the squares with gray dashed lines in Figure 5-6(b) and Figure 5-7(b)), (b) and (c) low speed reverse flow and high speed forward flow above the eaves (within the squares with gray dashed lines in Figure 5-6(f))

moment, increasing σ_u in that region.

5.4.2 Reynolds stress

Figure 5-9 is the contour maps of the Reynolds stress normalized by square of reference wind velocity ($-\overline{u'w'}/U_{20H}^2$). The streamwise-elongated regions of large Reynolds stress are observed at the canyon roof height in figures 5-8(a), 5-8(c), and 5-8(e). This feature is correspond with the results of the past PIV experiments for 2D street canyons with various canyon aspect ratio (e.g. Simoens et al. 2007; Annalisa 2014).

Meanwhile, the spatial distributions of Reynolds stress of the three canyons with eaves is obviously different from those of the canyons without eave, and similar trends are confirmed among the spatial distributions of σ_u , σ_w and Reynolds stress. For example, Reynolds stress is small in the almost entire region in figure 5-9(b), while an arrowhead-like region of large Reynolds stress appears in figure 5-9(d). This is perhaps due to the fact that Reynolds stress is the product of u' and w' . On the other hand, it is noteworthy that Reynolds stress rapidly increases at $x/H = 5.0\sim 6.0$ in figure 5-9(f), and the excessively large maximum peak is caused near the edge of the downstream eave. This result indicates that the influence of the eaves causes to drastic change the momentum exchange process between the regions above and inside the canyon.

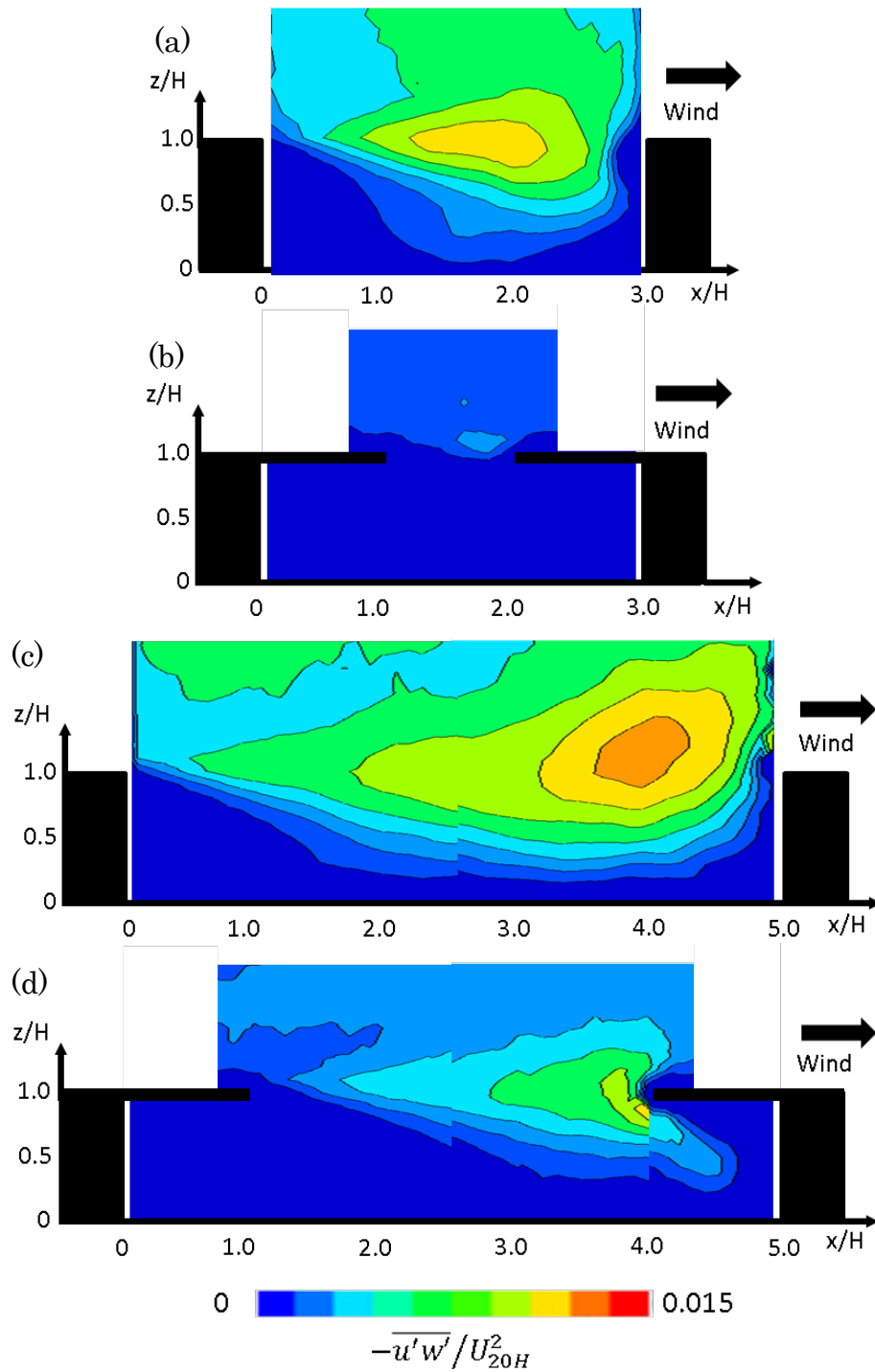
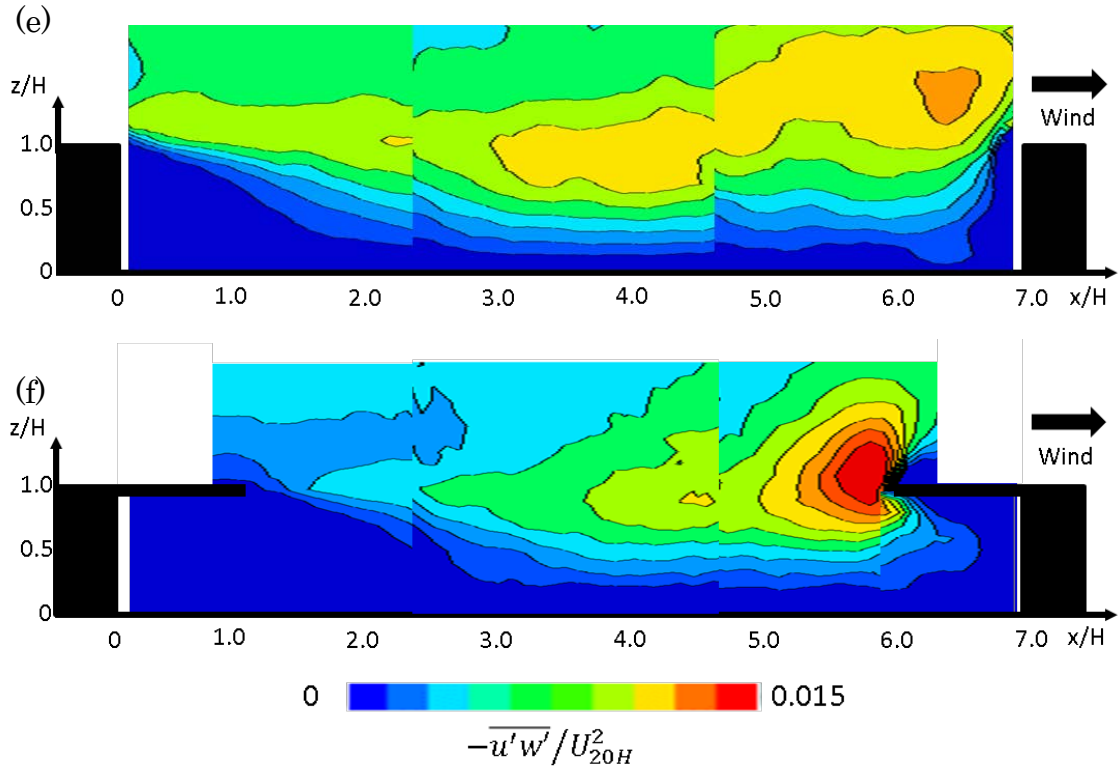


Figure 5-9 Spatial distributions of Reynolds stress normalized by reference wind velocity ($-\overline{u'w'}/U_{20H}^2$), (a) Case A ($L/H=3$, no eaves), (b) Case B ($L/H=3$, having eaves), (c) Case C ($L/H=5$, no eaves), (d) Case D ($L/H=5$, having eaves), (e) Case E ($L/H=7$, no eaves), (f) Case F ($L/H=7$, having eaves)



5.5 Turbulent coherent structure

Turbulent coherent structure was investigated by spatial distributions of two point correlation coefficients of streamwise and vertical velocity components (R_{uu} and R_{ww}) calculated by the equation 5-2.

$$R_{u_i u_i}(\Delta x, \Delta z) = \frac{\overline{u'_i(x_0, z_0, t) u'_i(x_0 + \Delta x, z_0 + \Delta z, t)}}{\sigma_{u_i}(x_0, z_0) \sigma_{u_i}(x_0 + \Delta x, z_0 + \Delta z)} \quad (i = 1, 2) \quad 5-2$$

Here, u'_1 and u'_2 are u' and w' , x_0 and z_0 are streamwise and vertical coordinates of a reference point, Δx and Δz are the distance from a reference point. Table 5-2 is the list of the positions of reference points in each case. In this research, the reference points are set at slightly lower and higher positions of the canyon roof level ($z_0 = 0.8H$ and $z_0 = 1.1H$) to clarify how eaves affect the turbulent coherent structure. The streamwise locations of the reference points are the center of the canyons

Table 5-2 Location of the reference points in each case

Case	(x_0, z_0)
A	(1.5H,0.8H), (1.5H,1.1H)
B	(1.5H,0.8H), (1.5H,1.1H)
C	(2.5H,0.8H), (2.5H,1.1H)
D	(2.5H,0.8H), (2.5H,1.1H)
E	(1.5H,0.8H), (3.5H,0.8H), (5.5H, 0.8H) (1.5H,1.1H), (3.5H,1.1H), (5.5H, 1.1H)
F	(1.5H,0.8H), (3.5H,0.8H), (5.5H, 0.8H) (1.5H,1.1H), (3.5H,1.1H), (5.5H, 1.1H)

in Case A, Case B ($x_0 = 1.5H$), Case C, and Case D ($x_0 = 2.5H$). On the other hand, the reference points in Case E and Case F are located at $x_0 = 1.5H$, $3.5H$ and $5.5H$ to investigate the turbulent structures of wider canyons.

Figure 5-10 are the spatial distributions of the two point correlation coefficients of streamwise velocity component (R_{uu}) with the reference points at $z_0 = 0.8H$, and figure 5-11 shows R_{uu} with the reference points at $z_0 = 1.1H$. In the canyons without eaves (figures 5-10(a), 5-10(c) and 5-10(e), 5-11(a), 5-11(c), and 5-11(e)), it is demonstrated that the regions of the large correlation coefficients are elongated in the streamwise direction, and it seems to be inclined toward upper right. Such inclination of turbulent coherent structures is consistent with the result of previous studies with a various types of roughness conditions (e.g. Kanda et al. 2004; Leonardi, et al. 2004; Coceal et al., 2007; Reynolds and Castro 2008). It is noteworthy that the large R_{uu} areas stretch across the regions above and inside the canyons even if the reference points are located above canyon roof height, indicating the turbulent coherent structures penetrate into the canyons.

On the other hand, the areas of large R_{uu} in the canyons with eaves are much smaller than that in the canyons without eaves, especially in the narrow canyon. In Figure 5-10(b),

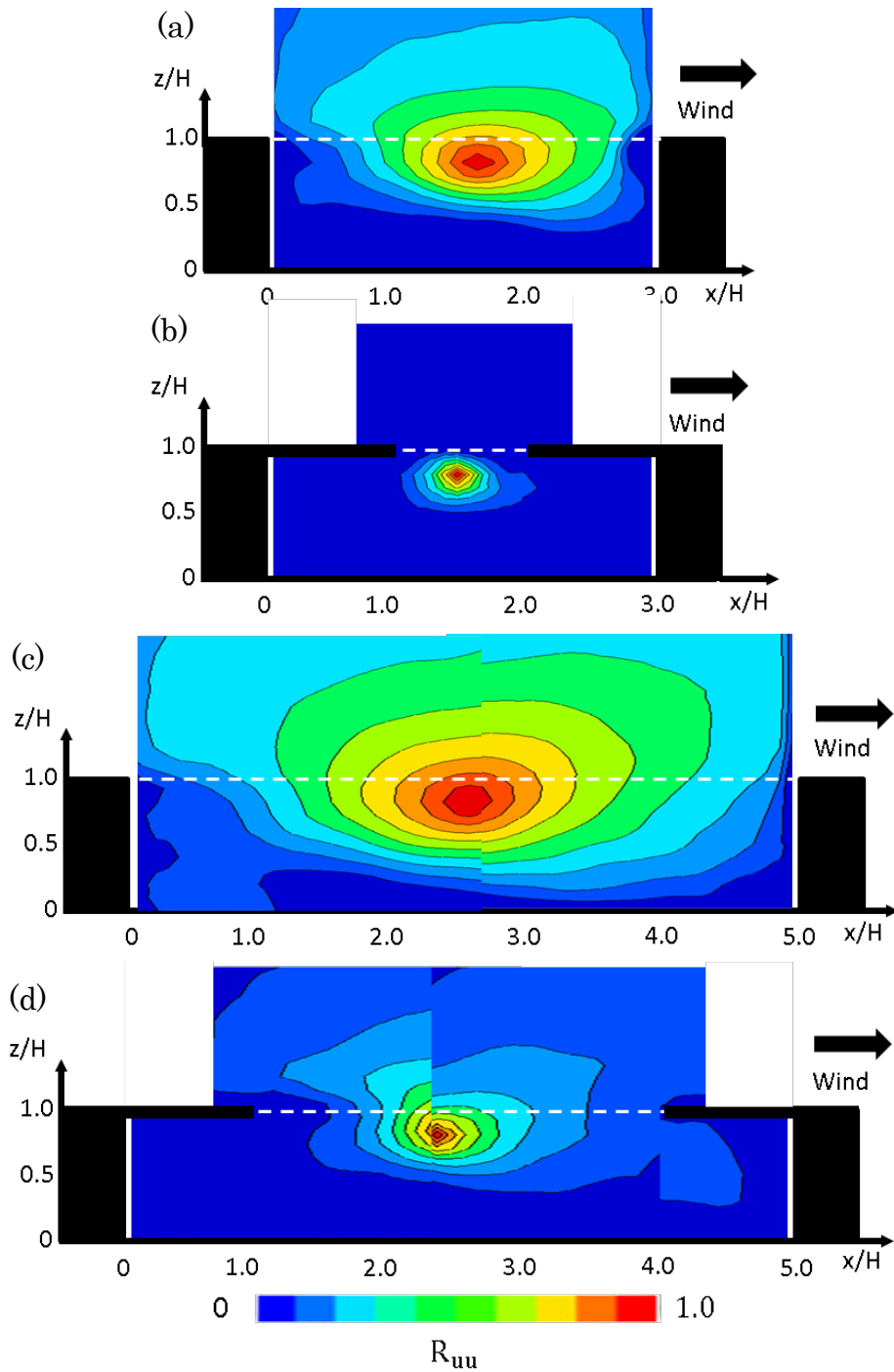
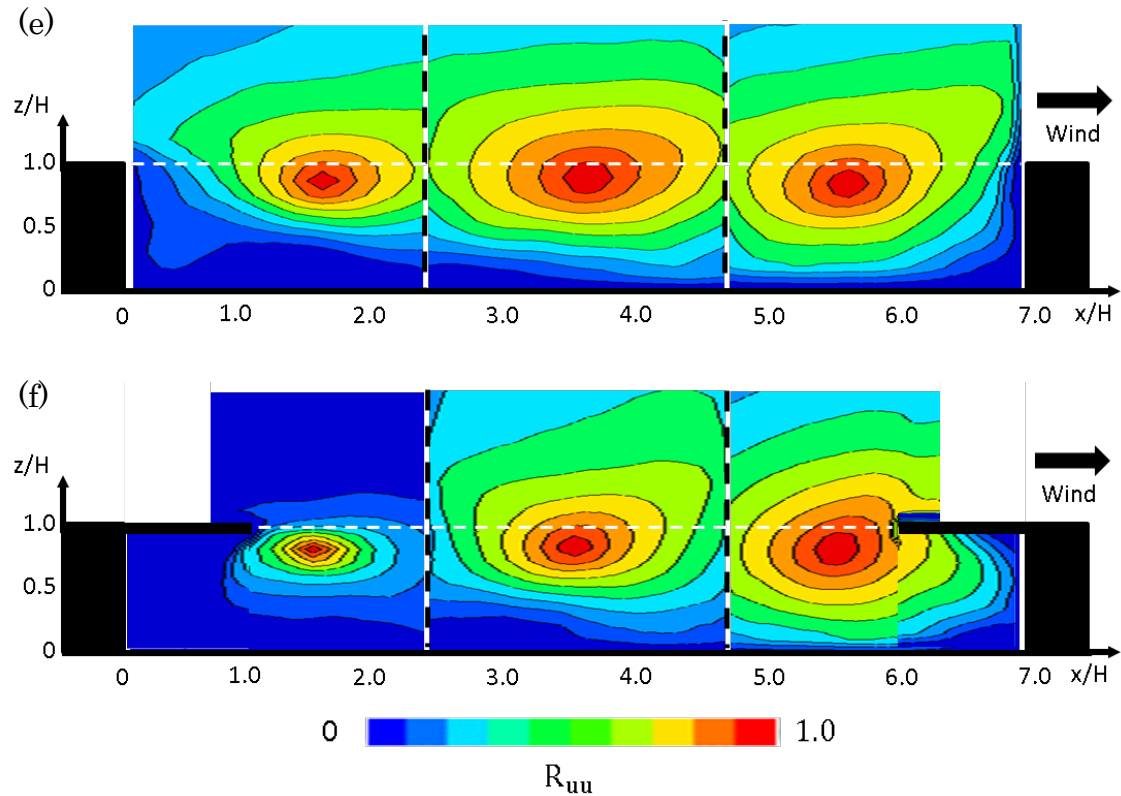


Figure 5-10 Spatial distributions of two point correlation coefficients of streamwise velocity component (R_{uu}) with reference points located below the canyon roof height (white dashed lines), (a) Case A ($L/H=3$, no eaves), (b) Case B ($L/H=3$, having eaves), (c) Case C ($L/H=5$, no eaves), (d) Case D ($L/H=5$, having eaves), (e) Case E ($L/H=7$, no eaves), (f) Case F ($L/H=7$, having eaves)



R_{uu} is almost zero above the canyon, while in figure 5-11(b), R_{uu} is extremely small in the canyon even in the region around $x/H = 2.1$, where the high speed downward flow comes from above the canyon intermittently (see section 5.4.1). These results implies that large size turbulent coherent structures cannot penetrate into the canyons by the effect of the eaves, and turbulent flows above and inside the canyon is irrelevant each other.

Similarly, the regions of large R_{uu} in figures 5-10(b) and 5-11(d) are divided at the canyon roof level. Another curious result is that the size of turbulent coherent structure above the canyon is similar in figures 5-11(a) and 5-11(d), however, the large R_{uu} area does not extend to above the canyon under the conditions that the reference point locate below the canyon roof level (figure 5-10(d)). This result might indicates interrelation of turbulent flow is much weaker in the idle canyon with eaves compared to that in the narrow canyon without eave, though similar size turbulent coherent structures

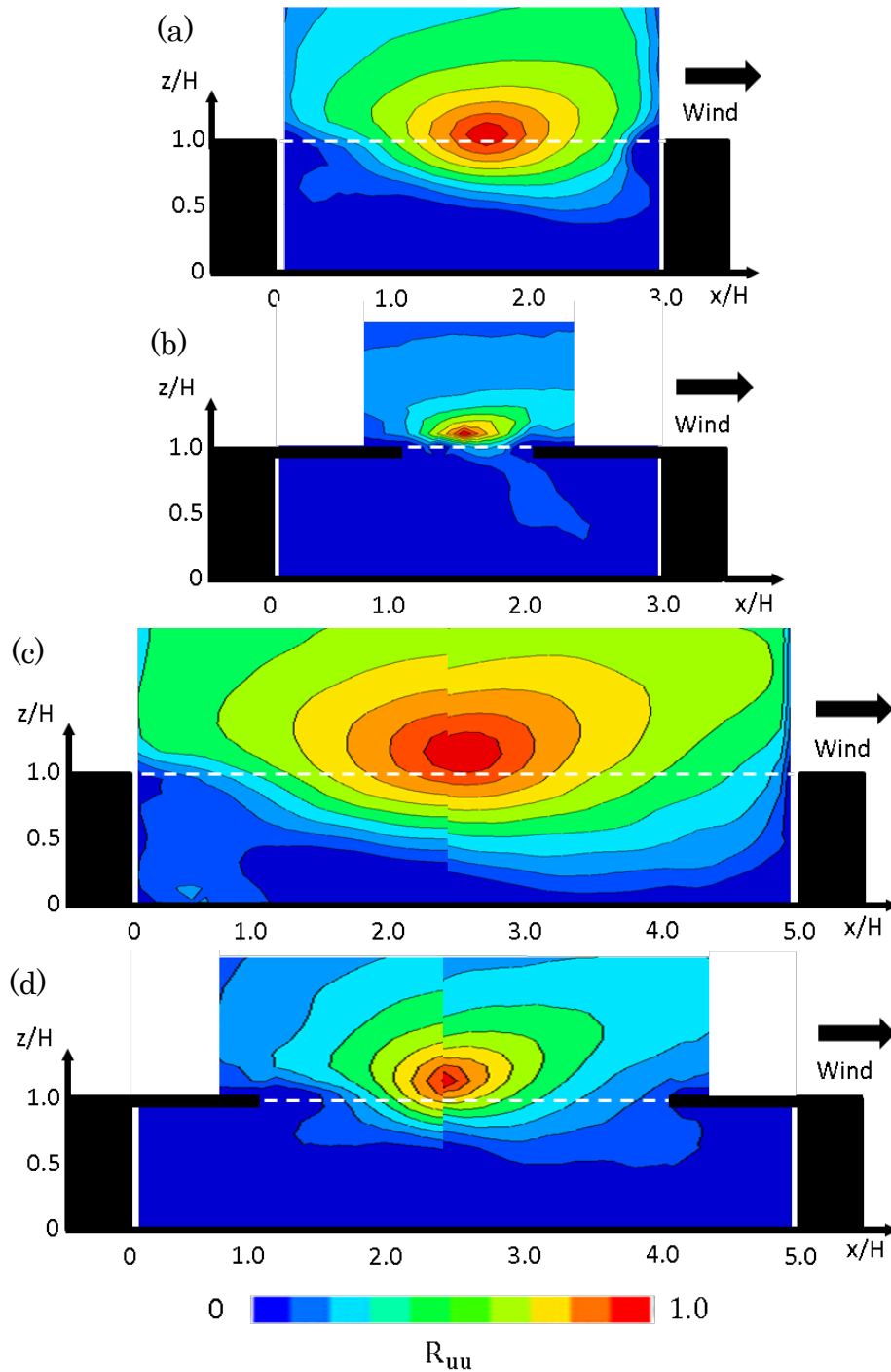
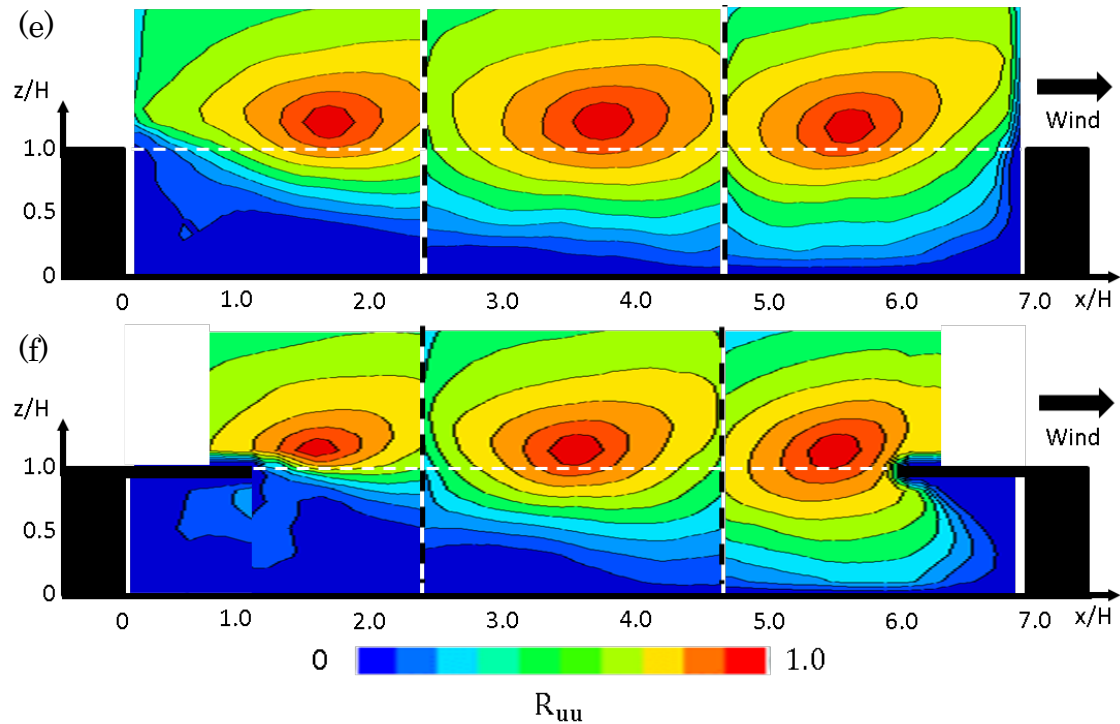


Figure 5-11 Spatial distributions of two point correlation coefficient of streamwise velocity component (R_{uu}) with reference points located above the canyon roof height (white dashed lines), (a) Case A ($L/H=3$, no eaves), (b) Case B ($L/H=3$, having eaves), (c) Case C ($L/H=5$, no eaves), (d) Case D ($L/H=5$, having eaves), (e) Case E ($L/H=7$, no eaves), (f) Case F ($L/H=7$, having eaves)



exist in the two cases.

Contrary to the narrow and middle canyon cases, the influence of the eaves does not reach the entire measurement area. Comparison among figures 5-10(e), 5-10(f), 5-11(e), and 5-11(f) demonstrates that the upstream eave has a large influence on coherent structures around $x/H = 1.0 \sim 2.3$, however, the effect of the eaves is weak in the center and downstream region. Especially, the downstream eave hardly affects the turbulent coherent structure even in the immediate vicinity to it, and the region of large correlation coefficient extends below the downstream eave.

Figures 5-12 and 5-13 show the spatial distributions of R_{ww} with the reference points which are located below and above the canyon roof height. For a qualitative point of view, the effect of the eaves on R_{ww} is similar to that on R_{uu} . Large size turbulent coherent structures are obstructed by the eaves and cannot penetrate into the canyon in the narrow

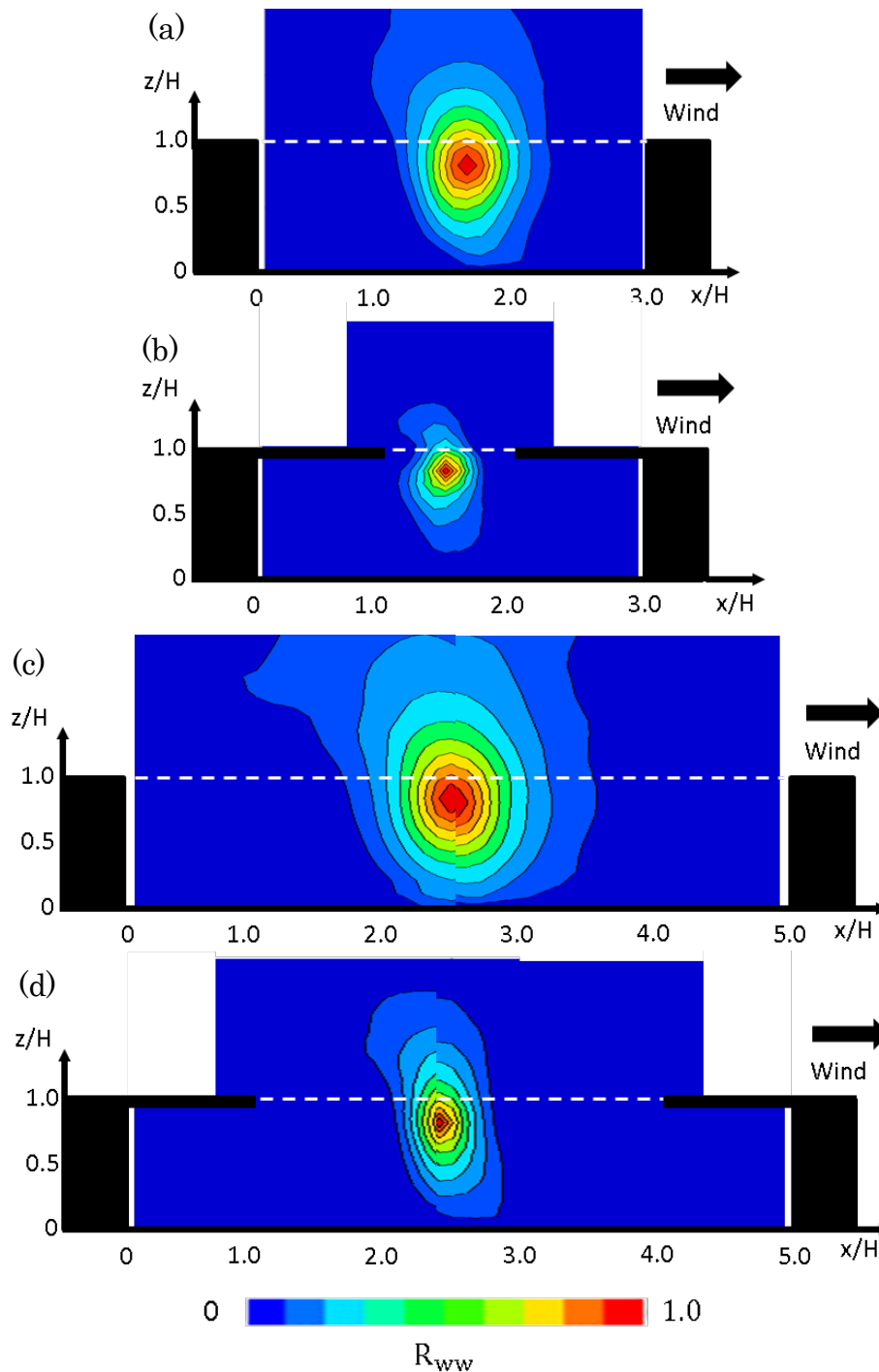
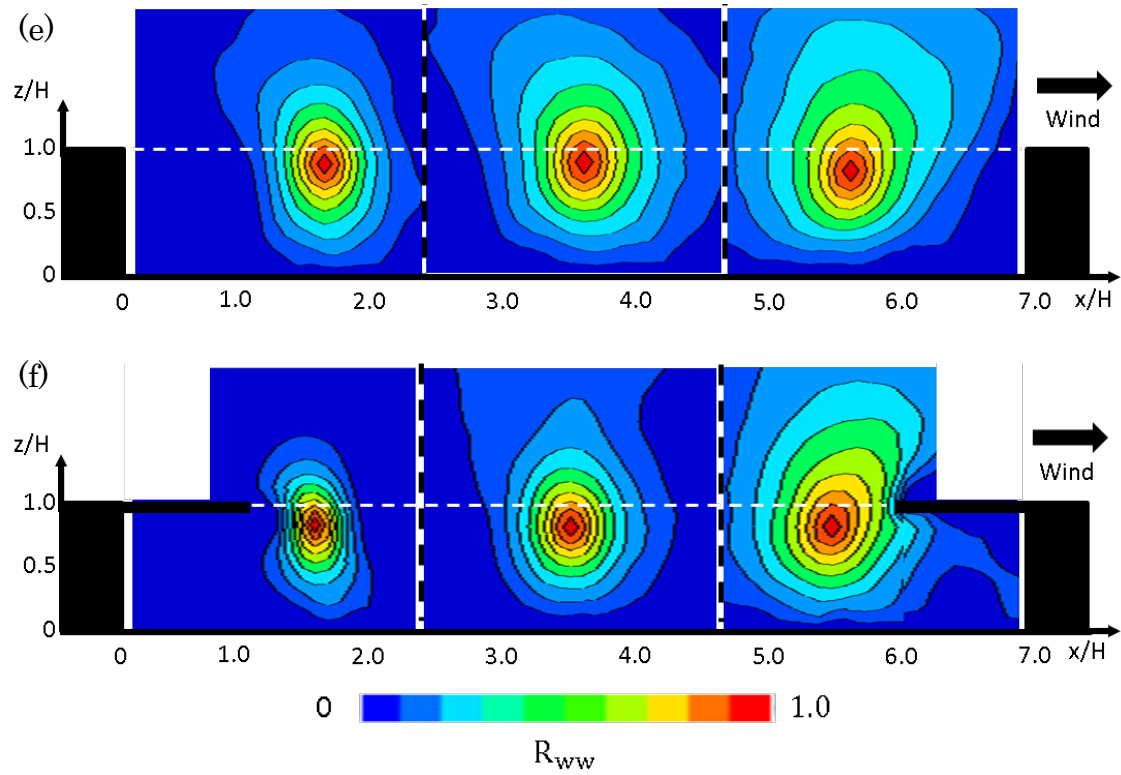


Figure 5-12 Spatial distributions of two point correlation coefficient of vertical velocity component (R_{ww}) with reference points located below the canyon roof height (white dashed lines), (a) Case A ($L/H=3$, no eaves), (b) Case B ($L/H=3$, having eaves), (c) Case C ($L/H=5$, no eaves), (d) Case D ($L/H=5$, having eaves), (e) Case E ($L/H=7$, no eaves), (f) Case F ($L/H=7$, having eaves)



canyon with eaves, and the size of turbulent coherent structures is highly reduced in the middle width canyon with eaves. By contrast, the region affected by the eaves is only the upstream, and large coherent motions are appear around the roughness in the wide canyon with eaves.

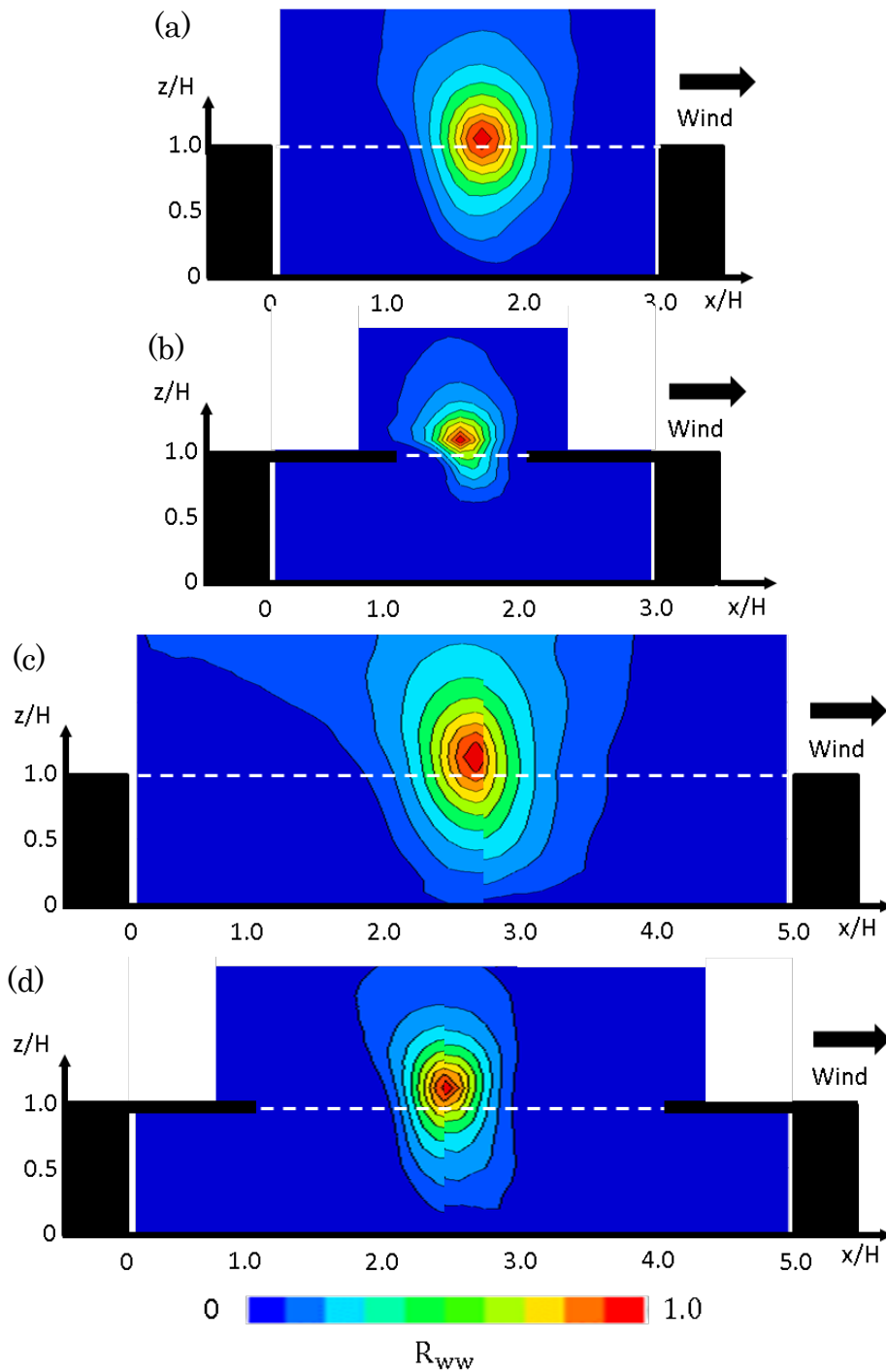
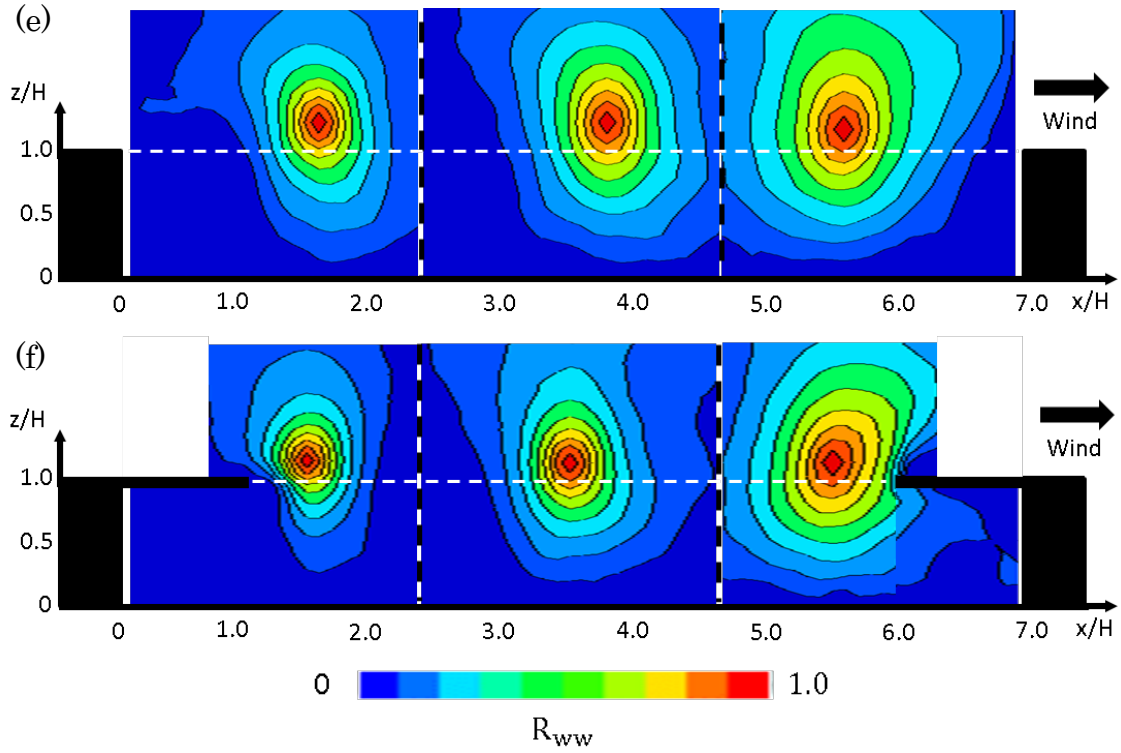


Figure 5-13 Spatial distributions of two point correlation coefficient of vertical velocity component (R_{ww}) with reference points located above the canyon roof height (white dashed lines), (a) Case A ($L/H=3$, no eaves), (b) Case B ($L/H=3$, having eaves), (c) Case C ($L/H=5$, no eaves), (d) Case D ($L/H=5$, having eaves), (e) Case E ($L/H=7$, no eaves), (f) Case F ($L/H=7$, having eaves)



5.6 Canyon ventilation rate

The ventilation rate ($Q[s^{-1}]$) normalized by the canyon time scale defined by H and U_{20H} ($T_c [s] = H/U_{20H}$, Liu et al. 2005) was calculated by the equation 5-3.

$$Q \cdot T_c = 0.5 \times \frac{H}{U_{20H}} \times \left(\frac{\int (\int (W + w')_+ dA - \int (W + w')_- dA) dt}{T \cdot V} \right)_{z=H} \quad 5-3$$

Here, $A [m^2]$ is the opening space of the canyons, $T[s]$ is measurement time, $V[m^3]$ is canyon volume, and the subscript sign means the inflow ($W + w' > 0$) and outflow ($W + w' < 0$) at the canyon roof level ($z/H = 1$). The temporally average of inflow and outflow should be equal in 2D street canyons if an averaging time is enough long. However, several percents of imbalance are found in the calculation results, therefore, the averaged values of inflow and outflow are used in the present study. In addition, the contribution of the time averaged velocity component on the canyon ventilation ($Q_m \cdot T_c$) was

calculated by the equation 5-4.

$$Q_m \cdot T_c = 0.5 \times \frac{H}{U_{20H}} \times \left(\frac{\int (W)_+ dA - \int (W)_- dA}{T \cdot V} \right) \quad 5-4$$

Figure 5-14 shows $Q \cdot T_c$ and $Q_m \cdot T_c$ of the six cases. The ventilation rate of the narrow canyon with eaves (Case B) is only 11% of that in the narrow canyons without eaves (Case A). This decreasing ratio is larger than the reduction of the canyon opening space (33%). The ratio of $Q \cdot T_c$ between the middle canyons without and with eaves (Case C and Case D) is 48%, and it is still smaller than the decreasing rate of the canyon opening space (60%). In contrast, $Q \cdot T_c$ of the wide canyon with eaves (Case F) keeps 70% of that of the wide canyon without eaves (Case E), and it corresponds with the proportion of canyon opening space between the two cases (71%). These results imply the fact that the canyon ventilation mechanism is highly changed by the effect of the eaves under the condition that canyon aspect ratio is small, however, the effect of the eaves decreases with the increase of the canyon aspect ratio, and finally it has almost no difference on canyon ventilation process.

It is noteworthy that the contribution of the turbulent velocity component to canyon

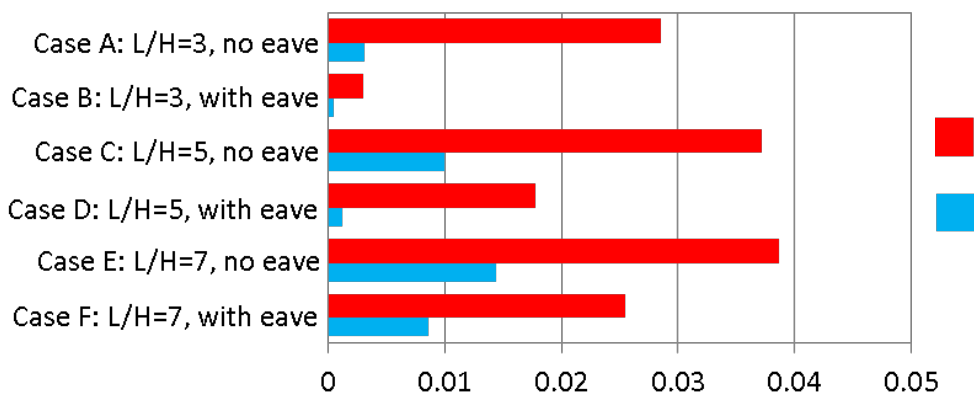


Figure 5-14 Canyon ventilation rate; $Q \cdot T_c$ and $Q_m \cdot T_c$

ventilation is much important than that of the temporally averaged velocity component, thereby, the difference of the ventilation mechanism among each case might be explained associated with the nature of turbulent flow fields. In the narrow canyon with eaves, σ_w is small (figure 5-7(b)) and turbulent coherent structures with large turbulent intensity cannot penetrate into the canyon (figure 5-12(b) and figure 5-13(b)), reducing the air mixing between the regions above and inside the canyon. Similarly, the turbulent intensity and coherent structures are small in the middle canyon with eaves. However, σ_w is large near the downstream eave ($x/H = 3\sim 4$), and the size of coherent structures is not decreased as much as in the narrow canyon case, maintaining the ventilation rate to a certain degree. Meanwhile, the influence of eaves on the turbulent flow field properties is limited in the wide canyon except for the upstream region, thus, the ventilation mechanism is unchanged.

5.7 Drag coefficient

C_d of 6 roughness arrangements are presented in figure 5-15. In addition, C_d of a smooth surface calculated by the equation 5-5(Hino, 1992) are also presented for a reference.

$$C_d = (2 \log Re_x - 0.65)^{-2.3} \quad 5-5$$

Here, Re_x is the Reynolds number defined by the free stream velocity (U_{20H}) and the distance from the leading edge of the test section to the floating element (= 3,036mm).

In the 2D street canyons without eaves (square plots), C_d decreases with the decrease of the canyon aspect ratio from 7 to 3. As figure 5-5(e) presents, a flow reattachment to the bottom of the canyon, and a flow parallel to the streamwise direction are observed in

the wide canyon without eaves (Case E), indicating the typical isolated flow pattern appears inside the canyon. Meanwhile, in the middle canyon without eaves (Case C), the downward flow arise within the canyon does not reach to the ground because of the reverse flow along the bottom of the canon. Thus, the weak interaction of the wake flow is caused in the canyon, and it is probably the reason why C_d of Case C is smaller than that of Case E. On the other hand, the canyon flow structure is much different in the narrow canyon (Case A) compared with other two cases, and the recirculation eddy extends from end to end of the canyon, resulting in the large decrease of C_d .

The value of C_d of the canyons with eaves are smaller than that in the canyons without eaves, however, the reduction rates of them are highly different among the cases. C_d of the wide canyon with eaves (Case F) keeps 88% of that without eaves (Case E). Moreover, it is close to C_d of the middle canyon without eaves (the ratio of Case F and Case C is 91%). Making a comparison between figure 5-5(c) and figure 5-5(f), the flow field structures in the canyons demonstrate similar features, such as the downward flow which

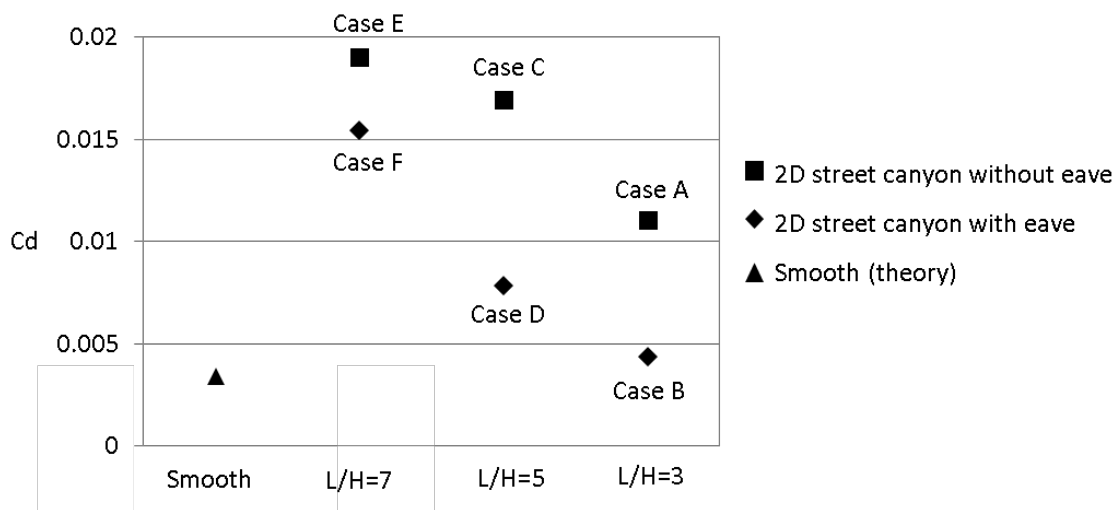


Figure 5-15 Drag coefficient (C_d) in each case. C_d of a smooth surface induced by equation 5-5 (hino, 1992) is also presented

does not reach to the canyon bottom. Hence, C_d of the two cases are close each other. On the other hand, C_d drops sharply between Case F and Case D. In figure 5-5(d), the elliptical eddy which extends in the streamwise direction occupies the region of $x/H = 1$ to 4.0, where is beneath the canyon opening. The transition of canyon flow structures between Case F and Case D is highly similar to that between Case C and Case A. In consequence, C_d decreases suddenly between Case F and Case D. Meanwhile, C_d of Case B is about 40% of Case A, and it is only 22% larger than that of a smooth surface.. In Case B, the distance between the upstream and downstream eaves are only $1H$, and the smooth surfaces with $3H$, which is consisted of eaves and building roofs, exist both sides of the gap (figure 5-3) thus, the influence of roughness on the flow fields is extremely small as if a nearly smooth surface is formed at $z/H = 1$. This result consist of the large velocity magnitude immediately above the canyon presented in figure 5-5(b).

5.8 Conclusion

The PIV experiments were conducted to investigate the effect of ancillary structures on turbulent flow fields employing 2D street canyons of three different canyon aspect ratio (3, 5, and 7) with and without eaves. In addition, air ventilation rate and drag coefficient were measured to investigate how the variation of turbulent flow fields near the roughness affects temporally-spatially averaged indications of urban air conditions.

The PIV experiments revealed how temporally averaged flow structures, spatial distributions of turbulent statistics, and turbulent coherent structures around roughness were changed. Under the condition that the canyon aspect ratio is 3 and 5, the region affected by the eaves are almost the entire canyons, drastically changing canyon flow structures and declining the turbulent intensity. By contrast, in the wide canyon with eaves,

the influence of the eaves is relatively small except for the upstream region, keeping the turbulent intensity and the size of coherent structures in the same degree as that of the wide canyon without eaves.

The ventilation rates were calculated based on the vertical velocity component at the canyon roof height ($z/H = 1$). The reduction rates of the ventilation strongly depend on the canyon aspect ratio, and it is associated with the physical characteristics of the turbulent flow fields, especially with coherent structures. The interaction of the turbulent flow between the region inside and above the canyon is extremely poor in the narrow canyon with eave, reducing the ventilation rate to 11% of the narrow canyon without eave. The decreasing rate is still over 50% in the middle canyon, while it is only 30% in the wide canyon. The turbulent coherent structure is affected by the eaves in only upstream region in the wide canyon with eaves, and eaves have almost no difference around the center and downstream regions, thus, the canyon ventilation rate is maintained.

Finally, the relation between the drag coefficient and flow field structures within the canyons was investigated. Drag coefficient decreases with the increase of the canyon aspect ratio in accordance with the transition of the canyon flow regimes, as indicated by past studies (e.g. Oke 1988). Regarding the canyons with eaves, drag coefficient decreases more sharply even when canyon aspect ratio is large. This is probably because the transition of the canyon flow structures is caused at the higher canyon aspect ratio by the effect of the eaves.

Reference

- Annalisa, B. D., Paolo, M., Giovanni, L., Giorgio, Q. (2014) Water-channel study of flow and turbulence past a two-dimensional array of obstacles, *boundary-layer meteorology*, vol. 155, pp. 73-85
- Adrian, R. J. (2005) Twenty years of particle image velocimetry, *experiments in fluids*, vol. 39, pp. 159-169
- Ayrault, M., Simoens, S., (1995) Turbulent concentration determination in a gas flow using multiple CCD cameras. *Journal of flow visualization and image processing*, vol.2, pp.195–208
- Coceal, O., Thomas, T. G., Castro, I. P., Belcher, S. E. (2006) Mean Flow and Turbulence Statistics Over Groups of Urban-like Cubical Obstacles, *boundary-layer meteorology*, vo. 121, pp.491-519
- Coceal, O., Dobre, A., Thomas, T. G., Belcher, S. E. (2007) Structure of turbulent flow over regular arrays of cubical roughness, *journal of fluid mechanics*, vol.589, pp. 375-409
- Hagishima, A., Tanimoto, J., Nagayama, K., Meno, S. (2013) Aerodynamic parameters of regular arrays of rectangular blocks with various geometries, *boundary-layer meteorology*, vol. 132, pp. 315-337
- Hino, M. (1992) *Fluid dynamics* (in Japanese), Asakura-shoten press, Tokyo, Japan
- Huang, Y., Xiaonan, H. and Ningbin, Z. (2009) Impact of wedge-shaped roofs on airflow and pollutant dispersion inside urban street canyons, *building and environment*, vol.44, pp.2335-2347
- Hunter, L.J., Watson, I.D., Johnson, G.T. (1991) Modelling air flow regimes in urban canyons, *Energy and buildings*, vol. 15, pp. 315-324
- Inagaki, A., Castillo, M. C. L., Yamashita, Y., Kanda, M., Takimoto, H. (2011) Large-eddy simulation of coherent flow structures within a cubical canopy, *boundary-layer meteorology*, vol. 142, pp. 207-222
- Kanda, M., Moriwaki, R., Kasamatsu, F. (2004) Large eddy simulation of turbulent organized structures within and above explicitly resolved cube arrays, *boundary-layer meteorology*, vol. 112, pp. 343-368

- Kanda, M. (2006) Large-eddy simulations on the effects of surface geometry of building arrays on turbulent organized structures, boundary-layer meteorology, vol. 118, pp. 151-168
- Kastner, K. P. and Plate, E. J. (1999) Wind-tunnel study of concentration fields in street canyons, atmospheric environment, vol. 33, pp.3973-3979
- Kellnerova, R., Kukacka, L., Jurcakova, L., Uruba, V., Janour, Z. (2012) PIV measurement of turbulent flow within a street canyon: detection of coherent motion, journal of wind engineering and industrial aerodynamics, vol.104-106, pp.302-313
- Leonardi, S., Orlandi, P., Smalley, R. J., Djenidi, L., Antonia, R. A. (2003) Direct numerical simulations of turbulent channel flow with transverse square bars on one wall, Journal of fluid mechanics, vol. 491, pp. 229-238
- Leonardi, S., Orlandi, P., Djenidi, L., Antonia, R.A. (2004) Structure of turbulent channel flow with square bars on one wall, international journal of heat and fluid flow, vol. 25, pp. 384-392
- Liu, C. H., Barth, M. C., Leung, D. Y. C. (2004) Large-eddy simulation of flow and pollutant transport in street canyons of different building-height-to-street-width ratios, Journal of applied meteorology, vol. 43, pp. 1410-1424
- Liu, C. H., Leung, D. Y. C., Barth, M. C. (2005) On the prediction of air and pollutant exchange rates in street canyons of different aspect ratios using large-eddy simulation, atmospheric environment, vol. 39, pp. 1567-1574
- Li, X. X., Liu, C. H. Leung, D. Y. C. (2008) Large-eddy simulation of flow and pollutant dispersion in high-aspect-ratio urban street canyons with wall model, boundary-layer meteorology, vol. 129, pp. 249-268
- Maruyama, T. (1991) On drag variation due to array patterns of cubic blocks (in Japanese), journal of wind engineering, no.49, pp.15-24
- Michioka, T., Sato, A., Takimoto, H., Kanda, M. (2011) Large-eddy simulation for the mechanism of pollutant removal from a two-dimensional street canyon, boundary-layer meteorology, vol. 138, pp. 195-213
- Michioka, T., Takimoto, H., Sato, A. (2014) Large-eddy simulation of pollutant removal from a three-dimensional street canyon, boundary-layer meteorology, vol.150, pp. 259-275

- Oke T. R. (1988) Street design and urban canopy layer climate. *Energy and building*, vol11, pp.103–113
- Reynolds, R. T., Castro, I. P. (2008) Measurements in an urban-type boundary layer, *experiments in fluids*, vol. 45 pp. 141-156
- Santiago, J. L., Martilli, A., Martín, F. (2007) CFD simulation of airflow over a regular array of cubes. Part I: Three-dimensional simulation of the flow and validation with wind-tunnel measurements, *boundary-layer meteorology*, vol. 122, pp. 609-634
- Scarano, F. (2005). Iterative image deformation methods in PIV, *Measurement Science and Technology*, 13, R1-R19
- Simoens, S., Ayrault, M., Wallace, J. M. (2007) The flow across a street canyon of variable width—Part 1: Kinematic description, atmospheric environment, vol. 41, pp. 9002-9017
- Simoëns, S., Wallace, J. M. (2008) The flow across a street canyon of variable width-Part 2.: Scalar dispersion from a street level line source, atmospheric environment, vol. 42, pp. 2489-2503
- Stanislas, M., Okamoto, K., Khler, C. J., Westerweel, J. (2005) Main results of the second international PIV challenge, *experiments in fluids*, vol.39, pp. 170-191
- Takano, Y. and Moonen, P. (2013) On the influence of roof shape on flow and dispersion in an urban street canyon, *journal of wind engineering and industrial aerodynamics*, vol.123, pp.107-120
- Uehara, K., Mochida, A., Yamao, Y., Oikawa, S. (2007) Wind tunnel experiments on improving the natural ventilation of a street canyon, *Journal of Japan society for atmospheric environment*, vol.42, pp.301-309
- The visualization society of Japan (2002) PIV handbook (in Japanese), morikita-shuppan press, Tokyo, Japan
- Westerweel, J. (2000) Theoretical analysis of the measurement precision in particle image velocimetry, *experiments in fluids*, vol.29, pp.S003-S012
- Zaki, S. A., Hagishima, A., Tanimoto, J., Ikegaya, N. (2010) Aerodynamic parameters of urban building arrays with random geometries, *boundary-layer meteorology*, vol. 138, pp. 99-120

CHAPTER VI

Conclusion

6.1 Conclusive summary

Creation and preservation of a pleasant environment in urban areas is one of the most important subjects for sustainable developments of human society. However, urban environmental problems is caused as a result of a complicated interaction of various numbers of sub-systems including both physical phenomena and nonphysical phenomena with various time and spatial scales, therefore, it is difficult to solve urban-type environmental problems without a comprehensive view with scientific knowledge in various study fields. Thereby, this study discussed urban environmental problems from the view point of wind engineering and comparative sociology.

In chapter 2, the process of the social agreement formation for the construction of the environmentally friendly society is investigated from a view point of comparative sociology. Through the intercomparison of regional histories of two environmentally pioneering societies in Japan and Germany, following three essential factors were extracted: management organization, symbol of clean environment, and legacy of the past. In both sample cases, a unified organization promoted area revitalization with strong leadership. The leadership conducted many projects, building consensus among residents through a symbol of clean environment, and this attitude induced follow-on environmental projects. Effective use of the heavy industry legacy of the past reinforced regional identity and raised the pride of the residents.

In chapter 3, the measurement accuracy of PIV experiments for unsteady turbulent flow fields around scaled urban building models was discussed. A bias error named peak locking is considered to be difficult to be avoided in PIV experiments especially if a measurement is conducted in a large size wind tunnel. According to the descriptions of past studies, peak locking is terminated by controlling typical particle diameter on images to be 2~3pixel, however, it is much difficult to satisfy this requirement in actual experimental conditions. Hence, the authors tried to mitigate peak locking problem by applying MCM in the image preprocessing step. MCM successfully improved the quality of particle image data obtained in an actual wind tunnel experiment, and peak clocking is drastically reduced. Furthermore, it was proved that MCM showed great performance regardless of the difference of flow field properties, indicating the usefulness of MCM for improving data accuracy of PIV experiment from a practical point of view.

Chapter 4 performed a wind tunnel experiment on turbulent flow fields around an urban canopy consists of slender rectangular blocks assuming high-rise buildings. The most important result of this experiment is identifying three typical instantaneous ascend flow patterns and three descent flow motions around block models.

One of the notable points of this study is that the instantaneous ascend and descent flow modes in the present study are quite similar to the typical instantaneous flow pattern called flushing around low-aspect building models (Takimoto et al. 2011, Inagaki et al. 2011) in both qualitative and quantitative aspects. Although transport phenomena of heat and pollutant materials are out of scope of this study, it might be considered that the typical upward flow motions identified in present study might have a large influence on the heat and pollutant removal from an urban canyons in the light of the result of past

studies.

Another remarkable point is the conjunction of typical instantaneous flow patterns and turbulent organized structure (TOS) above roughness models. The flow condition around eddies observed above roughness model were highly correspond with the feature of hairpin packet structure defined by past studies (e.g. Zhou et al. 1999, Adrian et al. 2000, Coceal et al. 2007). Although it is not definitive that the eddies shown in the present study are parts of hairpin packet structure because only one eddy was observed in each vector views due to the small measurement area, it is interesting if the large scale hairpin packet structure arises in the present roughness conditions and causes a certain type of instantaneous flow filed within the canopy.

Chapter 5 conducted a wind tunnel experiment on turbulent flow fields around 2D street canyons with and without flat eaves with three different canyon aspect ratio. The effect of eaves reaches almost the entire regions of the canyon, and temporally averaged flow structures and spatial distribution of turbulent statistics were drastically changed by the effect of eaves. On the other hand, the influence of the eaves is relatively small except for the upstream region in the large aspect ratio canyon, and common features were observed between the canyons with eaves and without eaves, such as recirculation eddy behind the windward building.

Similar tendency is observed in the coherent structure around the roughness. Judging from the 2 point correlation function of the vertical velocity component, in the small-width canyon with eaves, the penetration of large-scale turbulent structures into the canyon is prevented by the eaves. However, the influence of eaves on turbulent coherent structure is reduced with canyon aspect ratio, and very large coherent structure reaches

near the ground in the wide canyon case.

This result is strongly relevant to the canyon ventilation rates. The interaction of the flow between the region inside and above the canyon is extremely poor in the narrow canyon with eave, decreasing the ventilation ratio by 89%. The decreasing rate is still over 50% in the middle width canyon, while it is only 30% in the wide canyon. As it was mentioned above, large size turbulent coherent structures penetrate into the canyons in the case that canyon aspect ratio is large, stimulating the air mixing between the region inside and above the canyon.

Finally, the relation between the drag coefficient and flow field structures within the canyons was investigated. Drag coefficient of canyons with eaves is smaller than that of canyons without eaves regardless of canyon aspect ratio, furthermore, drag coefficient decreases sharply with the increase of aspect ratio. This is probably because the transition of the canyon flow regime is caused at the higher canyon aspect ratio by the effect of the eaves.

Reference

- Adrian, R. J., Meinhart, C. D., Tomkins, C. D. (2000) Vortex organization in the outer region of the turbulent boundary layer, *Journal of Fluid Mechanics*, vol. 422, pp.1-54
- Coceal, O., Dobre, A., Thomas, T. G. (2007) Unsteady dynamics and organized structures from DNS over an idealized building canopy, *international journal of climatology*, vol.27, pp. 1943-1953
- Inagaki, A., Castillo, M. C. L., Yamashita, Y., Kanda, M., Takimoto, H. (2011) Large-eddy simulation of coherent flow structures within a cubical canopy, *boundary-layer meteorology*, vol.142, pp.207-222
- Takimoto, H., Sato, A., Barlow, J. F., Moriwaki, R., Inagaki, A., Onomura, S., Kanda, M. (2011) Particle image velocimetry measurements of turbulent flow within outdoor and indoor urban scale models and flushing motions in urban canopy layers, *boundary-layer meteorology*, vol.140, pp.295-314
- Zhou, J., Adrian, R. J., Balachandar, S., Kendall, T. M. (1999) Mechanisms for generating coherent packets of hairpin vortices in channel flow, *Journal of Fluid Mechanics*, vol.387, pp.353-396

Appendix 2

Bottom notes for Chapter 2

- i. Minamata disease, Yokkaichi asthma, Ouch Ouch disease, and Niigata Minamata disease are considered the four major pollution-related illnesses in Japan.
- ii. Mu and Zhang (2013) investigated the influence of air pollution on human health in Beijing during January 2013. They estimated the economic loss at 23 billion Chinese yuan.
- iii. The investigating committee at that time presented seven requirements: military safety, a transport system, a supply of raw materials, a supply of industrial water, abundant labor power, and sufficient factory tools and sales contacts.
- iv. Jensen and Lonergan (2013) explains: “The system’s major aim, after strengthening coal production, is to restore steel manufacturing to drive Japanese industry as a whole. Steel is, in turn, given to coal mines, to help accelerate the extraction of more coal, and to other industrial and export businesses.”
- v. Wakamatsu, Yahata, Tobata, Kokura, and Moji.
- vi. Translated from Japanese to English by the author.
- vii. For example, the acceptable value for chemical oxygen demand (COD) was 120 ppm in national law, but the maximum limit in Kitakyushu was 15 ppm.
- viii. The IBA is a traditional architectural competition for urban planning and development. So far, IBA programs have been conducted in Darmstadt, Stuttgart, and Berlin.

- ix. The idea of “working in the park” meant the construction of attractive, green, modern working places, in combination with cultural heritage and old coal and steel production facilities if possible.'
- x. A survey conducted at that time measured dissolved oxygen in Doukaiwan Bay at 0%.

Appendix 3

3-1 calculation load of MCM

To estimate the calculation load of MCM, the numbers of calculation iteration required in preprocessing by MCM and that in velocity calculation (figure 3-2, step(e)) are compared. Both processes calculate correlation coefficient between two images, thus the calculation load are approximately compared by counting how many times the calculation is iterated. The numbers of iterative calculation to analyze one pair of image are calculated by equation A3-1 (MCM) and A3-2 (velocity calculation), respectively.

$$S_{\text{mask}} \times N_{\text{pix}} \times 2 \quad \text{A3-1}$$

$$S_{\text{interr}} \times S_{\text{search}} \times N_{\text{vector}} \quad \text{A3-2}$$

Here, S_{mask} is size of template image, N_{pix} is the total number of pixels of a particle image obtained by experiment, S_{interr} is the number of pixels of interrogation window, S_{search} is the number of pixel of search region, and N_{vector} is the number of vectors. Although the ratio of the numbers of calculation varies depending on size of particle image and parameter setting, it is considered that the number of calculation iteration of MCM does not exceed 10 % of that of velocity calculation (in authors case, it is about 1%).

A3-2 calculation procedure of statistics of particle luminance

At first, the spatially averaged luminance within 30×30 pixel is calculated about one image,

$$Ave_{lumi} = \frac{1}{900} \sum_{i=1}^{30} \sum_{j=1}^{30} Lumi(i,j) \quad A3-2-1$$

Here, $Lumi(i,j)$ is luminance at each pixel. Then, ensemble average of Ave_{lumi} is calculated about 500 images.

$$\widehat{Ave}_{lumi} = \frac{1}{500} \sum_{i=1}^{500} Ave_{lumi} \quad A3-2-2$$

Similarly, standard deviation of luminance is calculated about an image, then ensemble averaged is applied.

$$SD_{lumi}^2 = \frac{1}{900} \sum_{i=1}^{30} \sum_{j=1}^{30} (Lumi(i,j) - Ave_{lumi})^2 \quad A3-2-3$$

$$\widehat{SD}_{lumi} = \frac{1}{500} \sum_{i=1}^{500} SD_{lumi} \quad A3-2-3$$

Appendix 4

4-1 determination of convective velocity (U_c)

Tomkins and Adrian (2003), Coceal et al. (2007) specify hairpin packet structures on a smooth and cubic roughness surface with the condition that the instantaneous wind velocity is below 75% of local mean velocity, and present the highly clear horizontal vector maps of hairpin packet structures by averaging all extracted flow event. In the present study, the characteristic flow structure described by Adrian et al. (2000) (figure 4-9(b)) is observed if the convection velocity is changed with in the range of Tomkins and Adrian (2003), Coceal et al. (2007) as the figures below presents.

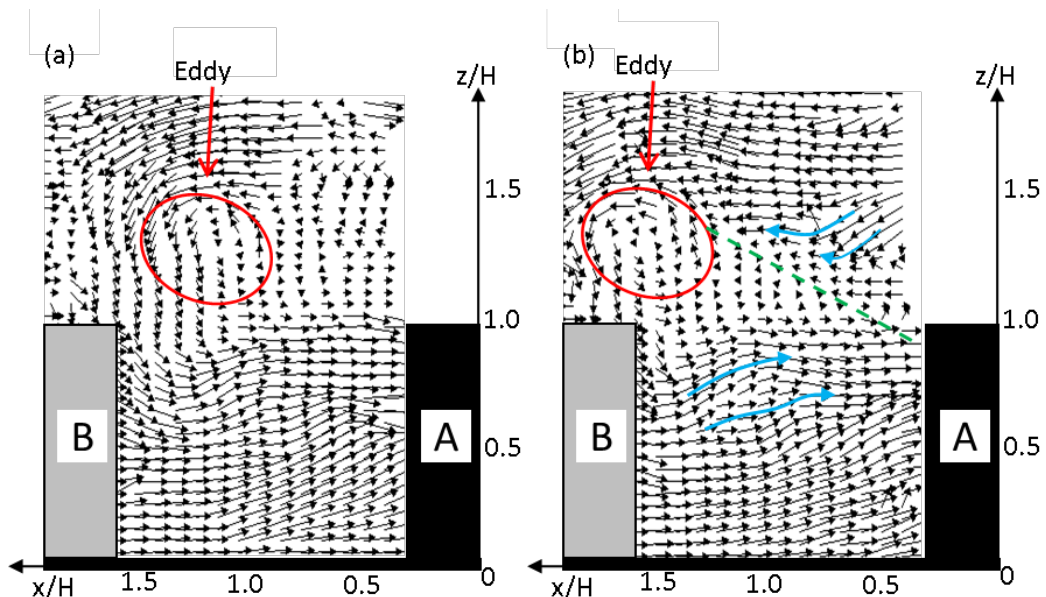


Figure AP4-1(a) and (b) vector views produced by subtracting convective wind speed ($U_c/U_{1.25H}=0.66$) from instantaneous flow fields in which ejection event arise.

Acknowledgments

I would like to express my gratitude to my supervisor Professor Aya Hagishima for her detailed comments, suggestions, and constant supports. I am also grateful to thank Professor Jun Tanimoto for his sensible and brilliant comments, valuable guidance and encouragement extended to me. I would also would like to thank Professor Naoki Ikegaya for his guidance, and his mentorship and my graduate studies and research at Kyushu University. In addition, I express my appreciation to Professor Kazuhide Ito and Yuji Sugihara for having served on my committee. Their thoughtful questions and comments were valued greatly.

I am indebted to all members of Tanimoto laboratory for providing a stimulation and fun environment in which to learn and grow. I would now have finished this thesis without kind supports of all labmates.

Finally, I would like to thank you my parents and sisters for their unconditional love and supports through my entire life.

February, 2017

Tsuyoshi Sato